An Overview of Advances in Signal Processing Techniques for Classical and Quantum Wideband Synthetic Apertures

Peter Vouras, Kumar Vijay Mishra, Alexandra Artusio-Glimpse, Samuel Pinilla, Angeliki Xenaki, David W. Griffith and Karen Egiazarian

***Abstract*—Rapid developments in synthetic aperture (SA) systems, which generate a larger aperture with greater angular resolution than is inherently possible from the physical dimensions of a single sensor alone, are leading to novel research avenues in several signal processing applications. The SAs may either use a mechanical positioner to move an antenna through space or deploy a distributed network of sensors. With the advent of new hardware technologies, the SAs tend to be denser nowadays. The recent opening of higher frequency bands has led to wide SA bandwidths. In general, new techniques and setups are required to harness the potential of wide SAs in space and bandwidth. Herein, we provide a brief overview of emerging signal processing trends in such spatially and spectrally wideband SA systems. This guide is intended to aid newcomers in navigating the most critical issues in SA analysis and further supports the development of new theories in the field. In particular, we cover the theoretical framework and practical underpinnings of wideband SA radar, channel sounding, sonar, radiometry, and optical applications. Apart from the classical SA applications, we also discuss the quantum electric-field-sensing probes in SAs that are currently undergoing active research but remain at nascent stages of development.**

***Index Terms*—Ptychography, quantum information engineering, radar, channel sounding, synthetic apertures.**

I. Introduction

Over the past several decades, an array of imaging sensors have been employed to create a single synthetic image by simulating a sensor with a much wider aperture and shallow depth-of-field. This *synthetic aperture* (SA) processing technique has led to a wide variety of cutting-edge applications in radar [1], sonar [2], radio telescopes [3], channel sounding [4], optics [5], radiometry [6], acoustics [7], quantum [8], microscopy [9] and biomedical applications, including ultrasound [10], magnetic resonance imaging (MRI) [11], magnetometry [12], and computed tomography (CT) [13]. The SAs offer savings in cost, hardware, and power while also providing a better view of occluded objects, improvement in signal-to-noise ratio (SNR), and enhanced resolution. The SAs may be constructed through motion of the sensor/object or distributed deployment of sensors. Originally invented for the radar systems in the 1950s, SAs were first implemented using digital computers in the late 1970s [1]. More advanced techniques were introduced in the late 1980s before widespread adoption in other applications throughout the 1990s [14].

The angle and delay resolution of a metrology system that collects information from the environment by steering a high-gain antenna to different directions in space is determined by the physical size of the antenna and by the instantaneous bandwidth of the transmitted signal. As the size and cost of the sensors have come down, denser and wider arrays have become feasible. Similarly, with the advent of several remote sensing and communications applications for higher frequency bands such as millimeter-wave [15] and Terahertz (THz) [16], SA systems with extremely wide bandwidths are currently being investigated. For example, millimeter-wave SA radar (SAR) is revolutionizing the rapid developments in the automotive industry toward building the next-generation autonomous vehicles [17]. In quantum applications, Rydberg state sensors are garnering significant interest for wideband receivers [8]. In SA sonar (SAS), existing algorithms are being adapted for widebeam and wideband systems to discern new properties of sea-bottom scattering [2]. In optics, coded diffraction patterns are now used to acquire several snapshots of the scene by changing the spatial configuration [18].

Novel signal processing techniques are essential for implementations of wideband SA techniques. In this paper, we provide a tutorial overview of methods to improve the spatial (angular) and delay resolution by synthesizing, respectively, a virtual aperture larger than the physical antenna and a measurement bandwidth greater than the instantaneous signal bandwidth. This paper brings together wideband SA techniques across different disciplines. Table 1 lists the SA systems considered along with a brief description of generation of the spatial aperture and the type of signal bandwidth available, e.g. instantaneously wideband, narrowband, or synthesized wideband. We remark that the wideband SAs have become more pervasive in various other fields such as seismology, biomedical, and acoustics. However, it is not possible to cover all applications in this paper and, hereafter, we only focus on the major developments in some salient applications.

In Section IV, we provide a background on SAR techniques along with some of the wideband SAR applications, including millimeter-wave SAR, wideband autofocusing, and quantum systems for SAR. Section V presents new results for systems that leverage the same antenna aperture, hardware platform, and waveforms to combine radar detection processing with data communications. In Section VI, we discuss another important SA application of channel sounding. In modern 5G/6G communications, channel sounding plays an important role in establishing system performance, especially for single-carrier modulated systems. With multiple-carrier modulations, such as Orthogonal Frequency Division Multiplexing (OFDM), a guard interval is added between symbols, which mitigates the impact of multipath and intersymbol interference (ISI). The SAs have been used in channel sounding to accurately characterize the scattering of electromagnetic fields propagating through a wireless channel. This paper describes SA channel sounders that sample the frequency response of a wireless channel. A brief introduction to possible

P. V. is with the United States Department of Defense, Washington, DC, 20375 USA, e-mail: synthetic_aperture_twg@ieee.org.

K. V. M. is with the United States DEVCOM Army Research Laboratory, Adelphi, MD, 20783 USA, e-mail: kvm@ieee.org.

A. A-G. is with the National Institute of Standards and Technology (NIST), Boulder, CO, 80303 USA e-mail: alexandra.artusio-glimpse@nist.gov.

S. P. is with the University of Manchester at Harwell Science and Innovation campus, Oxfordshire, OX110GD United Kingdom, e-mail: samuel.pinilla@correo.uis.edu.co.

A. X. is with the Centre for Maritime Research and Experimentation, Science and Technology Organization, NATO, La Spezia, 19126, Italy, email: angeliki.xenaki@cmre.nato.int.

D. W. G. is with NIST, Gaithersburg, MD, 20899, USA e-mail: david.griffith@nist.gov.

K. E. is with Faculty of Information Technology and Communication Sciences, Tampere University, Tampere, 33720, Finland, e-mail: karen.egiazarian@noiselessimaging.com.

K. V. M. acknowledges support from the National Academies of Sciences, Engineering, and Medicine via Army Research Laboratory Harry Diamond Distinguished Fellowship.

TABLE I
COMPARISON OF MAJOR WIDEBAND SA SYSTEMS

System	Spatial Aperture	Bandwidth
SAR	Aperture created via aircraft motion	Wide instantaneous bandwidth
ISAR	Aperture created via object motion	Wide instantaneous bandwidth
InSAR	Aperture created via phase difference from multiple passes	Wide instantaneous bandwidth
SA sounder via frequency domain sampling	Aperture created using mechanical positioner such as a robot	Instantaneously narrowband but synthesized wide bandwidths
SAS	Aperture created along vessel's trajectory	Instantaneously wide fractional bandwidth
Optical SA	Aperture created via mechanical positioner	Narrow instantaneous bandwidth
SA Radiometry	Large SA from sparse spatial samples	Wide synthesized bandwidth
Quantum SA via Rydberg probe	Aperture created via mechanical positioner	Instantaneously narrowband but can synthesize wide bandwidths
Quantum entanglement-based SAR	Aperture created via aircraft motion	Narrow instantaneous bandwidth but excellent noise suppression
SA ultrasound	Aperture created by acquiring *near-field* data from parts of a stationary array	Narrow instantaneous bandwidth
SA MRI/CT	Aperture created via low-resolution images acquired from a moving field-of-view (FoV)	Narrow instantaneous bandwidth but synthesized wide bandwidths
SA acoustics	Aperture created with microphones on a mobile platform	Wide instantaneous bandwidth

future paths of research describes time-domain SA sounders that utilize novel quantum sensors to measure the intensity of impinging electric fields. Then, Section VIII explains the use of various lensng techniques in optics to generate wideband apertures. In Section VIII, we introduce and discuss new developments in SAS such as wideband processing, micronavigation, and multiple-input multiple-output (MIMO) systems. New innovations and capabilities enabled through the use of machine learning techniques in SA systems are briefly summarized in Section IX. Section IV described SA applications in radiometry. We conclude in Section XI.

II. Wave Propagation

– plane waves – spherical waves

III. Array Architectures

– cylindrical arrays – polygonalization – spherical arrays at acoustic freqs – wideband DBF

IV. Wideband SAR

When a radar illuminates an object, conventional processing techniques, such as beamforming and matched filtering, are utilized to obtain downrange resolution along the radar line-of-sight (RLoS). If the object is also moving relative to the radar, then the Doppler frequency gradient is used to obtain cross-range resolution that is much finer than the radar's beamwidth. The motion of the object is generated in a variety of ways but ultimately this motion is related to the simplified case of a stationary monostatic radar illuminating a rotating object.

In Fig. 1, a three-dimensional (3-D) object illuminated by the radar signals is projected onto the x-y plane with the object rotating about the z-axis with uniform angular velocity. If the object is contained within the main beam of the radar and rotating about the point A at ω radians per second with the radar at a line-of-sight (LoS) distance R_1 from A, then the distance to a point on the object with initial coordinates (R_0, θ_0, z_0) at time $t = 0$ is

$$R = \left[R_0^2 + R_1^2 + 2R_1R_0\sin(\theta_0 + \omega t) + z_0^2\right]^{\frac{1}{2}}. \tag{1}$$

If the distance to the object is much larger than the size of the object, i.e. $R_1 >> R_0, z_0$, then a good approximation is

$$R \approx R_1 + x_0\sin(\omega t) + y_0\cos(\omega t), \tag{2}$$

and the Doppler frequency of the returned signal is

$$f_d = \frac{2}{\lambda}\frac{dR}{dt} = \frac{2x_0\omega}{\lambda}\cos\omega t - \frac{2y_0\omega}{\lambda}\sin\omega t, \tag{3}$$

where λ is the radar wavelength. If the radar data are processed over a short time interval centered at $t = 0$, the range to (x_0, y_0) and the Doppler frequency shift is approximated as

$$R = R_1 + y_0, \quad f_d = \frac{2x_0\omega}{\lambda}. \tag{4}$$

It follows that the downrange component y_0 of the position of a point scatterer is estimated by analyzing the delay of the radar return and the cross-range component x_0 is obtained by analyzing the Doppler frequency shift [19–25]. This framework captures the conventional range-Doppler imaging technique used in SAR. An implicit assumption is that the LoS distance R_1 from the radar antenna to the center of the rotating object is a constant and known

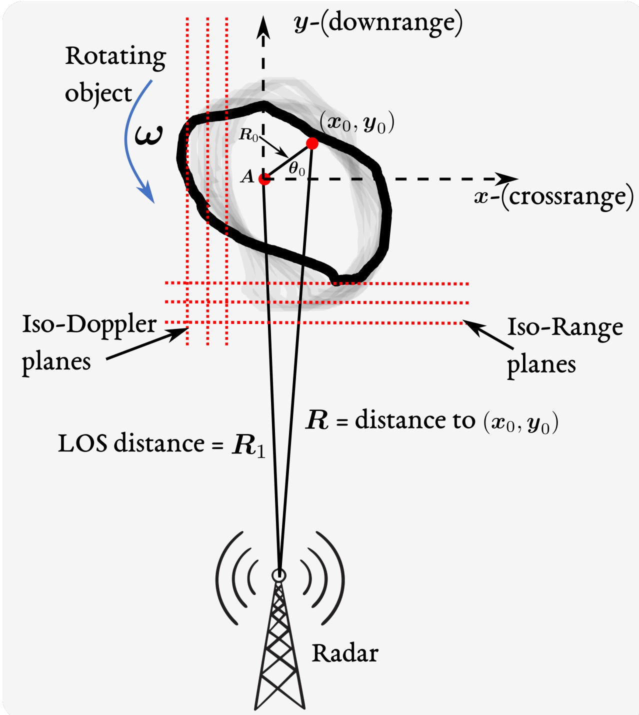

Fig. 1. Range-Doppler imaging through radar using the synthetic aperture principle. Signal bandwidth and Doppler frequency resolution determine downrange and cross-range resolutions, respectively. The graphic shows a moving target for a stationary antenna. This is the principle of inverse SAR (ISAR). In SAR, the SA is created with a moving array sensor and stationary target.

value. If R_1 is time varying, then the effects of changing range must be compensated for in the signal processing. The parallel lines in Fig. 1 perpendicular to the radar LoS are surfaces of constant delay or range. The surfaces of constant Doppler are the lines parallel to the plane formed by the RLoS and the rotation axis.

A. Resolution Performance

The downrange resolution ΔR of the monostatic radar illuminating a rotating object is determined by the instantaneous bandwidth B of the transmitted waveform, $\Delta R = c/2B$, where c is the speed of light. The factor of two arises because an incremental delay $\Delta t = 1/B$ corresponds to an incremental downrange distance $\Delta R = c\Delta t/2$. Fine range resolution is achieved with a single pulse and the corresponding processing is termed fast-time processing, meaning that the input data rate is equal to the analog-to-digital converter (ADC) sampling rate.

It follows from (4) that a cross-range resolution Δx is achieved if Doppler frequency is measured with a resolution of

$$\Delta f_d = \frac{2\omega \Delta x}{\lambda}. \tag{5}$$

A resolution of Δf_d requires a coherent processing interval of approximately $\Delta T = 1/\Delta f_d$. The cross-range resolution is

$$\Delta x = \frac{\lambda}{2\omega \Delta T} = \frac{\lambda}{2\Delta\theta}, \tag{6}$$

where $\Delta\theta = \omega\Delta T$ is the angle through which the object rotates during the coherent processing interval. Fine cross-range resolution requires multiple pulses and the corresponding processing is often called slow-time processing because the input data rate is equal to the pulse repetition frequency (PRF) of the transmitted waveform.

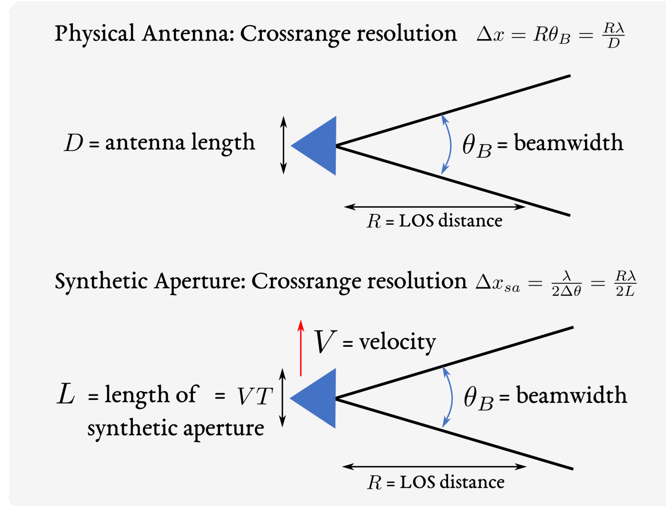

Fig. 2. Cross-range resolution of physical antenna (top) and SA (bottom).

B. Configurations

The range-Doppler imaging principle leads to several different SAR configurations [26]. Strictly speaking, SAR is a method only useful for improving cross-range resolution. One particular SAR configuration is stripmap SAR where the radar is mounted on an airborne platform and looking down from the side of the aircraft towards terrain. Assume the aircraft is moving in a straight line at a constant altitude with a speed V for a duration T along the direction perpendicular to the LoS. The length of the SA, $L = VT$, is small compared to the range R_1 to the center of the target region, so the angle subtended by the SA is approximately $\Delta\theta \approx L/R_1 = VT/R_1$.

From the viewpoint of the radar, the scene appears to be rotating with angular velocity $\omega = V/R_1$. During the duration T, the total angle through which the scene appears to rotate is $\Delta\theta = \omega T = VT/R_1$. A point scatterer in the scene will appear to have a LoS velocity of ωx relative to the radar, where x is the cross-range distance of the scatterer from the radar LoS. This apparent LoS velocity v will create a Doppler frequency of $f_d = 2v/\lambda = 2\omega x/\lambda$.

If the Doppler frequency can be measured with a resolution of Δf_d, then the corresponding cross-range resolution is

$$\Delta x = \frac{\lambda}{2\omega T} = \frac{\lambda}{2\Delta\theta} \approx \frac{\lambda R_1}{2L} = \frac{\lambda R_1}{2VT}. \tag{7}$$

Equations 6 and 7 yield the same result but are derived using different approaches. Equation 6 suggests that cross-range resolution results from the Doppler shifts created by the different apparent LoS velocities of point scatterers in the scene [27]. Equation 7 indicates that cross-range resolution is a result of the larger aperture size as measured by its length L. Both interpretations are valid and show that synthesizing larger apertures and using coherent processing can increase cross-range and angular resolution.

Fig. 2 compares the cross range resolution, defined as the distance from the mainlobe peak to the first null in the antenna pattern, for a physical antenna and for a SA of the same size. The beamwidth of the physical antenna is approximately given by $\theta_B \approx \lambda/D$, where D is the cross-range length of the antenna, which in this scenario is $D = L$. The figure illustrates that for the case of range-Doppler imaging the cross-range resolution that can be achieved by a SA is one-half the cross-range resolution possible using a physical antenna of the same size.

SAR resolution performance will be degraded if point scatterers in the scene move through different range or Doppler resolution

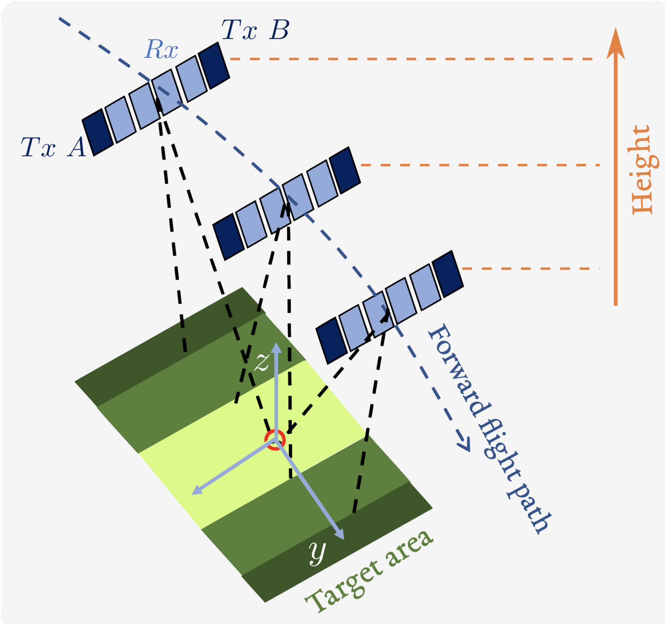

Fig. 3. Imaging geometry of the FLoSAR. The receive antenna array is flanked on both sides by a transmit antenna. As the radar traverses a curvilinear downward motion, it exploits the virtual array along the height dimension [33].

cells. Errors caused by range or Doppler bin migration will have to be removed in the signal processing or by shortening the coherent processing interval. Other errors that affect performance include a variable angular rotation rate or a radar LoS that is not orthogonal to the axis of rotation.

In the following, we describe the popular and recent wideband SAR configurations.

1) Wideband Tomographic SAR: The tomographic SAR follows the principle of CT in medical imaging through the use of diversity in the scan geometry. The transmitters and receivers are deployed in multiple locations to provide additional angular information about the targets leading to spatial diversity. This is useful for both SAR-based ground-penetrating radar (GPR) as well as space-based SAR or inverse SA radar (ISAR) [28]. For wideband tomographic SAR [29], the transmitter emits a step-frequency waveform leading to a different wavelength and resolution at each step. This method trades-off the image resolution at each stepped-frequency for the computational cost. Coherent processing of all low-resolution images obtained at each stepped frequency is then used to construct a high-resolution tomographic image of the scene.

2) Ultrawideband SAR: Low-frequency ultra-wideband (UWB) SAR has become very popular recently largely because it offers a unique capability of detecting complex hidden objects such as landmines and other explosive hazards. However, the sizes of the targets-of-interest are relatively small compared to the wavelengths of the radar signals within the operating frequency band. As a result, in the reconstructed SAR image, these targets (even when detected) only show up in a few pixels as point-like targets without any specific structure. Moreover, other manmade and clutter objects of a similar size as the targets-of-interest also result in point-like responses in SAR images. Thus, discriminating these targets from confusers or clutter objects in SAR imagery is a highly challenging task in the emerging low-frequency UWB SAR technology used for this application [30]. In general, techniques ranging from dictionary learning to neural networks (NNs) are employed for object classification in this wideband SAR mode [31, 32].

3) Millimeter-Wave SAR: Toward higher frequencies, there is growing interest in millimeter wave (mm-Wave) forward-looking SA radar (FLoSAR) technology because the very wide, unlicensed bandwidth available at mm-Wave band has potential for very high-resolution applications. In addition, the mm-Wave components have reduced dimensions and the signal experiences little attenuation at close-ranges. Yet substantial challenges remain in deploying such a system on airborne platforms whose motion is not stable within subwavelength levels because the coherent SAR processing requires subwavelength knowledge of platform position from pulse to pulse relative to the target scene. In general, coherent SAR processing relies on motion sensors such as an inertial measurement unit (IMU) or the global positioning system (GPS) for this information [34]. However, at mm-Wave, GPS accuracy is insufficient thereby leading to inaccurate or *defocused* image reconstructions. Therefore, it becomes imperative to resort to signal or data-driven motion compensation algorithms to *autofocus* SAR images [35, 36].

4) THz SAR: The free space path loss and atmospheric attenuation are severe at THz spectrum. Hence, THz band is currently explored for short-range applications such as automotive, non-destructive testing, food processing, body scanners, and indoor room profiling. The THz band offers contiguous wide bandwidths up to 15 GHz. In automotive SAR, the forward looking mode is not very useful because of relatively slight change in aperture motion. The side-mounted SAR is rendered ineffective for guiding the driver in the incoming traffic. Therefore, squint-mode with side-mounted SAR has been the preferred mode for THz automotive SAR [17]. Apart from the high-resolution, THz EM waves exhibit good penetration depth and are, therefore, employed for applications such as through-material scans. The near-optical performance of the resultant images makes these devices very useful. The spatial resolution is further enhanced through the use of MIMO-SAR at these frequencies [37].

C. Wideband Autofocusing

There is a large body of literature on SAR autofocus algorithms (see e.g. [38] and references therein). The principle of autofocusing algorithms is as follows. The range measurement introduces two artifacts: defocusing in the azimuthal domain arising from azimuth phase errors and 2-D defocusing due to range cell migration. At mm-Wave wavelength λ, wherein $4\pi/\lambda \gg 1$, the azimuth defocusing is a more serious effect and, as long as the range measurement error is less than the range resolution itself, range cell migration is negligible. Most autofocusing techniques estimate an equivalent phase error in the measured signal by modeling the effect of the position error as a linear time-invariant filter [39].

There are several approaches toward data-driven SAR image autofocus processing. The most common phase gradient autofocus (PGA) [40, 41] does not assume any specific model of the phase error function and estimates phase errors from echoes reflected from multiple strong scatterers. The method has several variations such as the eigenvector method [39] and its fast computation counterparts [42]. Alternatively, a few approaches consider minimizing the image entropy to obtain a sharp image. These algorithms exploit the fact that a focused image will yield lower entropy than its blurry counterparts [38]. More recently, autofocusing techniques based on compressed sensing [43], blind deconvolution [44], and deep learning [45] have been proposed. In the context of autofocusing in FLoSAR, very few works exist [46, 47]; further, there have not been in-depth investigations into autofocus algorithms for mm-Wave FLoSAR.

D. Multi/Hyper-Spectral Processing

Modern SARs produce valuable information content especially if they operate in multichannel [49], multi-polarization [50, 51], or

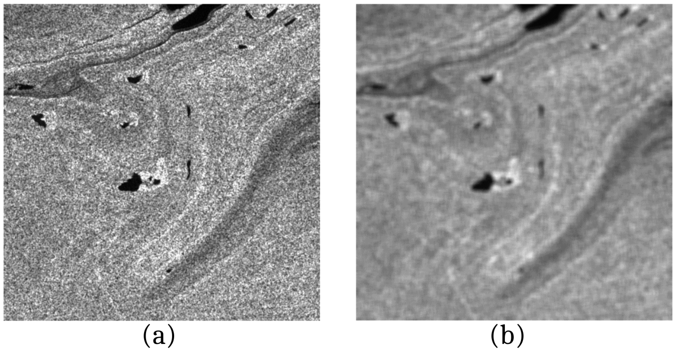

Fig. 4. Example of (a) noisy and (b) denoised SAR images using Lee filters for a window of size 5×5. In this particular example, component images from channels 5 and 11 are used of the Sentinel-2 multispectral imager [48].

multi-temporal mode [52]. The multispectral SAR typically provides images with higher spatial resolution but poorer spectral resolution. On the other hand, hyperspectral SAR acquires images in the form of a set of reflectance spectra in many contiguous and very narrow bands thereby yielding a high spectral resolution but trading off the spatial resolution. Sometimes, the SAR may be fitted with both sensors and employ techniques for hyperspectral and multispectral image fusion [49]. These applications often suffer from the presence of a multiplicative, non-Gaussian and spatially correlated [53] *speckle* noise [50] in SAR images. Mathematically, a noisy image $\boldsymbol{Z} \in \mathbb{R}^{m \times n}$ is modeled as

$$\boldsymbol{Z} = \boldsymbol{Y} \odot \boldsymbol{\zeta}, \tag{8}$$

where $\boldsymbol{Y} \in \mathbb{R}^{m \times n}$ is the target clean image, $\boldsymbol{\zeta} \in \mathbb{R}^{m \times n}$ stands for multiplicative noise with assumed variance equal to σ_μ^2, and $\odot$ represents point-wise multiplication. The image/noise model relies on general information about SAR image/speckle properties [48].

In practice, it is desired to remove this specific noise $\boldsymbol{\zeta}$ in (8) (see Fig. 4(a)) through *denoising* or *despeckling* filters [52]. However, it is not always possible, at least not without degrading useful information [52, 54]. In other words, a positive effect of speckle suppression takes place simultaneously with a negative effect of smearing of image edges and details. Depending on the properties of an image, the filter used and characteristics of speckle, there can be different proportion of positive and negative effects. When this proportion is about equal, despeckling becomes an unreasonable procedure [54].

Thus, it is important to predict the filtering performance before applying image filtering. A recent successful example is the Lee filter, which its output is expressed as

$$\boldsymbol{Z}^{\text{Lee}}[i,j] = \hat{\boldsymbol{Z}}[i,j] + \frac{\sigma_{i,j}^2}{\hat{\boldsymbol{Z}}^2[i,j]\sigma_\mu^2 + \sigma_{i,j}^2}\left(\boldsymbol{Z}[i,j] - \hat{\boldsymbol{Z}}[i,j]\right), \tag{9}$$

where $\boldsymbol{Z}^{\text{Lee}}[i,j]$ is the filtered image, $\hat{\boldsymbol{Z}}[i,j]$ denotes the local mean in the scanning window centered on the i,j-th pixel, $\boldsymbol{Z}[i,j]$ denotes the central element in the window, and $\sigma_{i,j}^2$ is the variance of the pixel values in the current window. In Fig. 4(b) we present an example of Lee filter outputs.

In [55], it was demonstrated that such a prediction is possible for filters based on the discrete cosine transform (DCT) with application to SAR images acquired by the Sentinel-1 sensor. Here, data provided by the Sentinel-1 sensor have been already used for several important applications [56]. Then, there are numerous papers dealing with estimation of image quality [57] including visual quality and prediction of filtering efficiency [55]. For the corresponding methods, there is a clear tendency to apply neural networks (NNs) [55]. Then, it is increasingly popular to employ visual quality metrics in analysis of image original quality and filter performance [55]. Finally, it has been shown that filtering efficiency can be predicted for different types of noise (additive, pure multiplicative, and, in general, signal dependent; white and spatially correlated) and for different types of filters [58].

Filtering based on the DCT [55] is one type of filtering used to remove speckle. Meanwhile, there are many other methods to deal with SAR image denoising and the prediction of filter efficiency. Thus, we have tried to design and apply a predictor based on a trained NN for the well-known Lee filter [59] that is included in many existing tools for SAR image despeckling.

E. Quantum Systems for SAR

While, at present, a fully quantum SAR system is yet to be demonstrated, steps toward practical quantum SAR have been made in recent years that bear mentioning. A quantum SAR (QSAR) system is any SAR system that exploits the effects of quantum mechanics. Generally speaking, QSAR systems employing entanglement are the primary schemes being considered by the community. The benefit of entanglement QSAR is the enhanced ability to distinguish signals from noise especially in low SNR scenarios. This allows for the use of very weak transmitter powers with such systems showing excellent potential for covert applications (see, e.g., [60]) or cases where radiation dose must be limited, e.g., imaging of human tissue and other biomedical applications.

Entanglement QSAR is based on the principle that two entangled signals have a higher degree of correlation than their classical counterparts. This enhanced correlation means that any matching that takes place following the injection of noise through a measurement activity is more robust and likely to return a correct positive match. Even though the process of launching one of the two entangled signals into free space destroys the entanglement, from the combination of noise and loss mechanisms, successful detection is still enhanced by the degree of entanglement [61]. For example, consider the engtangled state $\Psi_{SI} = (1/\sqrt{d})\Sigma_k \left|k\right\rangle_S \left|k\right\rangle_I$ for a signal photon, sent in the direction where an object is expected to be, and idler photon, where d is the number of signal and detector modes. Assuming noise is injected into the system, where b is the number of noise photons, an object with reflectivity η is likely to be detected when $\eta/b > 1$ whether entanglement is used in the measurement or not. However, when $\eta/b < 1$, the SNR is low and a simple analysis [61] shows that on average $8b/n^2$ photons must be collected to distinguish the signal from noise in a classical measurement, whereas only $8b/n^2d$ photons on average are needed when entanglement is used. In other words, the degree of entanglement defined by the number of modes d enhances the SNR and reduces the number of trials needed to distinguish a signal photon from noise.

Following a theoretical study using SNR and error detection probability calculations, Lanzagorta et al. predicted the benefit of entanglement-based QSAR over coherently integrated classical SAR [62]. They define SNR as

$$SNR = \frac{PG^2\lambda^3\sigma_0\delta_r}{2(4\pi)^3R^3k_bT_0F_nl_av\cos(\theta)}, \tag{10}$$

where P is the average transmitted power in the classical regime or $P = M\hbar\omega$ in the quantum regime defining M signal photons of frequency ω and $\hbar = h/2\pi$, h is Planck's constant. In this expression, G is the antenna gain, λ is the radar wavelength, σ_0 is the target radar cross-section, δ_r is the range resolution, R is the range to the target, k_b is Boltzmann constant, T_0 is the normal scene noise temperature,

F_n is the dimensionless noise figure, l_a is the loss due to atmospheric attenuation, v is the speed of the radar platform, and θ is the grazing angle. They also define the detection error probability of the classical and quantum systems, respectively, in the low brightness, high noise, low reflectivity regime as

$$\epsilon_c = \frac{1}{2}e^{-SNR/4}, \qquad \epsilon_q = \frac{1}{2}e^{-SNR}. \tag{11}$$

Comparing the classical and quantum detection error probabilities, advantages of QSAR are found in range, speed, target size, and grazing angle. For example, by defining a clear image as one having an SNR of at least 5 dB, QSAR returns clear images over a range of 125 km while classical SAR does not in their analysis. This and other theoretical studies of microwave entanglement applied to radar, ranging, and SAR motivate the investigation of practical realizations of these quantum systems.

In quantum illumination (QI) [61], a signal and idler pair of entangled photons are generated by some parametric converter. The signal is sent into free space while the idler is held in memory at the point of the receiver. At the time when the signal is expected to return, the received signal is compared with the saved idler to determine if what was received is noise or the returned signal. Holding the idler in quantum memory is non-trivial and generally limits the detection range due to losses in that memory. Therefore, two groups have demonstrated schemes where a quadrature measurement is made on the idler to digitize its information for more convenient storage.

Luong et al. presented experimental measurements in 2019 demonstrating their so-called quantum two-mode squeezing (QTMS) technique where the in-phase (I) and quadrature (Q) voltage signals of the retained idler and returned signal are mixed to enhance sensitivity [63]. They used a Josephson parametric amplifier to generate an entangled pair at 6.1445 GHz (idler) and 7.5376 GHz (signal). Both signals were first passed through a chain of amplifiers before being split into two paths, detected, and compared. The experimental demonstration did not include a target as the transmitter and receiver horns of the radar system were pointing directly at each other; nevertheless, they demonstrated the process of a detection by performing matched filtering between the stored 6 GHz and launched 7 GHz signals. The technique showed some quantum benefit when the team exchanged the quantum signal generator (the Josephson parametric amplifier) with a classical signal generator. The correlated classical signals underwent the exact same amplification and propagation chains followed by the same matched filtering. Based on receiver operating characteristic curves, Luong et al. found that, at low SNR, the classical measurement required longer integration time to reach the signal performance of the QTMS measurement [63]. The authors note there are similarities between their QTMS radar technique and noise radar in [64] and discuss spaces for future development of this and related quantum radar systems in [65].

In 2020, Barzanjeh et al. published a thorough investigation of a QI setup with a digital receiver [66]. Their use of the digital detection scheme, where again I and Q voltages are obtained of the signal and idler, circumvents the memory requirements of the traditional QI schemes [67]. In this setup, a Josephson parametric converter (JPC) was used to generate the entangled signals through three-wave mixing producing the signal photons at $\omega_S/2\pi = 10.09$ GHz and idler photons at $\omega_I/2\pi = 6.8$ GHz. Following amplification, the signal and idler are down converted to an intermediate frequency of 20 MHz and digitized with a sample rate of 100 MHz. They applied a fast Fourier Transform (FFT) and postprocessing to obtain I and Q voltages for the signal and idler paths, respectively. These quadrature voltages are related to the complex amplitudes a_j and their complex conjugate a_j^* of the signal ($j = S$) and idler ($j = I$) modes at the output of the JPC by

$$a_j = \frac{I_j + iQ_j}{\sqrt{2\hbar\omega_j B\Omega G_j}}, \qquad a_j^* = \frac{I_j - iQ_j}{\sqrt{2\hbar\omega_j B\Omega G_j}}, \tag{12}$$

where $\Omega = 50$ ohms is the resistance, $B = 200$ kHz is the measurement bandwidth, and $(G_S, G_I) = (93.98(01), 94.25(02))$ dB is the measured system gain for each channel. They also measured the added system noise to be $(n_S, n_I) = (9.61(04), 14.91(1))$ referenced to the JPC output. The degree of entanglement is measured using the nonseparability criterion $\Delta := \langle \hat{X}_-^2 \rangle + \langle P_+^2 \rangle < 1$, where $\hat{X}_- = (\hat{a}_S + \hat{a}_S^\dagger - \hat{a}_I - \hat{a}_I^\dagger)/2$, $\hat{P}_+ = (\hat{a}_S - \hat{a}_S^\dagger + \hat{a}_I - \hat{a}_I^\dagger)/(2i)$, $\langle \hat{O} \rangle$ defines the mean of the operator O, and $O^\dagger$ is the transpose conjugate of the operator O. They measure Δ as a function of the signal photon number $N_S = \langle \hat{a}_S^\dagger \hat{a}_S \rangle$, and find that at low photon number, Δ is below one meaning the outputs of the JPC are entangled, while at larger photon number obtained with large pump powers, entanglement gradually degrades and vanishes at $N_S = 4.5$ photons/sHz.

With this confirmation of entanglement, Barzanjeh et al. then analyzed the SNR of the QI detection (Eq. 13) with comparisons to classical illumination (also Eq. 13), subjected to the same noise and loss conditions as the QI measurement, and to a coherent-state illumination scheme (the classical benchmark) with digital homodyne (Eq. 14) and digital heterodyne (Eq. 15) detection also following the same measurement chain, signal bandwidth, and signal power. Their analysis showed marginal quantum enhancement of the SNR over the classical benchmark with perfect microwave photon counting of the idler, which they simulate by calibrating the idler path.

$$SNR_{QI/CI} = \frac{\left(\langle \hat{N}_1 \rangle - \langle \hat{N}_0 \rangle\right)^2}{2\left(\sqrt{\sigma_{N_1}^2} + \sqrt{\sigma_{N_0}^2}\right)^2} \tag{13}$$

$$SNR_{CS}^{homo} = \frac{\left(\langle \hat{X}_{S,1}^{det} \rangle - \langle \hat{X}_{S,0}^{det} \rangle\right)^2}{2\left(\sqrt{\sigma^2_{X_{S,1}^{det}}} + \sqrt{\sigma^2_{X_{S,0}^{det}}}\right)^2} \tag{14}$$

$$SNR_{CS}^{het} = \frac{\left(\langle \hat{X}_{S,1}^{det} \rangle - \langle \hat{X}_{S,0}^{det} \rangle\right)^2 + \left(\langle \hat{P}_{S,1}^{det} \rangle - \langle \hat{P}_{S,0}^{det} \rangle\right)^2}{2\left(\sqrt{\sigma^2_{X_{S,1}^{det}} + \sigma^2_{P_{S,1}^{det}}} + \sqrt{\sigma^2_{X_{S,0}^{det}} + \sigma^2_{P_{S,0}^{det}}}\right)^2}, \tag{15}$$

where $\hat{N}_j = \hat{a}_{j,+}^\dagger \hat{a}_{j,+} - \hat{a}_{j,-}^\dagger \hat{a}_{j,-}$ is the annihilation operator of the mixed signal and idler modes in the absence ($j = 0$) or presence ($j = 1$) of a target, where $\hat{a}_{j,\pm} = (\hat{a}_{S,j}^{det\dagger} + \sqrt{2}\hat{a}_v \pm \hat{a}_I^{det})/\sqrt{2}$, $\hat{a}_v$ is the vacuum noise operator, $\hat{a}_{S,j}^{det}$ is the detected radiation, and σ_O^2 is the variance of the operator O. Also, $\hat{X}_{S,j}^{det} = (\hat{a}_{S,j}^{det} + \hat{a}_{S,j}^{det\dagger})/\sqrt{2}$ and $\hat{P}_{S,j}^{det} = (\hat{a}_{S,j}^{det} - \hat{a}_{S,j}^{det\dagger})/\sqrt{i2}$ are the field quadrature operators. To calibrate the number counting of the idler, Barzanjeh et al. reduce the variance in the denominator of Eq. 13 by the calibrated idler vacuum and amplifier noise as $\langle \hat{a}_I^\dagger \hat{a}_I \rangle = \langle \hat{a}_I^{det\dagger} \hat{a}_I^{det} \rangle / (G_I - (n_I + 1))$.

There are significant challenges still to overcome before QSAR becomes a reality. The generation of entangled microwave signals and the quantum detection of those signals, both likely requiring cryogenic temperatures and, for the moment struggling with heavy amplification noise, are the main technological barriers to practical implementations of QSAR or any quantum illumination application in the microwave regime [68–71]. Plus, the synchronization of the signal and idler places some constraints on the measurement acquisition process that are noteworthy [72]. That said, new innovations are consistently put forward, meaning there is reason to continue to track developments in this field and look forward to new advancements.

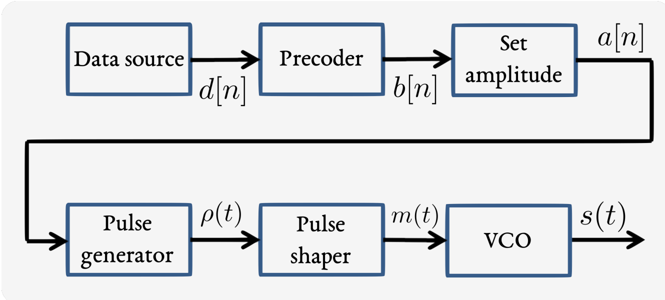

Fig. 5. Simplified illustration of BFSK transmit chain. Wideband SAR systems are suitable for combining such a communications system in the existing hardware.

V. Single Aperture Joint Communications-Radar

Historically, there has been strong interest in combining the functions of radar and data communications using a single aperture [15]. If one considers only the output of a single beamformer channel and the waveforms that are generated by modulating one carrier, then it seems possible to combine the detection functions of a radar and a communications systems into a single aperture. This capability is especially practical for software defined systems where the transmitted and received signals are digitized as close to the antenna as possible, allowing for much of the necessary functionality to be built into software. Ideally, digitization would occur behind each element of a phased array, as in digital beamforming (DBF) architectures, such that software selects the necessary processing functions for executing a desired task. This section provides a brief description of the processing similarities and differences between a notional radar as compared to a digital communication system assuming both systems rely on a binary frequency shift keying (BFSK) waveform. The situation is more complex for multi-carrier waveforms or for systems that can generate multiple beamformer output channels, including simultaneous beams. Since wideband SAR systems also operate at high power levels they are well suited for high data-rate communications. References are provided to highlight some of the recent advances in joint radar-communications processing.

For the case of BFSK modulation, a notional block diagram describing the transmit chain is shown in Fig. 5. With BFSK two tones at f_0 and f_1 are used to transmit two symbols A and B. The symbol rate, R, is known as the Baud rate and $|f_1 - f_0|$ is the frequency excursion. The modulation index h is,

$$h = \frac{|f_1 - f_0|}{R}. \tag{16}$$

If the tone spacing equals one-half the symbol rate, then $h = 0.5$ and the modulation is known as minimum shift keying (MSK). The minimum value that h can take is 0.5 because any smaller values will violate the orthogonality of the tones f_0 and f_1. Notice that since $|f_1 - f_0| = 2R$ for the case of MSK, transmitting at higher data rates will require a higher signal bandwidth.

Referring to Fig. 5, the precoder converts the input data $d[n]$ into a discrete sequence of bits $b[n]$ with values of 0 or 1. Absolute encoding is used if the bit sequence $b[n]$ corresponds directly to points in a symbol constellation. Differential encoding is used if the values of $b[n]$ correspond to the changes in the data sequence $d[n]$. For a radar, typical values for $b[n]$ might be a pseudo-noise (PN) sequence with low autocorrelation sidelobes. The PN codes allow peak-power constrained radars to illuminate targets with high average-power, long-duration waveforms that also provide high delay resolution after matched filtering. The Amplitude block in Fig. 5 converts the precoded bits $b[n]$ into amplitude levels -1 or 1 according to $a[n] = (-1)^{b[n]}$. The pulse generator creates a continuous-time waveform of pulses $p(t)$ which are then filtered by the pulse shaper to control the waveform's bandwidth. The filter's output $m(t)$ drives a voltage controlled oscillator (VCO) whose frequency varies between $f_c - f_0$ and $f_c + f_1$. The final transmitted signal $s(t)$ can be represented as,

$$\begin{aligned} s(t) &= m_{\mathrm{I}}(t)\cos(2\pi f_c t + \theta_c) - m_{\mathrm{Q}}(t)\sin(2\pi f_c t + \theta_c) \\ &= \mathrm{Re}\left[(m_{\mathrm{I}}(t) + \mathrm{j} m_{\mathrm{Q}}(t))(\cos(2\pi f_c t + \theta_c) + \mathrm{j}\sin(2\pi f_c t + \theta_c))\right] \\ &= \mathrm{Re}\left[(m_{\mathrm{I}}(t) + \mathrm{j} m_{\mathrm{Q}}(t)) e^{\mathrm{j}(2\pi f_c t + \theta_c)}\right]. \end{aligned} \tag{17}$$

The term $(m_{\mathrm{I}}(t) + jm_{\mathrm{Q}}(t)$ is known as the complex envelope of the signal with in-phase component $m_{\mathrm{I}}(t)$ and quadrature component $m_{\mathrm{Q}}(t)$. The complex envelope contains all the information of the signal. For the case of BFSK,

$$\begin{aligned} &\text{Symbol A} \to a[n] = -1 \to m_{\mathrm{I}}(t) = \cos(2\pi(f_c - f_0)t + \theta(t)), \\ &\text{Symbol B} \to a[n] = +1 \to m_{\mathrm{Q}}(t) = \cos(2\pi(f_c + f_1)t + \theta(t)), \end{aligned} \tag{18}$$

where the phase $\theta(t)$ may change randomly or deterministically with each symbol depending on the VCO.

A. Intersymbol Interference

The role of the pulse-shaping filter in the transmit chain highlights the major differences between the mission requirements of a radar and a digital communication system. An optimal waveform for a radar produces a thumb-tack ambiguity diagram (to be described later) and measures the Doppler and range of a target unambiguously. Typically, a matched filter is used on receive because it achieves the maximum output SNR for a signal in additive white noise.

In digital communications, especially in environments with congested spectrum, such as with cellular telephones or wireless local area networks (LANs), transmitting a sequence $p(t)$ of ideal brick-wall pulses that never overlap in time would require infinite bandwidth due to the $\sin(f)/f$ spectrum for each pulse. Since there is an inverse relationship between bandwidth and the temporal extent of a signal, limiting the signal bandwidth will increase the duration of each symbol and cause it to interfere with neighboring symbols, creating ISI. Choosing an appropriate pulse-shaping filter limits the ISI created when a finite bandwidth pulse spreads into the time bin of an adjacent pulse.

In general, the maximum possible symbol rate without ISI for a baseband receiver with frequency bandwidth of f_{SY} Hz is $f_{\mathrm{SY}} = 1/T$ symbols per second, where T is the Baud interval or duration of a single symbol. Note that $1/T$ is the symbol or Baud rate, not the bit rate, since there may be multiple bits per symbol. This result is known as the Nyquist bandwidth constraint and should not be confused with the Nyquist sampling criterion which states that a signal can be reconstructed from its samples provided that the sampling frequency $f_{\mathrm{SAM}} \geq 2 f_{\mathrm{MAX}}$, where f_{MAX} is the highest frequency component of the signal.

Three spectral-shaping filters are typically used to control the spectral splatter of symbols and to limit ISI. The zero-ISI $\sin(t)/t$ or $\mathrm{sinc}(t)$ filter for a symbol rate f_{SY} is

$$h_{\mathrm{SINC}}(t) = \frac{\sin(\pi f_{SY} t)}{(\pi f_{SY} t)}. \tag{19}$$

This filter produces a $\sin(t)/t$-shaped pulse which is equal to unity at time $t = 0$ and is also zero at the sampling instants corresponding to

$$t = \frac{n}{f_{\mathrm{sy}}}, \quad n = \ldots -2, -1, 0, 1, 2, \ldots \tag{20}$$

A more common spectral control filter is generated by multiplying the $\sin(t)/t$ function by a raised cosine. This filter provides less passband ripple and lower sidelobes in the pulse spectrum. The impulse response is given by,

$$h_{\mathrm{COS}}(t) = \frac{\sin(\pi f_{\mathrm{SY}} t)}{(\pi f_{\mathrm{SY}} t)} \cdot \frac{\cos(\beta \pi f_{\mathrm{SY}} t)}{1 - 4\beta^2 t^2 f_{\mathrm{SY}}^2}, \tag{21}$$

where β is a rolloff factor that describes how steeply the filter's passband transitions. If f_{BW} denotes the null-to-null bandwidth of the filter's frequency response, then $\beta = (f_{\mathrm{BW}} - f_{\mathrm{SY}})/f_{\mathrm{SY}}$. Values of $\beta > 0$ allow excess bandwidth that enable the receiver to recover the symbol or Baud timing from the transmitted waveform. Typical values of β are in the range 0.3 to 0.5.

The raised cosine waveform is ideal but it is not possible to matched filter such a signal and still maintain zero ISI. Therefore, the square root of the raised cosine frequency response $H_{\mathrm{COS}}^{0.5}(f)$ is applied at the transmitter and also at the receiver to yield the desired raised cosine response $H_{\mathrm{COS}}(f)$.

B. Radar Ambiguity Function and Matched Filtering

For radar the primary objective of any waveform is measuring the velocity and range of a target. To maximize SNR the receive waveform is often processed using a matched filter. The detection performance of a radar waveform is often analyzed using the concept of an ambiguity function. The ambiguity function represents the output of a matched filter for all possible target delays and Doppler shifts.

The ambiguity function $\Psi(\tau, f_d)$ for a transmit waveform with complex envelope $u(t)$ is defined as the squared magnitude of the autocorrelation function $\chi(\tau, f_d)$,

$$\Psi(\tau, f_d) = |\chi(\tau, f_d)|^2, \tag{22}$$

where τ represents relative time delay and f_d is Doppler shift. The autocorrelation function $\chi(\tau, f_d)$ for $u(t)$ is defined as,

$$\chi(\tau, f_d) = \int_{-\infty}^{\infty} u(t) u^*(t+\tau) e^{\mathrm{j}2\pi f_d t} dt. \tag{23}$$

The value of the ambiguity function at the origin is equal to $(2E)^2$ where E is the energy of the bandpass signal corresponding to $u(t)$, and the volume under the ambiguity function is also equal to $(2E)^2$.

The impulse response of a filter matched to a waveform $u(t)$ is given by

$$h_{mf}(t) = u^*(-t). \tag{24}$$

The output $y(t)$ of a matched filter to an input signal $s(t) = u(t)e^{\mathrm{j}2\pi f_d t}$ with zero time delay and Doppler shift f_d is given by the convolution of $s(t)$ with the matched filter impulse response $h_{mf}(t)$,

$$y(t) = \int_{-\infty}^{\infty} u(t') u^*(t'-t) e^{\mathrm{j}2\pi f_d t'} dt'. \tag{25}$$

Comparing this result with the definition of the autocorrelation function shows that the matched filter response can be expressed as,

$$y(t) = \chi(-t, f_d). \tag{26}$$

Thus, the matched filter output for a target with Doppler frequency f_d is a time-reversed version of the autocorrelation function.

The ambiguity function computed from the magnitude squared autocorrelation of the baseband radar waveform $u(t)$ can be used to describe the resolution performance of the waveform. For example, assume $u(t)$ is normalized to have unit energy,

$$\int_{-\infty}^{\infty} |u(t)|^2 dt = 1, \tag{27}$$

and two targets are located in the same angular direction and with equal radar cross sections. If one target is located at the origin of the delay-doppler plane with zero Doppler and zero relative time delay, then the value of the ambiguity function is unity, $\Psi(0,0) = 1$. If a second target is located at a slightly different Doppler frequency f_d and delay offset τ, then it is not resolvable at locations in the delay-Doppler plane that place the peak value of $\Psi(\tau, f_d)$ within the mainlobe of the reference target at $\Psi(0,0)$.

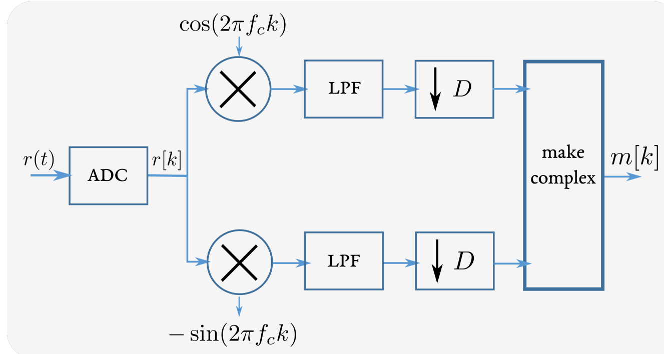

Fig. 6. The I/Q demodulator for wideband signals replaces the standard decimator after filtering by a polyphase filter bank.

C. Wideband Signal Basebanding

Demodulating a received communications signal is not the same process as traversing the transmit chain backwards. The demodulator must recover the carrier frequency and the baud rate from the received signal. In the absence of any multipath or interference, the received signal $r(t)$ is equal to the transmitted signal $s(t)$ given in (17). The transmitted data is contained in the complex envelope of the modulation $m(t)$ which must be recovered from $r(t)$. If the carrier frequency f_c and carrier phase ϕ_c are perfectly known, then multiplying $r(t)$ by $\cos(2\pi f_c t + \phi_c)$ and $\sin(2\pi f_c t + \phi_c)$ yields,

$$\begin{aligned} &r(t)\cos(2\pi f_c t + \phi_c) \\ &= 0.5\left[m_{\mathrm{I}}(t)\left[1 + \cos(2\pi 2 f_c t + 2\phi_c)\right] - m_{\mathrm{Q}}(t)\left[\sin(2\pi 2 f_c t + 2\phi_c)\right]\right], \end{aligned} \tag{28}$$

and

$$\begin{aligned} &-r(t)\sin(2\pi f_c t + \phi_c) \\ &= -0.5\left[m_{\mathrm{I}}(t)\sin(2\pi 2 f_c t + 2\phi_c) + m_{\mathrm{Q}}(t)\left[1 - \cos(2\pi 2 f_c t + 2\phi_c)\right]\right]. \end{aligned} \tag{29}$$

Thus, low pass filtering these products yields $0.5 m_{\mathrm{I}}(t)$ and $0.5 m_{\mathrm{Q}}(t)$. Typically, the filter output is then also decimated to a lower sample rate. This process is summarized in Fig. 6. For wideband signals sampled at a high rate, decimation is not performed after filtering since that wastes computations. Instead, a polyphase filter bank is used to split the input signal $r[k]$ into D sub-bands operating at a sample rate reduced by a factor of D. Rather than convolving all signal samples with a filter and then retaining only the Dth sample, the polyphase filter bank only calculates the convolution samples that are retained [73]. Note that if the system designer has the flexibility to choose the sampling frequency in relation to the intermediate frequency (IF) according to

$$f_s = \frac{4 f_{\mathrm{IF}}}{2M - 1}, \tag{30}$$

where M is an integer, then digital downconversion schemes can generate I and Q samples directly from the output $r[k]$ of the ADC [74, 75].

If the estimated carrier phase $\tilde{\phi}_c$ does not equal the true value ϕ_c, then multiplying $r(t)$ by $\cos(2\pi f_c t + \tilde{\phi}_c)$ and $\sin(2\pi f_c t + \tilde{\phi}_c)$ and low-pass filtering as before yields,

$$\begin{aligned}\tilde{m}_{\mathrm{I}}(t) &= 0.5\left[m_{\mathrm{I}}(t)\cos(\phi_c - \tilde{\phi}_c) - m_{\mathrm{Q}}(t)\sin(\phi_c - \tilde{\phi}_c)\right], \\ \tilde{m}_{\mathrm{Q}}(t) &= 0.5\left[m_{\mathrm{I}}(t)\sin(\phi_c - \tilde{\phi}_c) + m_{\mathrm{Q}}(t)\cos(\phi_c - \tilde{\phi}_c)\right].\end{aligned} \quad (31)$$

In the complex plane, $(\tilde{m}_{\mathrm{I}}(t), \tilde{m}_{\mathrm{Q}}(t))$ is a rotated version of $(m_{\mathrm{I}}(t), m_{\mathrm{Q}}(t))$. Thus, the effect of not correctly compensating for carrier phase is that after demodulation is complete, the symbol constellation will appear rotated.

Alternatively, if the estimated carrier frequency $\tilde{f}_c$ does not equal the true value f_c, perhaps due to oscillator drift, then multiplying $r(t)$ by $\cos(2\pi \tilde{f}_c t + \phi_c)$ and $\sin(2\pi \tilde{f}_c t + \phi_c)$ and low-pass filtering as before yields,

$$\tilde{m}_{\mathrm{I}}(t) = 0.5\left[m_{\mathrm{I}}(t)\cos(2\pi(f_c - \tilde{f}_c)t) - m_{\mathrm{Q}}(t)\sin(2\pi(f_c - \tilde{f}_c)t)\right], \quad (32)$$

$$\tilde{m}_{\mathrm{Q}}(t) = 0.5\left[m_{\mathrm{I}}(t)\sin(2\pi(f_c - \tilde{f}_c)t) + m_{\mathrm{Q}}(t)\cos(2\pi(f_c - \tilde{f}_c)t)\right].$$

Geometrically, the point $(\tilde{m}_{\mathrm{I}}(t), \tilde{m}_{\mathrm{Q}}(t))$ will rotate continuously in the complex plane at a rate equal to the frequency error, $f_c - \tilde{f}_c$. In short, the impact of not knowing the carrier frequency correctly is that the symbol constellation will appear spinning after demodulation.

The process of estimating the complex envelope $m(t) = m_{\mathrm{I}}(t) + \mathrm{j}m_{\mathrm{Q}}(t)$ can also be performed after digitizing the real-valued receive signal mixed down to the IF. When sampling a wideband signal, the analog-digital-converter (ADC) ideally operates at the lowest practical sampling rate without aliasing the signal. The top-left corner of Fig. 7 illustrates the spectrum of the real-valued received signal after mixing down to the IF. Because the signal is real, the spectrum is double-sided. If the Nyquist sampling criterion is obeyed then the analog-to-digital sampling frequency must be at least twice the highest frequency component of the signal. However, such a high sampling rate is unnecessary given that the signal only occupies a band-pass region and the information in the positive and negative frequency sidebands is redundant. To reduce the required sampling frequency, the two sidebands could be moved closer together until they touch at 0 Hz as shown in the top right. If the sidebands move any closer, they will overlap which creates aliasing as shown in the bottom left. The optimal solution is to eliminate one of the sidebands (since retaining both is redundant) and then shift the remaining sideband to 0 Hz. This signal could then be represented at the lowest sampling rate and is equivalent to the desired complex envelope of the transmitted signal. Equivalent implementations that use band-pass instead of low-pass filtering can be constructed using the Hilbert transform [73].

D. Fewer-Bit Sampling of Wideband Signals

In narrowband digital receivers the primary consideration driving the choice of ADC hardware is dynamic range. Typically, the system design chooses an ADC with the maximum available dynamic range that also satisfies constraints on sampling rate, power dissipation, and cost. In wideband applications however, it may be desirable to sample with fewer bits so as to increase the sample rate [77–83].

Fig. 8 illustrates the contributions to the dynamic range of an ADC that samples input signals at a rate of $1/T_s$, where T_s is the sample period and is chosen proportionally to signal bandwidth. The output of the ADC is quantized to one of 2^B levels, where B is the number of bits. The amplitude quantization intrinsic to an ADC creates a random error known as quantization noise. The quantization noise power for a sinusoidal input signal is approximately equal to [84]

$$N_{\mathrm{QU}} = \frac{\mathrm{LSB}^2}{12} = \frac{1}{12}\left(\frac{V_{\mathrm{FS}}}{2^B}\right)^2, \quad (33)$$

where LSB denotes the least significant bit voltage value and V_{FX} is the peak-to-peak full scale range at the ADC input. If the input signal is a full scale sinusoid, the ideal output signal power is $V_{\mathrm{FS}}^2/8$ which implies the SNR at the output of the quantizer is

$$\mathrm{SNR}_{\mathrm{OUT}} = \frac{V_{\mathrm{FS}}^2/8}{N_{\mathrm{QU}}} = 1.5(2^{2B}) = 6.02B + 1.76 \quad \mathrm{dB}. \quad (34)$$

A more common figure of merit is the signal-to-noise-and-distortion ratio (SNDR or SINAD), which includes the power contribution from nonlinear distortions at the ADC output. Substituting SNDR in (34) yields an expression for the effective number of ADC bits (ENoB),

$$\mathrm{ENoB} = \frac{\mathrm{SNDR}_{\mathrm{OUT}} - 1.76}{6.02}. \quad (35)$$

The ADC's full-scale output power and quantization noise floor determine the upper bound of receiver dynamic range. The total gain from the RF and IF components should be chosen such that the maximum input signal to the ADC is less than full-scale by about 1 to 10 dB to avoid signal distortion. The RF gain should be sufficiently large so that the receiver's thermal noise is dominated by the noise figure and noise bandwidth of the RF front end rather than the thermal noise contributions from gain or loss in the IF section or ADC input stages. The thermal noise power adds linearly to the quantization noise floor as shown in Fig. 8. It is often desirable to design the thermal noise to be approximately 10 dB higher than the

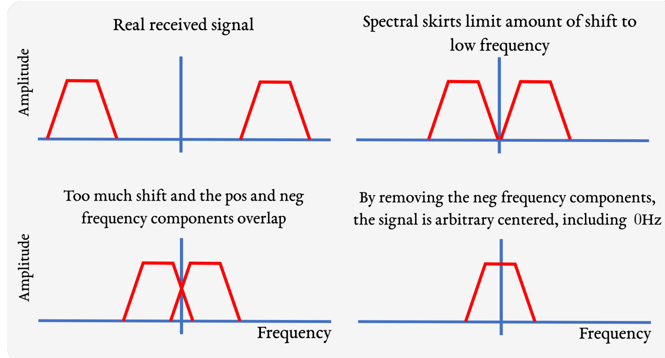

Fig. 7. Complex basebanding of wideband signals. The ADC employs subsampling techniques [76] at the receiver.

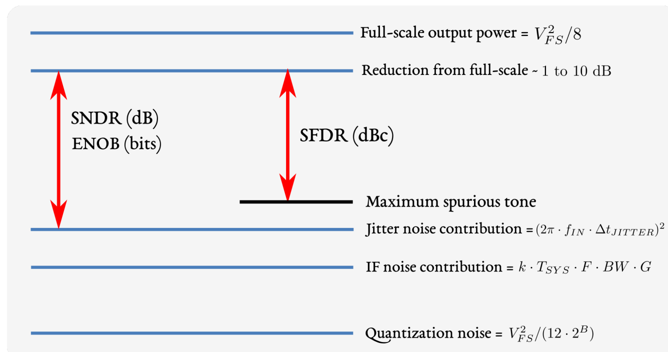

Fig. 8. Receiver dynamic range contributions. A receiver with a wide dynamic range is able to handle high in-band power levels. Although there are several techniques to increase the dynamic range of a digital receiver [76, 85, 86], it is primarily decided by the choice of the ADC.

quantization noise power in order to guarantee dithering the LSB and to preclude any hysteretic effects. Jitter noise from the sample clock and RF waveform can further degrade the noise floor at the output of the ADC [87]. The resulting SNDR, or ENOB, establishes the useful dynamic range of the receiver prior to any digital signal processing gain. The maximum power of any spurious tone within the full Nyquist bandwidth then defines the spurious free dynamic range (SFDR).

Many of these narrowband principles are not accurate for few-bit or monobit ADCs [77]. For example, the conventional rule-of-thumb that ADC output SNDR increases by about 6.02 dB/bit for sinusoidal inputs, is only approximate for less than 4 bits and mostly invalid for the quantization of low-SNR signals. Also, two-tone intermodulation distortion is a significant issue for ADCs with less than 4 bits operating in the presence of strong in-band interfering signals. Lastly, if the ADC sample rate is not sufficiently high, the noise floor at the ADC output increases since wideband noise will fold into the bandwidth of the ADC.

E. SAR Processing of Communication Waveforms

A substantial amount of recent research has been devoted to joint communication and radar sensing (JCRS) system design [88–90]. Applications at the higher mmWave band frequencies between 70 to 100 GHz include environmental sensing for autonomous vehicles [15, 91]. In some designs the radar and communication functions proceed along separate paths through the receive chain. Other designs strive to implement both functions on a common platform to reduce system cost, size, weight and power (SWAP) [15, 92]. In systems with the available hardware design flexibility, a powerful approach is to jointly optimize the transmit waveform and the receive filter such that constraints on power amplifier outputs and radar detection performance are satisfied [16]. Other schemes for JCRS leverage a full-duplex capability that allows for the simultaneously transmitting and receiving signals [93]. Novel approaches for cancelling the self-interference between transmit and receive antennas are described in [94–98]. The IEEE 802.11ad wireless standard for 60GHz has also been explored for JCRS because of its available 2 GHz bandwidth [91, 99–102]. Some recent wideband JCRS designs employ intelligent reflecting surfaces for non-line-of-sight (NLoS) sensing and communications [103–105].

As described previously, the matched filter is the optimal detector for a single target with known impulse response in additive white Gaussian noise since it maximizes SNR at the output. However, matched filtering waveforms that use typical modulations for wideband digital communications, such as Phase Shift Keying (PSK) or OFDM, can result in high range sidelobes that mask nearby weak targets. In these scenarios matched filtering is suboptimal and a mis-matched filter is preferred.

To eliminate the effects of masking, the receive filter must be adaptively estimated from the received signal independently for every delay bin. The re-iterative minimum mean-square error (RMMSE) algorithm described in [106, 107] alternates between estimating the true range profile impulse response and the respective receive filters. For every delay bin k the RMMSE algorithm minimizes the standard minimum mean-square error (MMSE) cost function,

$$J(k) = \mathbb{E}\{|x(k) - \mathbf{w}^H(k)\mathbf{y}(k)|^2\}, \tag{36}$$

where $x(k)$ is the sample of the range profile to be estimated, $\mathbf{y}(k)$ is a blocked vector of received signal samples, $\mathbf{w}(k)$ is the adaptive filter for the kth bin, and $\mathbb{E}\{\cdot\}$ is the statistical expectation operator. The optimal MMSE filter that minimizes $J(k)$ is the standard Wiener solution,

$$\mathbf{w}(k) = (\mathbb{E}\{\mathbf{y}(k)\mathbf{y}(k)^H\})^{-1}\mathbb{E}\{\mathbf{y}(k)x^*(k)\}. \tag{37}$$

More approaches to adaptive filtering in the range domain include for ISAR, interferometric SAR (InSAR), and interferometric ISAR (InISAR) applications [108, 109]. Additional methods for range processing adaptively subtract off the effects of large targets via the CLEAN algorithm [110, 111].

VI. SA CHANNEL SOUNDING

Communication at millimeter-wave frequencies with high bandwidths and high data transfer rates is enabling a new era of wireless applications. To effectively utilize the wider channel capacities available at millimeter wave frequencies the signal propagation environment must be comprehensively analyzed. Multipath signals at the receiver created by numerous propagation paths can significantly increase bit error rate and degrade data transfer performance. Alternatively, multipath can be leveraged to improve spatial diversity and to enable multiple-input multiple-output (MIMO) communications. The most important method for characterizing the signal propagation environment is channel sounding. Channel sounding refers to the process of estimating the impulse response of a communication channel and yields information on the source of signal echoes caused by reflections, the extent of diffuse scattering and diffraction, and the amount of shadow effects or signal blocking created by stationary objects or moving people and vehicles in the scene.

To illustrate the impact of multipath consider the case where two signals arrive at the receiver. The direct path signal is $V_{\mathrm{D}}(t) = \cos(\omega_0 t)$. The scattered multipath signal is $V_{\mathrm{R}}(t) = \rho\cos(\omega_0(t-\tau)) = \rho\cos(\omega_0 t + \phi)$, where $\phi = -\omega_0\tau$ and ρ and τ are random variables. The complete signal $V_{\mathrm{RX}}(t)$ at the receiver is given by the phasor sum shown in Fig. 9,

$$\begin{aligned} V_{\mathrm{RX}}(t) &= \cos(\omega_0 t) + \rho\cos(\omega_0 t + \phi) \\ &= \beta\cos(\omega_0 t + \theta). \end{aligned} \tag{38}$$

The path loss β^2 and phase of the received signal are given by,

$$\beta^2 = \frac{P_{\mathrm{RX}}}{P_{\mathrm{TX}}} = 1 + 2\rho\cos\phi + \rho^2, \tag{39}$$

$$\theta = \tan^{-1}\left[\frac{\rho\sin\phi}{1+\rho\cos\phi}\right], \tag{40}$$

where, P_{TX} and P_{RX} are transmit and received powers, respectively. For signals that are highly correlated $\rho \approx 1$ and the destructive sum of the two incident signals at the receiver results in high path loss if the signals are close to 180° out of phase as shown in Fig. 10 (data in this section is available on GitHub [112]). Characterizing the severity of multipath scattering in a wireless channel is the primary motivation behind channel sounding which is described next.

A. Frequency Domain SA Sounders

The simplest channel sounding systems rely on directional antennas placed in a bistatic geometry to transmit and receive a probe signal that is matched filtered to produce an estimate of the channel impulse response. The concept of synthesizing an aperture larger than the physical size of an antenna can be leveraged to yield improved angular resolution performance for channel sounders [113–121]. Furthermore, a higher measurement bandwidth than the instantaneous bandwidth of the signal can be synthesized to improve

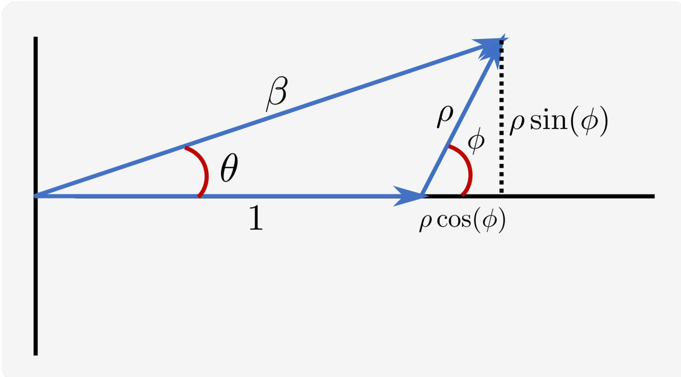

Fig. 9. Two-ray multipath geometry. The complex line-of-sight (LOS) signal and a multipath replica combine as vectors in the complex plane.

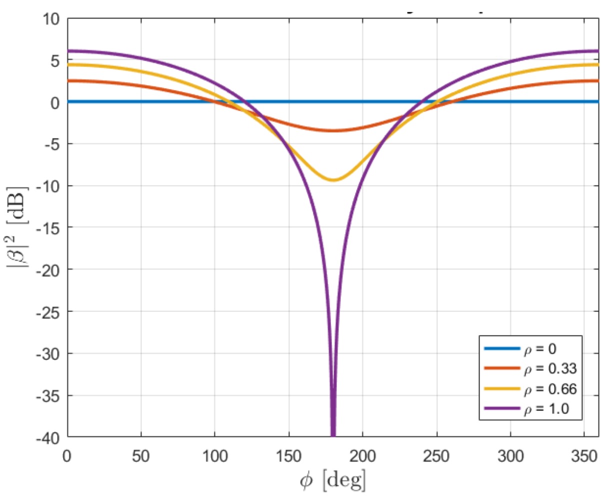

Fig. 10. Receiver impact of multipath. When the direct LOS signal and a delayed maultipath replica are out-of-phase the result can be a deep null in received power due to destructive interference.

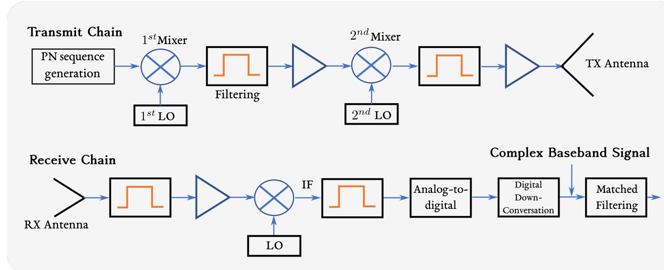

Fig. 11. Channel sounder architecture. The baseline channel sounder configuration is a transmit and receive antenna in a bistatic configuration.

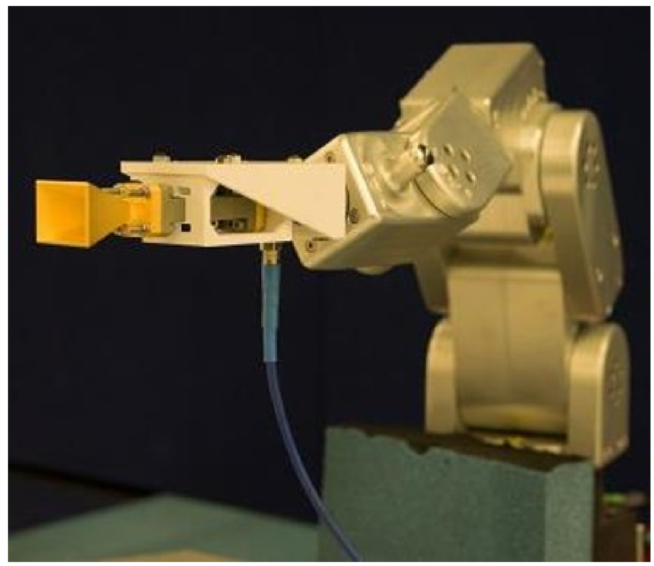

Fig. 12. Receive antenna mounted on robot. The robot moves the antenna to precise locations in space to measure the spatial distribution of signal phase. These coherent measurements form the basis for a synthetic aperture.

delay resolution. Fig. 11 illustrates the architecture of a typical channel sounding system.

The nominal angular resolution of the sounder in Fig. 11 is equal to the receive antenna beamwidth, or $\Delta\theta = \lambda/D$, where λ represents wavelength and D is the dimension of the antenna in the principal plane. The delay resolution $\Delta\tau$ is inversely proportional to the signal bandwidth B, or $\Delta\tau = 1/B$. An SA channel sounder with greater resolution in both the angular and delay domains can be constructed by attaching the receive antenna to a precise mechanical positioner such as the robot arm shown in Fig. 12.

The premise behind a SA channel sounder is that the mechanical positioner moves the receive antenna (also called a probe) to points along a spatial sampling lattice. In the most general sense, the lattice can be arbitrary but in typical cases it is chosen to be planar or cylindrical. At each spatial sample point, the receiver digitizes the antenna output and writes the data to memory. The availability of the digitized receive signal at every spatial sample location allows the SA to emulate the functionality of an element-level digital beamforming (DBF) array.

A conventional heterodyne receiver can be used behind the antenna to detect the signal or a vector network analyzer (VNA). If a VNA is used, then a discrete frequency grid is specified of carrier frequencies. VNA receivers have been investigated in a number of channel sounder configurations. For example, wideband channel measurements using a VNA are discussed in [122, 123]. A cubic SA with a VNA is utilized in [124] to estimate LoS and NLoS propagation paths in an indoor environment. A long range wideband sounder using a VNA was described in [125] for outdoor measurements.

The VNA-based SA channel sounder developed at the National Institute of Standards and Technology (NIST) and described in [126, 127] radiates 1351 sinusoidal tones spaced 10 MHz apart in the range from 26.5 to 40 GHz and measures S_{21} parameters at each spatial sample. Thus, the total synthesized measurement bandwidth B is 13.5 GHz even though each radiated tone is very narrowband. An advantage of the VNA sounding approach is that the channel is illuminated with a uniform power spectral density since each radiated sinusoidal tone is of equal amplitude. With some channel sounding waveform modulations, such as pseudo-random noise sequences, the shape of the signal spectrum allocates more power to some frequencies than to others.

After beamforming the wideband data towards a specified direction, a power delay profile (PDP) is generated that represents the beam's temporal output. The resulting delay resolution of the system is approximately $1/B$ or 2.2 cm and this value is much less than the delay resolution available using a typical narrowband channel sounder that radiates an instantaneous signal bandwidth in the range of 1-3% of the carrier. The total unambiguous delay T_{dur} that can be measured by the SA is determined by the frequency step size Δf_{sa} as in $T_{\text{dur}} = 1/\Delta f_{\text{sa}}$. An example of a directional PDP is shown in Fig. 13 for sounding data measured in an industrial environment

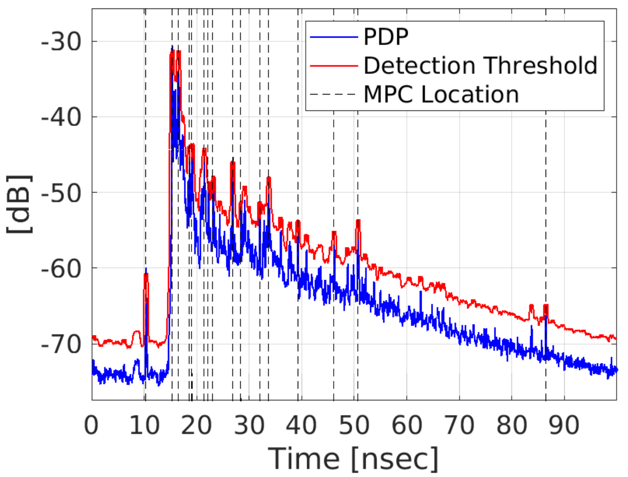

Fig. 13. Directional PDP showing normalized power received (path loss) as a function of delay for a specified look direction. The long fading time constant of diffuse multipath is clearly evident for this wireless scenario.

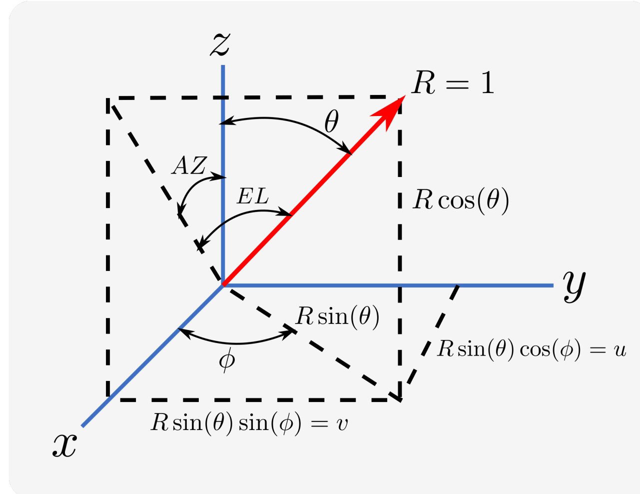

Fig. 14. Array coordinate systems. The beam pattern is scan-angle invariant when computed in sine space or uv-coordinates.

with dense multipath. A frequency varying phase taper was applied across the aperture to steer the beamformed output to the direction $-0.8°$ azimuth and $-0.8°$ elevation and an inverse Discrete Fourier Transform (DFT) was used to transform the frequency domain data to the delay domain. The blue curve represents signal path loss (or normalized receive power) as a function of delay and the red curve is an adaptive threshold that rides over the data. Data values that exceed the threshold are multipath detections and are marked using a dashed line.

To avoid any spatial aliasing, the maximum distance between points on the spatial sampling grid of the SA is chosen to be $\lambda/2$ at the highest frequency of the measurement bandwidth. If using conventional beamforming or Fourier techniques to coherently combine the received data across the aperture, the nominal angular resolution of the system is equal to the beamwidth, or $\theta_B = \lambda/D$ for a planar aperture. An important observation is that the size, D, of a SA can be made almost arbitrarily large. For example, the baseline NIST SA channel sounding configuration is a square 35-by-35 grid of spatial samples that yields a half power beamwidth of 2.9° at 40 GHz. This aperture contains 1225 spatial sample points which would be a challenge to build in hardware. Aside from the benefits of finer angle and delay resolution, SA channel sounders have other desirable features that will be described next.

1) Detection Range: The Friis equation defined in [4] can be used to compute the maximum detection range possible given the transmit and receive antennas of a channel sounder. In a LoS geometry, the Friis equation for detection range is

$$R^2 = \frac{P_t G A_e}{4\pi S_{\min}}, \tag{41}$$

where P_t refers to the transmit power, R is the distance between antennas, G is the power gain of the transmit antenna, A_e is the effective aperture area on receive, and $S_{\min}$ is the minimum detectable signal level in the receiver. In a multipath or non-LoS scenario, the Friis equation yields

$$R_1^2 R_2^2 = \frac{P_t G A_e \sigma}{(4\pi)^2 S_{\min}}, \tag{42}$$

where R_1 denotes the distance from the transmit antenna to an object with backscatter area σ (in units of m^2), and R_2 is the distance from the scatterer to the receive aperture. Both equations show that to maximize detection range the effective area of the receive aperture, A_e, should be as big as possible, which is most practical using a SA. With a SA, the number of spatial sample points can be made large and, by coherently combining the signals received across all the samples, A_e can be maximized subject only to constraints such as the available measurement time or the range of motion of the mechanical positioner.

2) Array Coordinate Systems: Fig. 14 shows the angles used to describe beam scanning directions for three common array coordinate systems. In this illustration, the array lies in the x-y plane and the z-axis points along the normal to the plane of the array, also known as the boresight direction. In a spherical coordinate system, the angles θ and ϕ define points on the surface of the forward unit hemisphere. The angle θ is measured from boresight and ϕ extends to the plane of scan from the x-axis. The projection of points from the forward hemisphere onto the xy plane yields the coordinate axes labeled as u and v. The coordinates u and v can also be used to describe beam directions and are known as sine-space coordinates. The relations used to transform angles between the spherical, azimuth (AZ)/elevation (EL), and sine-space coordinate systems are defined below.

$$u = \sin\theta\cos\phi, \quad v = \sin\theta\sin\phi \tag{43}$$
$$u = \cos EL \sin AZ, \quad v = \sin EL \tag{44}$$
$$\sin^2\theta = u^2 + v^2, \quad \tan\phi = v/u \tag{45}$$
$$\cos\theta = \cos EL \cos AZ, \quad \tan\phi = \tan EL/\sin AZ \tag{46}$$
$$\tan AZ = u/\sqrt{1-u^2-v^2}, \quad \sin EL = v \tag{47}$$
$$\tan AZ = \tan\theta\cos\phi, \quad \sin EL = \sin\theta\sin\phi \tag{48}$$

where $0 \le \theta \le \pi$ and $-\pi \le \phi \le \pi$. Note that azimuth angle is defined with respect to the boresight axis and elevation angle is defined with respect to the projection onto the xz plane.

3) Dynamic Range and Mutual Coupling: In typical hardware phased arrays, an analog beamforming network coherently combines the RF signals received at each array element before downconversion to baseband and digitization. One consequence of this architecture is that the coherent integration gain due to beamforming (equal to $10\log_{10} N$, where N is the number of array elements) can limit the dynamic range of the system. For example, if a strong signal is incident on an array of 1000 elements then the 30 dB of additional gain at the output of the beamformer may cause the ADC to saturate. With a SA however, the signal received at each spatial sample position is digitized separately and the only additional gain before the ADC is the gain of the receive probe. This architecture maximizes system dynamic range, especially if a low gain probe is used, because there is no coherent integration gain before the digitizer. Low gain antennas are desirable as probes in SAs because the wider antenna beam allows for higher array factor scan angles.

An additional benefit due to the fact that SAs digitize each spatial sample position sequentially is that there is no mutual coupling created between array elements that can affect the overall array beampattern. With hardware arrays, the pattern of each array element is perturbed once the element is embedded in the array structure. For example, the elements in the interior of the array will exhibit a different pattern compared to the elements at the edge of the array, even if all the element patterns are identical outside the array. This phenomenon is caused by currents that re-radiate between the elements. Mutual coupling can create angle estimation and beam pointing errors in hardware arrays but does not exist in SAs.

B. *Frequency and Scanning Behavior of the Array Factor*

The far-field response in spherical coordinates (θ, ϕ) for an array of $M \times N$ homogeneous elements located in the xy plane is given by,

$$B(\theta,\phi) = E(\theta,\phi) \sum_{m=0}^{M-1} \sum_{n=0}^{N-1} w_{mn} e^{\mathrm{j}k(x_m \sin\theta\cos\phi + y_n \sin\theta\sin\phi)}, \quad (49)$$

where $E(\theta,\phi)$ is the array element pattern, the wavenumber $k = 2\pi/\lambda$, λ is the operating wavelength, and w_{mn} is the array element weighting. If the array elements are uniformly spaced on a rectangular grid then the element locations are given by $x_m = md_x$ and $y_n = nd_y$ where d_x and d_y denote the distance between elements in the x and y directions. This equation can be rewritten as a 2-D spatial Fourier Transform by using the sine space coordinates $u = \sin\theta\cos\phi$ and $v = \sin\theta\sin\phi$,

$$B(u,v) = E(u,v) \sum_{m=0}^{M-1} \sum_{n=0}^{N-1} w_{mn} e^{\mathrm{j}k(md_x u + nd_y v)}. \quad (50)$$

The summation term is known as the array factor. The array factor repeats in the u dimension with period λ/d_x and repeats in the v dimension with period λ/d_y. A single period in uv space of the array factor is equal to the rectangular region $-0.5\lambda/d_x \le u < 0.5\lambda/d_x$ and $-0.5\lambda/d_y \le v < 0.5\lambda/d_y$. The visible region of the array factor that exists in physical space corresponds to the interior of the unit circle $u^2 + v^2 \le 1$. Replicas of the mainlobe outside the unit circle are known as grating lobes. The Nyquist spatial sampling rate that avoids spatial aliasing or grating lobes is given by $d_x = d_y = \lambda/2$. If the element spacing is greater than $\lambda/2$ then the array is undersampled and the grating lobes move closer to the unit circle and may even enter the visible region. If the element spacing is less than $\lambda/2$ then the array is oversampled and the grating lobes move farther away from the unit circle. The peak of the mainbeam depends only on the number of array elements and is equal to $10\log_{10}(MN)$.

All of the properties of Fourier Transforms apply to the array factor and in particular the Fourier shift and the Fourier scaling properties. The Fourier shift property is relevant when the main beam is steered to a direction (u_0, v_0). Beam steering is accomplished by applying the linear phase taper $e^{-\mathrm{j}k(md_x u_0 + nd_y v_0)}$ across the aperture. The main beam will shift by an angular distance equal to the slope of the linear phase taper in the u and v directions. Steering the main beam for a single frequency is a linear transformation that does not affect the amplitude of the array factor or the shape of the main beam. When the beam scans, sidelobes that were originally outside the unit circle in the invisible region of uv space will enter the visible region and therefore the sidelobe structure of the beam changes.

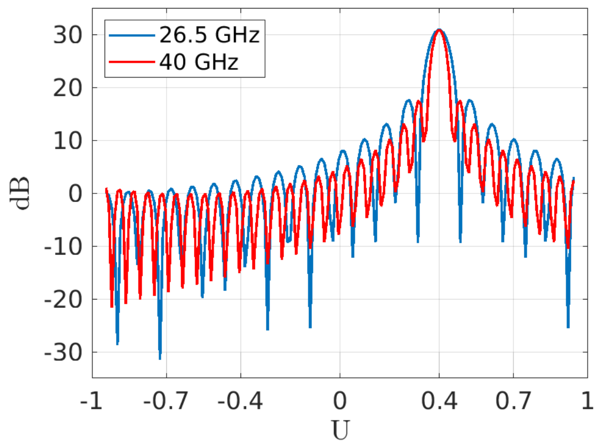

Fig. 15. U-Cut of beampattern illustrating Fourier scaling property. Since array element spacing is fixed, the width of angular lobes decreases as the frequency increases because array becomes electrically larger.

In wideband regimes where the linear phase taper is computed for a single center frequency but applied to the aperture over a wider bandwidth, then the main beam will squint, or point to different directions, as the operating frequency changes. Beam squint is an undesired effect that can be mitigated by using true time delay beam steering or a frequency invariant beamformer [128]. True time delay beam steering applies a frequency independent time delay or a frequency dependent linear phase shift between array elements to steer the beam and can be easily implemented on SAs.

The Fourier scaling property states that changing the sample spacing of a 2D discrete sequence $h(m,n)$ expands or contracts the output of the Fourier transform $H(u,v)$ according to

$$H\left(\frac{u}{a}, \frac{v}{b}\right) \iff \frac{1}{|ab|} h(am, bn). \quad (51)$$

This property implies that if the physical spacing between array elements is held fixed while the operating frequency decreases, then the width of every angular lobe in the beampattern (main beam and sidelobes alike) will increase. Conversely, if the element spacing is held fixed while the frequency increases, then the width of every angular lobe decreases. Consequently, a SA of fixed dimensions attains higher angular resolution at 40 GHz than at 26.5 GHz due to the narrower width of the main beam (approximately equal to λ/D radians, where D is the largest dimension of the aperture in the principal planes). Fig. 15 illustrates the Fourier scaling property by comparing a u-dimension cut of the array beampattern for 26.5 and 40 GHz with the main beam steered to $(u = 0.4, v = 0.3)$. In channel sounding applications it is important to maintain a frequency invariant array response such that it does not obfuscate the estimated channel frequency response.

1) Beam Squint in Wideband Arrays: As described by (49) or (50) forming the coherent sum of the signals collected across the SA forms a directional beam in space. This beam may be steered to different directions by applying the appropriate phase shift between successive array elements. To steer the beam in the direction (θ, ϕ) the phase shift applied at the mnth array element is given by

$$\psi_{mn}(\theta,\phi) = \frac{2\pi}{\lambda}(x_m \sin\theta\cos\phi + y_n \sin\theta\sin\phi), \quad (52)$$

where x_m denotes the x-coordinate of the element's location and y_m denotes the y-coordinate. For the case of a SA with a VNA acting as the signal receiver the exact phase shift required can be applied in the post-processing since the received signal is a single

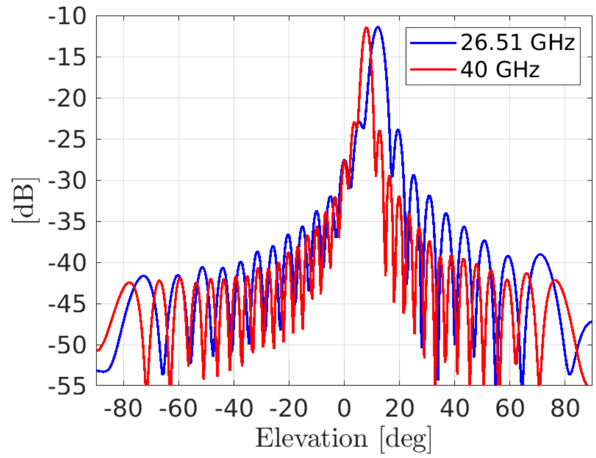

Fig. 16. Beampattern elevation cut showing beam squint. The beam-steering phase taper computed for 26.51 GHz is also applied at 40 GHz and as a result the beam pointing direction changes.

monochromatic sinusoidal tone for each measurement frequency. If frequency is substituted into (52) rather than wavelength then it is clear that the required steering phase at any array element varies linearly with frequency [128].

$$\psi_{mn}(\theta,\phi) = \frac{2\pi f}{c}(x_m \sin\theta\cos\phi + y_n \sin\theta\sin\phi) \quad (53)$$
$$= \frac{\omega}{c}(x_m \sin\theta\cos\phi + y_n \sin\theta\sin\phi). \quad (54)$$

If the steering phase is computed for a single frequency only and the frequency of the received signal is allowed to vary without adjusting the steering phase accordingly, then the beam squints, or points in a slightly different direction for each frequency. Fig. 16 illustrates the effect of beam squint using measured NIST data collected in a conference room setting. In this case, a steering vector is computed for 26.51 GHz and applied to the data measured at 40 GHz. The elevation cut shown in the plot illustrates how the beam squints, or changes pointing direction because the computed steering phase is not matched to the frequency of the received signal. Beam squint can have an impact in millimeter-wave systems as described in [129].

To implement true time-delay beamforming, if the phase shift $\psi_{mn}(\theta_0,\phi_0)$ is computed exactly for an initial frequency ω_0 then at all other frequencies a differential phase shift proportional to the frequency difference should be applied. The steering phase versus frequency is then given by

$$\psi_{mn}(\omega;\theta_0,\phi_0) = \psi_{mn}(\omega_0;\theta_0,\phi_0)[1+(\omega-\omega_0)/\omega_0] \quad (55)$$
$$= \psi_{mn}(\omega_0;\theta_0,\phi_0)\omega/\omega_0. \quad (56)$$

The slope of the linear phase ramp in (55) corresponds to a time delay of

$$\tau = \frac{d\psi}{d\omega} = \frac{\psi_{mn}(\omega_0;\theta_0,\phi_0)}{\omega_0} \quad (57)$$
$$= \frac{1}{c}(x_m \sin\theta_0\cos\phi_0 + y_n \sin\theta_0\sin\phi_0). \quad (58)$$

The wideband processing algorithm described in the next section eliminates beam squint by applying a phase shift proportional to frequency, or equivalently a time delay, at each array element to steer the beam.

2) Wideband Power Angle Delay Profile (PADP): True time delay beam steering refers to the practice of inserting a pure time delay instead of a phase shift behind each array element to steer the beam in wideband arrays. True time delay beam steering can be implemented on wideband SAs to avoid beam squint by applying a frequency dependent phase taper to the array output vector as described in (55). After computing the dot product of the beam steering phase taper and the array output vector for every frequency, an Inverse Fourier Transform is computed to yield the beam output power received from the direction (θ_0,ϕ_0) as a function of delay. This beam output is also known as the PDP for the direction (θ_0,ϕ_0). The process is summarized in Algorithm 1 below. Note that a frequency invariant beamformer may replace the phase steering vectors $\mathbf{w}(\omega_k;u_0,v_0)$ with optimized weight vectors computed at every frequency for the desired beam-steering direction.

Algorithm 1 PADP and delay slice creation

Input: Array output vector $\mathbf{y}(\omega_k)$ at each frequency ω_k for $k=0,\ldots,S-1$ and desired beam pointing direction (u_0,v_0)

1: Compute the phase steering vector for each frequency, $\mathbf{w}(\omega_k;u_0,v_0)$.
2: Beamform the array output vector $\mathbf{y}(\omega_k)$ at each frequency by forming the dot product $b(\omega_k;u_0,v_0) = \mathbf{w}(\omega_k;u_0,v_0)^H\mathbf{y}(\omega_k)$
3: Compute the Inverse Fourier Transform (temporal) to obtain the beam output (directional PDP), $x(\tau_k;u_0,v_0) = IFT[b(\omega_k;u_0,v_0)]$
4: To reduce high-frequency, time-domain ripple in wide bandwidth measurements and to increase sampling resolution, compute a window function c_k of length S with low sidelobes, e.g. Hamming window. Then zero-pad the sequence $c_k b(\omega_k;u_0,v_0)$ to L times its original length before computing the IDFT
5: For a fixed delay, $\tau=\tau_0$, $x(\tau_0;u,v)$ is the spatial frequency spectrum of all signal sources impinging on the array (also called a delay slice) and can be used to estimate angles of arrival

Outputs: PDP $x(\tau;u_0,v_0)$ in the fixed direction (u_0,v_0). Delay slice $x(\tau_0;u,v)$ at the fixed delay τ_0.

3) Spatial Wideband Effect: In large phased arrays with many elements, the propagation time of an impinging electromagnetic wave travelling across the aperture is non-negligible. More precisely, if the distance between elements on opposite corners of the array is large compared to the carrier wavelength, then there will be noticeable offsets between the signal arrival times across the array elements. When all the array element signals are coherently combined during the beamforming operation, the effect of the non-uniform delay offsets will be to limit the instantaneous bandwidth of the array.

For a uniform linear array of length L, the time τ required to fill the aperture with energy for radiation arriving from an angle θ_0 is given by

$$\tau = \frac{L}{c}\sin\theta_0. \quad (59)$$

For a pulsed waveform, as the array mainbeam is scanned away from boresight, each spectral component is steered to a slightly different direction. To determine the overall effect on antenna gain, it is necessary to add the far-field patterns of all the individual spectral components. The result is that a loss of 0.8 dB in energy on target occurs due to frequency-scanned spectral components when the mainbeam is scanned to an angle of 60° and the pulse width is equal to the array fill time; or equivalently the signal bandwidth is equal to $1/\tau$ [73].

Thus a large hardware array that achieves high angular resolution will be necessarily bandwidth-limited and not capable of supporting delay resolutions less than the array fill time. With VNA-based synthetic apertures however, high angle and delay resolutions are simultaneously compatible since the VNA inherently measures

S-parameters (signal ratios) at each spatial location and the beamforming operation is carried out in post-processing. A tutorial description of the spatial wideband effect is provided in [130].

C. Delay Resolution

The frequency range measured at each spatial sample of the SA determines the synthesized bandwidth of the channel measurement. The delay resolution of the channel measurement is equal to the reciprocal of the synthesized bandwidth. For example, if the total bandwidth is $f_{\mathrm{BW}} = 13.5$ GHz between $f_{\min} = 26.5$ GHz and $f_{\max} = 40$ GHz, then the corresponding delay resolution is $\Delta T = 0.074$ ns, which yields a distance resolution of 2.2 cm. The maximum unambiguous delay extent that can be measured by the SA is equal to one over the increment between frequency samples. If, for example, the frequency step size is Δf = 10 MHz, this corresponds to a maximum unambiguous delay extent of T = 100 ns, or D = 29.96 meters. This frequency step size yields 1351 frequency samples within the synthesized 13.5 GHz bandwidth and 1351 delay samples within the total time duration of the power delay profiles. Thus, for this case, the temporal sampling rate of each PDP is equal to the measurement bandwidth, or f_{BW} = 13.5 GHz.

Since the ratio of the highest measurement frequency to the total measurement bandwidth is very nearly an integer, $40/13.5 = 2.96 \approx 3$, bandpass sampling considerations for the complex S_{21} parameters suggest that any aliasing due to sampling at a temporal rate equal to f_{BW} will be small. In general, aliasing is negligible if the complex sampling rate f_{sam} of the PDPs satisfies

$$f_{\mathrm{sam}} \geq q f_{\mathrm{BW}}, \quad 1 \leq q \leq \left\lfloor \frac{f_{\max}}{f_{\mathrm{BW}}} \right\rfloor. \tag{60}$$

The wideband true-time-delay algorithm can be leveraged to evaluate delay slices of the four-dimensional channel impulse response by computing directional PDPs at directions (θ_k, ϕ_k) or (u_k, v_k) on a discrete angular grid of $k = 0, \ldots, K-1$ angles that encompass the entire forward hemisphere. If these PDPs are evaluated over all the angles at the fixed delay $\tau = \tau_m$, then $x(\tau_m; u, v)$ is the spatial frequency spectrum of all signal sources impinging on the array and can be used to estimate strong angles of arrival for the delay bin τ_m. The equation for evaluating the Inverse Discrete Fourier Transform of the beam output $b(f_s; u_k, v_k)$ at only the mth delay bin τ_m is

$$x(\tau_m; u_k, v_k) = \frac{1}{S} \sum_{s=0}^{S-1} b(f_s, u_k, v_k) e^{\mathrm{j}2\pi ms/S}, \tag{61}$$

where S is the total number of frequency samples f_s and $0 \leq m \leq S-1$. Fig. 18 and Fig. 19 illustrate delay slices for measurements taken in a utility plant at the NIST Boulder campus. The utility plant environment is shown in Fig. 17. In these figures, we see the signal received from the utility plant environment as a function of azimuth and elevation for two different time delay values. The relative received power level is given by the color bar in dB. These delay slices show a detailed view of the angular power spectrum created by multipath scattering as a function of time.

Practical experience suggests that the delay slice algorithm is most effective when a candidate set of delay bins to search for multipath components is determined in advance. A particularly useful method for determining candidate delay bins is to integrate (using summation) each available delay slice $x(\tau_m; u, v)$ over all angles in order to compute the total energy received versus delay. This procedure yields an aggregate power delay profile $r(\tau_m)$ that describes the total energy

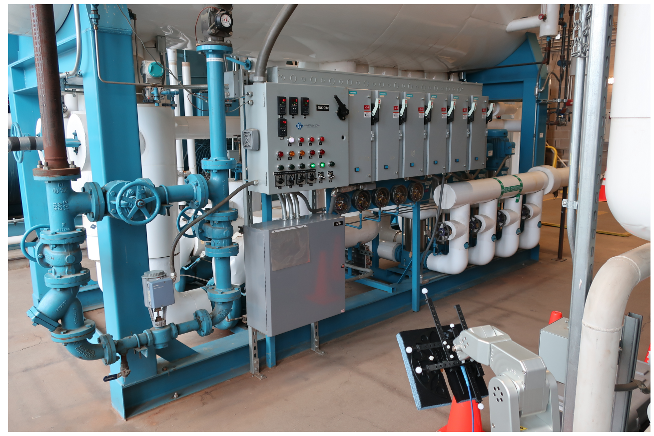

Fig. 17. NIST central utility plant (CUP). Channel sounding experiments in this location were conducted to characterize dense multipath scattering environments. Photo credit: NIST.

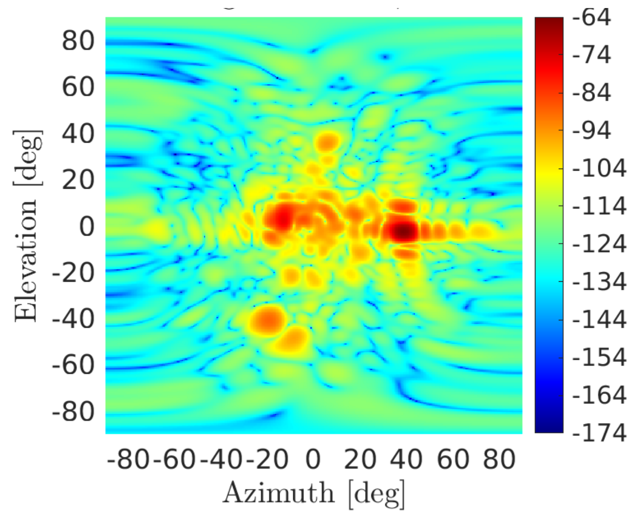

Fig. 18. Delay slice (dB) at 19.08 ns. A strong signal source is visible at 40° azimuth as well as lots of diffuse scattering.

impinging on the SA from the entire forward hemisphere as a function of delay,

$$r(\tau_m) = \sum_{k=0}^{K-1} |x(\tau_m; u_k, v_k)|^2. \tag{62}$$

If the summation is taken over a subset of (u_k, v_k) samples smaller than the entire forward hemisphere, then the total power received versus delay is computed for an angular sector.

D. Frequency Invariant Array Response

When the complex field of a propagating wave is incident on a phased array or crosses the observation plane of a SA, the beamformed array response will be angle and frequency dependent. To avoid distorting the estimated wireless channel it is desirable to equalize the array frequency response such that it is constrained along specified directions. Consider the field of a propagating monochromatic wave as a function of position $\mathbf{x}$ and time t given by, [131]

$$U(\mathbf{x}, t) = e^{\mathrm{j}2\pi(-\mathbf{v}^T\mathbf{x} + ft)}, \tag{63}$$

where $\mathbf{v}$ is the propagation direction (spatial frequency) vector and f is temporal frequency. The Helmholtz equation relates the spatial and temporal frequencies by $|f| = c/||\mathbf{v}||$, where c is the speed of

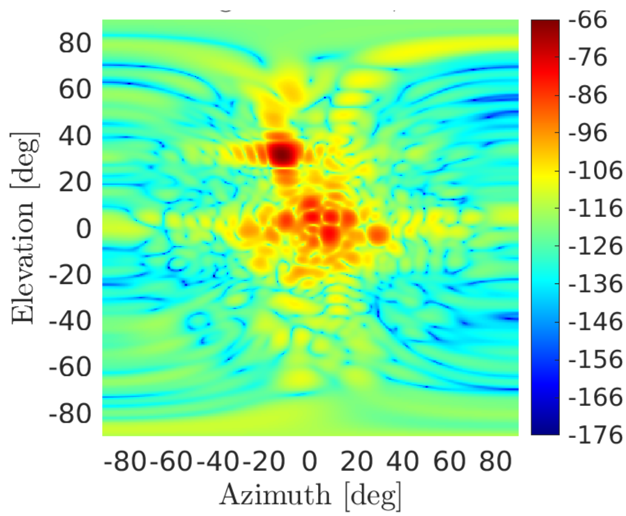

Fig. 19. Delay slice (dB) at 21.36 ns. A strong signal source is clearly visible at approximately 30° elevation. Many other specular returns are also visible near boresight.

propagation. The output of an antenna element at position $\mathbf{x}$ is the time function

$$y(t) = G(\mathbf{v}, f)U(\mathbf{x}, t), \tag{64}$$

where $G(\mathbf{v}, f)$is the complex gain of the element as a function of spatial and temporal frequency. The coherent sum of an array of N elements yields

$$s(t) = \sum_{k=0}^{N-1} G_k(\mathbf{v}, f)U(\mathbf{x}, t). \tag{65}$$

Consider a linear array with K elements where each element is a length-N FIR filter. Each element is located at kd_x where $d_x = \lambda/2$ at the highest frequency of interest to avoid grating lobes and $-K+1 \leq k \leq K-1$. The filter taps are spaced at nT intervals where $-N+1 \leq n \leq N-1$. The array pattern is then

$$H(\mathbf{v}, f) = \sum_k \sum_n c_{kn} e^{-\mathrm{j}2\pi(kv_x d_x + nfT)}. \tag{66}$$

where $\mathbf{v} = [v_x \quad v_y]^T$. This equation describes the 3D response of a 2D FIR filter and does not depend on v_y since the array has no extent in the y dimension. The array pattern is periodic in v_x and f, with period $1/T$ in f and period l/d_x in spatial frequency v_x. The tap spacing T should be chosen so that $1/T$ is larger than the desired instantaneous bandwidth of the array response.

Since (54) is linear in the filter coefficients c_{kn} even with arbitrary element locations, many common constraints can be expressed as upper bounds of convex functions of the coefficients. Consequently, the array pattern can be designed using convex optimization tools [132].

Another frequency invariant array architecture that avoids the use of temporal filtering behind each element is the use of sensor delay lines (SDLs). For planar sampling, SDLs are constructed by creating consecutive sample planes spaced along regular spatial intervals. For cylindrical sampling, SDLs can be constructed using concentric circular lattices. SDLs are particularly straightforward to implement for SA channel sounders that use a robot positioner. For example, if an initial planar lattice lives in the xy plane, then additional planar lattices would be created along the z-axis (boresight) dimension spaced a distance $\lambda/2$ or $\lambda/4$ apart. An optimized coefficient can be computed for each spatial sample in a 3-D SDL to create the frequency invariant array response [133, 134].

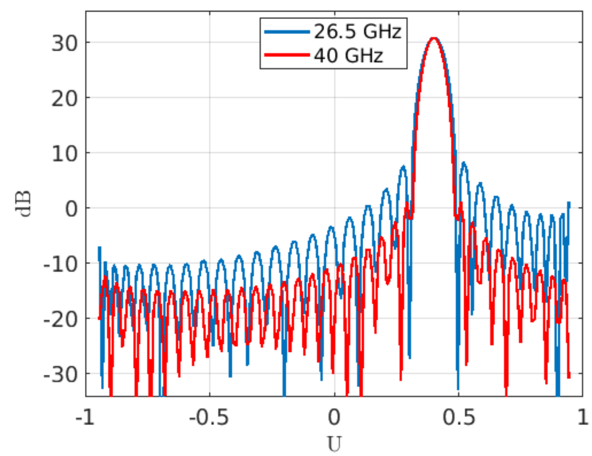

Fig. 20. Frequency invariant beampattern (dB) showing constant beamwidth and reduced sidelobes at 26.5 and 40 GHz for fixed array element spacing.

It is also possible to generate frequency invariant beampatterns by placing a filter bank behind each array element and partitioning the wideband signal spectrum into sub-bands. Then each sub-band can be optimized independently using narrowband techniques to create the frequency invariant array response as descibed in [135, 136]. The filter banks used could be as simple as a Discrete Fourier Transform Filter Bank (DFTFB) or more complicated designs including Cosine Modulated Filter Banks (CMFBs). One advantage of this approach is that the sub-band processing can be implemented at a lower sample rate than the digitized signal at the filter bank input.

With a frequency domain channel sounder one can design an optimized beamformer for every beam-steering direction at each discrete measurement frequency as described in [4]. Fig. 20 illustrates the case for a beamformer that has been designed to reduce ambient sidelobe levels while also maintaining a constant beamwidth over the frequency range from 26.5 to 40 GHz. Fig. 21 shows constant beamwidth maintained over the entire bandwidth. In the absence of any optimized beamforming, the width of the mainbeam would decrease by 33% from 26.5 to 40 GHz.

Note that in a conventional narrowband or wideband array design, a prototype array pattern is designed at boresight, and then used to generate beam patterns steered to other directions by applying direction-dependent phase shifts (narrowband) or time delays (wideband) to the signal at each array element. The result is a set of array patterns that at each temporal frequency are spatial-frequency-shifted copies of the prototype pattern. This approach is computationally efficient but not truly optimal in the sense that the beam pattern has not been jointly optimized for beam-steered and frequency response.

E. Sparse Sampling Lattices

An advantage of using a precision robot to position the receive antenna is that almost arbitrary spatial sampling lattices can be created. The simplest case is to create a planar lattice such as previously described. However, rotationally symmetric lattices such as circular, cylindrical, or spherical are also desirable because they offer omnidirectional signal reception.

Sparse sampling lattices are especially useful since they may reduce the data acquisition time required for channel sounding or the hardware complexity of phased arrays. However, sparsely sampled lattices on a regular grid introduce grating lobes in the beampattern as shown in Fig. 22 (model code and data publically available [137]). Grating lobes are functionally equivalent to high sidelobe levels and

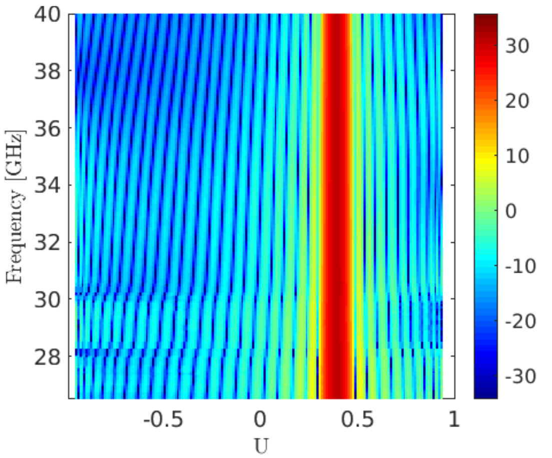

Fig. 21. Frequency invariant beampattern (dB) showing constant beamwidth across entire bandwidth from 26.5 to 40 GHz.

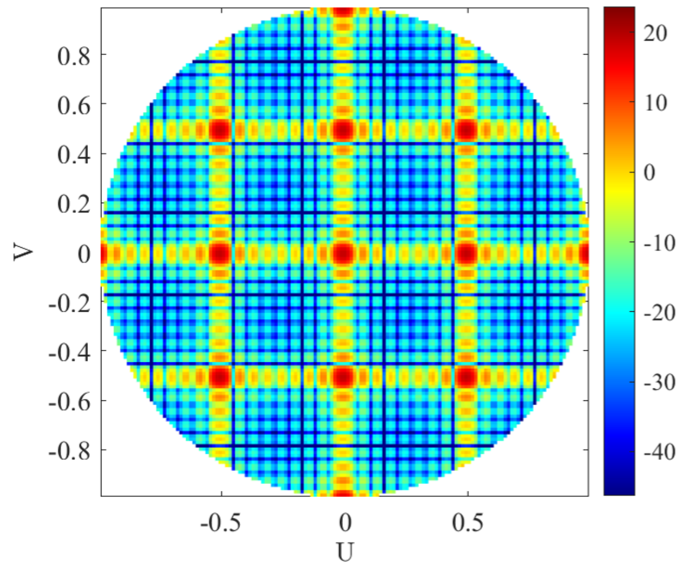

Fig. 22. Grating lobes in array pattern (dB) due to a sparse sampling grid. The grating lobes are essentially copies of the mainbeam and create spatial ambiguities when estimating angles of arrival.

create spatial ambiguities that make it difficult to determine the correct angles of arrival for measured signals. The search space for optimizing the location of spatial samples in a sparse array is vast, so heuristic search algorithms such as genetic optimization and simulated annealing have been applied to this problem. The use of quantum computing for solving sparse radar images has also been theorized and studied for its potential increase in computational capability.

One simple approach for mitigating grating lobes in a sparse lattice is to perturb the regularly spaced grid by applying a random offset to each spatial sample as shown in Fig. 23. The red circles correspond to the original sparse lattice and the green circles correspond to the perturbed lattice with random position offsets. The random displacements have the effect of disrupting any periodicity across the spatial samples that contributes to grating lobes. The end result is shown in Fig. 24 where the peak sidelobe level has been reduced to at least 13 dB below the peak of the mainbeam, shown steered to boresight.

Other approaches investigated for sparse array design include simulated annealing and genetic algorithms. Simulated annealing is a stochastic optimization method analogous to the manner in which a metal cools and anneals [138]. The algorithm seeks to minimize an energy function which for sparse arrays is set proportional to the peak sidelobe level. At each algorithm iteration, the location of array elements is randomized by moving one element at a time. The peak sidelobe level of the perturbed array is found and compared to the best solution of the last iteration. The new solution is accepted if it lowers the peak sidelobe level, or it may also be accepted with some finite probability if it raises the sidelobe level. In this way, the algorithm is less likely to be trapped in a local minimum. As the cost function is progressively minimized, the probability of accepting an inferior solution is reduced and ultimately the algorithm converges to a solution that may be close to optimal, provided the optimization parameters are well chosen. Simulated annealing has been applied to the optimization of sparse lattices in [139–142]

Genetic algorithms iteratively operate on the individuals in a population [143, 144]. Each member of the population represents a potential solution to the optimization problem. Initially, the population is randomly generated. The individuals are evaluated by means of a fitness function and then either retained or replaced. New individuals are created through either a cross-over operation or a mutation. Genetic optimization has been applied to the layout of sparse arrays in [145–147].

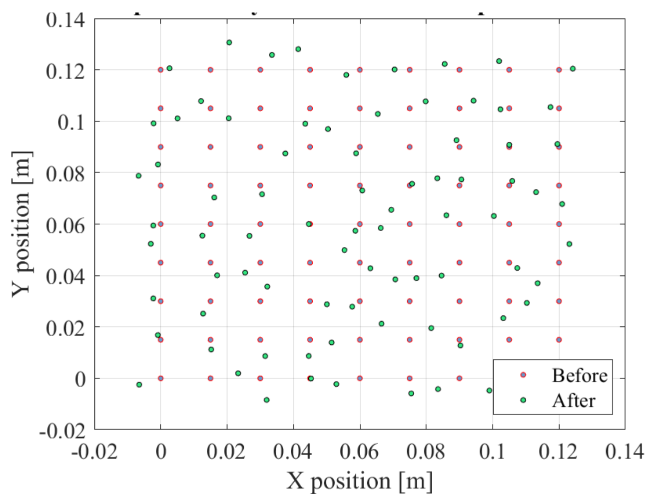

Fig. 23. Randomized and regularly sampled sparse array. The random position offsets applied to each array element break up the spatial periodicity that contributes to grating lobes.

Sparse Fourier Transform (SFT) algorithms have been investigated for several applications including fast Global Positioning System (GPS) receivers, wide-band spectrum sensing, and multidimensional radar signal processing [148–152]. In all SFT algorithms, the reduction of sample and computational complexity is achieved by reducing the input data samples using a well-designed, randomized subsampling procedure [153]. The significant frequencies contained in the original data are then localized and the corresponding Discrete Fourier Transform (DFT) coefficients are estimated with low-complexity operations. Iterative subsampling-localization-estimation SFT algorithms are described in [154–157]. Other approaches estimate sparse DFT coefficients in a single pass after obtaining sufficient copies of subsampled signals [150–152, 158].

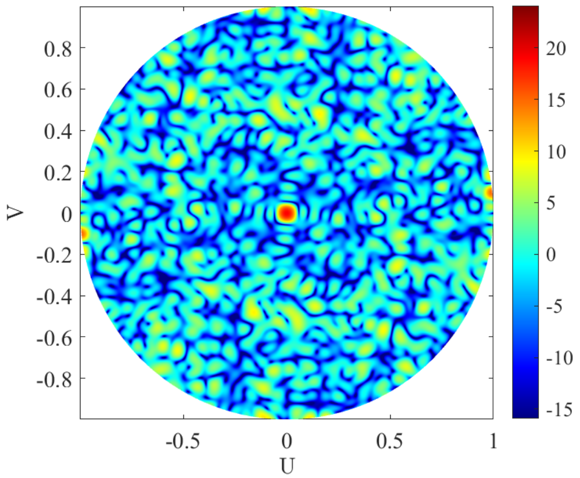

Fig. 24. Beampattern (dB) of randomized sparse array. Grating lobes have been reduced to at least 13 dB below the mainbeam peak.

F. Optimized SA Probes

With SA channel sounders, the receive antenna (also called a probe) mounted on a mechanical positioner can be optimized for wideband performance. For example, vector antennas are capable of measuring all six components of an impinging electromagnetic wave (i.e., $E_x, E_y, E_z, H_x, H_y, H_z$) in a Cartesian coordinate system. Recent results in [159] describe a dual-polarized vector antenna with 7:1 bandwidth (or 1-7 GHz). Due to its size, such an antenna would be difficult to embed into a hardware phased array, but it could serve as the receive probe for a SA. Quantum sensors that measure electric fields are also being investigated for use as probe antennas in SA systems, as described next.

Researchers at National Metrology Institutes [8, 160, 161], academic labs [162, 163], and in industry [164–171] are developing a new type of wideband receiver that detects the atomic response of room temperature vapor in the presence of a radio frequency (RF) electric field. These quantum receivers use lasers to excite alkali atoms to a high principal quantum number, a Rydberg state, where the valence electron is weakly bound to the nucleus and, therefore, is highly sensitive to perturbations from an incident RF electric field, Fig. 25. The operating frequency of this quantum receiver is defined by the frequency of the lasers that excite the atoms. Due to the fine tunability of these lasers, the quantum receivers the lasers drive are widely tunable, detecting incident fields from kilohertz to terahertz without any changes to the hardware [8, 172, 173]. Meanwhile, the instantaneous bandwidth of these receivers is on the order of megahertz [174] due primarily to the state lifetime of the Rydberg atoms. The receivers can also be used in a mixer configuration [175] wherein sub-Hertz frequency distinguishability is possible [176].

Early investigations using these Rydberg atom-based quantum microwave receivers to resolve spatial variations of an incident electric field and to detect angles of arrival have been published in recent years. These probes have been shown to detect spatial variations in the strength $|E(x,y)|$ of a microwave field either within an atomic vapor cell [172] or in the near-field of a transmitter [177, 178]. Using the mixer method [175] to determine phase of an incident RF electric field, Robinson, et al. demonstrated an angle of arrival measurement wherein two spatial locations inside the vapor cell were probed to determine the phase angle of the incident plane-wave field [179]. This concept was then extended by scanning a single-point Rydberg atom receiver over a SA to determine the spatial distribution of phase in the plane of measurement and to extract a set

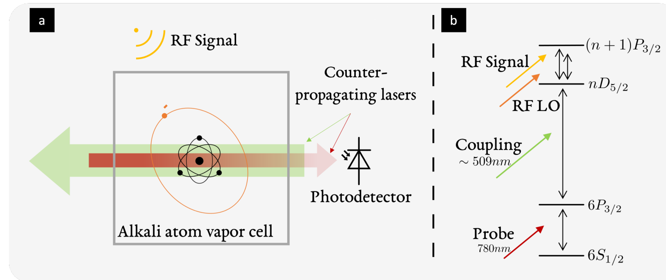

Fig. 25. (a) Depiction of a Rydberg atom sensor receiving over the air RF signals. (b) Basic ladder diagram showing the excited states (in cesium, e.g.) coupled by two counter-propagating lasers (probe and coupling) - reaching the first high n Rydberg state - and the RF signal coupling two Rydberg states. When an over the air RF local oscillator (LO) is on, the atoms act like a mixer where the signal output of the photodetector is the down-converted signal at the intermediate frequency between the RF signal and LO.

of angles of arrival [180]. The SA measurement was an early study in understanding the use of these receivers in such measurements, ultimately to be used in channel sounding. Other than the intrinsic wideband tunability of these receivers, a benefit of using the Rydberg atom quantum receivers is that field strength measurements with these devices are directly traceable to Planck's constant (h), Eq. 67 [181], a fundamental unit in the new SI [182], with a calculable scaling factor, the Rydberg transition dipole moment ($\wp_{ij}$) [181], where f_s is the splitting frequency of the narrow electromagnetically induced transparency (EIT) spectral line as the laser frequency is scanned, which can be measured very accurately, and ij denotes the two Rydberg states coupled by the RF field.

$$|E_{RF}| = \frac{f_s h}{\wp_{ij}} \tag{67}$$

When the atoms are used in the mixer method [175], the RF field imposed on the atoms is

$$\begin{aligned} E_{atoms} &= E_{res} E_{mod}, \\ E_{res} &= \cos(2\pi f_{LO} + \phi_{LO}) \\ E_{mod} &= \left(E_{LO}^2 + E_{SIG}^2 + 2E_{LO}E_{SIG}\cos(2\pi\Delta f t + \Delta\phi)\right)^{1/2}, \end{aligned} \tag{68}$$

with a component of the field that is resonant with the pair of Rydberg states E_{res} (see Fig. 25) and a component that causes a modulation of the EIT spectral line splitting (or a modulation of the transmitted power on the photodetector when the lasers are locked on resonance) at the intermediate frequency $\Delta f = f_{LO} - f_{SIG}$ between the over the air signal RF field and over the air LO, where $\Delta f \ll (f_{LO} + f_{SIG})/2$. The phase of this modulated voltage signal measured by the photodetector $\Delta\phi = \phi_{LO} - \phi_{SIG}$ contains information about the phase of the signal RF field, and, as long as the LO provides a constant phase reference, allows measurement of the signal field phase for angle of arrival and channel sounding applications described above. What is more, this receiver is fully dielectric and scatters much less radiation, potentially leading to more reliable wireless channel characterizations.

VII. SA's in Optics

Michelson and Pease published a seminal study on optical incoherent SA in 1921 which started the history of SA [183]. As a result, all of the interferometer systems in the radio and optical spectral regimes now provide high resolution images of astronomical objects through SA imaging [184, 185]. Essentially, these astronomical interferometers measure the statistical correlation between two electromagnetic signals originating in the object

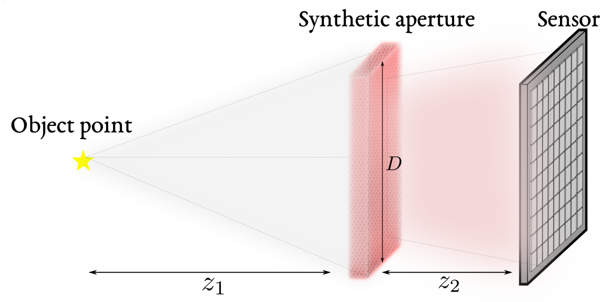

Fig. 26. Scheme of an SA optical system. The incoming light, either coherent or incoherent, from the object propagated to a distance z_1 is modulated by the SA. The resultant encoded light which passes through a different aperture is then recorded at a distance z_2 by an intensity sensor.

and passing through two telescopes spaced apart. Hence, all of these interferometers allow two signals to propagate simultaneously through two channels. Since the radio signals, including their amplitude and phase, are recorded in the radio antennas and transmitted electronically to the point of cross-correlation, this presents a less serious problem than in optics. In fact, only recording the amplitude of the signal leads to a problem called *phase retrieval*.

In the optical regime, however, an electrical detector cannot directly record the signal's phase without interfering with another telescope's wave. As a result, optical signals should be transferred by waveguides from the two telescopes far apart to the interference laboratory, with an optical path difference of about 100 micrometers between them, which is typical for optical sources. Thus, optical astronomical interferometers are heavy devices whose baseline (the distance between two telescopes) is limited to a few hundred meters. There is one exception to the two-wave interference problem: the intensity interferometer proposed by Hanbury Brown and Twiss [186], in which the intensity, rather than the complex amplitude, is cross-correlated between the two telescopes. Although intensity interferometers are capable of estimating target sizes in addition to imaging, these interferometers are no longer used because of relatively low SNRs.

In 2007, *F*resnel *in*coherent *c*orrelation *h*olography (FINCH) was introduced, opening up a number of new opportunities for incoherent SA imaging [187]. A typical setup is illustrated in Figure 26. A FINCH hologram is created using objects emitting incoherent light. As a result of the recording system splitting each object's light into two waves, it is possible to make holograms. In the camera, where these waves interact as holograms, both waves are modulated differently. Rather than record a hologram all at once, it was proposed to record it piecemeal over a period of time [188]. Nevertheless, this FINCH-based optical incoherent SA was not optimal in the sense that it resulted in relatively low image resolution. With FINCH [189] configured optimally, the various parts of the hologram were formed by interference between two waves from two far-apart subapertures. The problem of processing simultaneously through two far-apart channels still exists even when the SA imaging is implemented with a different physical effect than the traditional statistical correlation.

Three more systems in the history of optical incoherent SAs were introduced: *co*ded *a*perture *c*orrelation *h*olography (COACH) [190], interference-less COACH [191], followed by an imaging system for partial illumination [192]. COACH is a generalized version of FINCH as it is also a self-interference method for recording incoherent holograms, but instead of a quadratic phase mask in FINCH it uses a chaotic phase mask for one of the waves. In contrast, the interference-less COACH is a degenerate version of the self-interference COACH. Due to the necessity of recording a wave interference from two far-apart subapertures at the same time, a high-resolution image is achievable only if the system operates in the mode of two far-apart channels at the same time. In situations in which the same rule of simultaneously using two channels exists in three different systems that each rely on different physical effects, the rule may be considered as a generic law of nature that cannot be changed.

Researchers are also looking to quantum mechanics to find tools that may enable longer baselines between optical telescopes. One proposed method uses quantum repeater networks to create shared entangled states over arbitrarily long distances [193, 194]. Rather than needing to preserve the astronomical photons, entangled photons from a source between distant telescopes are transmitted over the long distance, with help from the quantum repeaters, and interferograms between the laboratory entangled photons and the astronomical photons are generated at each telescope. Those interferograms are subsequently compared to generate an image of the celestial object. Alternatively, quantum hard drives have been proposed to entirely avoid the need for optical fiber links between distant telescopes [195, 196]. The concept here is the quantum state of the astronomical photons is preserved in quantum memory on a physical quantum hard drive. That hard drive is then transported to a common location where all hard drives from each of the optical telescopes in the array are combined and interference between the preserved photon states is used to extract the high resolution image of the celestial object. At this point, quantum repeaters are limited in range due to their complexity and losses while the best reported storage lifetime of a quantum hard drive is on the order of 1 hour [196]. Further advancements in these spaces is needed before a practical quantum enhanced long baseline optical interferometer is implemented.

A. Phase retrieval algorithms

Phase information characterizes the delay accrued by an electromagentic wave during propagation. This information is typically lost in the optical detection process, because light detectors measure intensity-only variations. The phase information is regained at the cost of greater experimental complexity, typically by requiring light interference with a known field, as in the process of holography.Mathematically, the phaseless measurements $\{y_i\}_{i=1}^m$ acquired in this problem are

$$y_i = |\langle \boldsymbol{a}_i, \boldsymbol{x} \rangle|^2 + \eta_i, \tag{69}$$

where $\boldsymbol{x} \in \mathbb{C}^n$ is the target unkown signal, $\boldsymbol{a}_i \in \mathbb{C}^n$ are the known sampling vectors, and η_i models the noise.

Traditional algorithms to solve the phase retrieval problem are based on the error-reduction method [197] proposed in 1970. However, this method does not have solid theoretical convergence guarantees [197, 198]. Recently, a convex formulation was proposed in [199] via Phaselift, which consists in lifting up the original problem of vector recovery from a quadratic system into that of recovering a rank-1 matrix. In fact, this is possible because phaseless measurements in (69) are equivalent to

$$y_i = |\langle \boldsymbol{a}_i \boldsymbol{a}_i^H, \boldsymbol{X} \rangle|^2 + \eta_i, \tag{70}$$

where $\boldsymbol{X} = \boldsymbol{x}\boldsymbol{x}^H$. For this convex approach, large theoretical guarantees of convergence and recovery were provided, but its computational complexity becomes prohibitive when the signal dimension is large.

More recent methods described in [200] retrieve the phase by applying techniques such as matrix completion, and non-convex formulations [201, 202]. Specifically, one of the non-convex

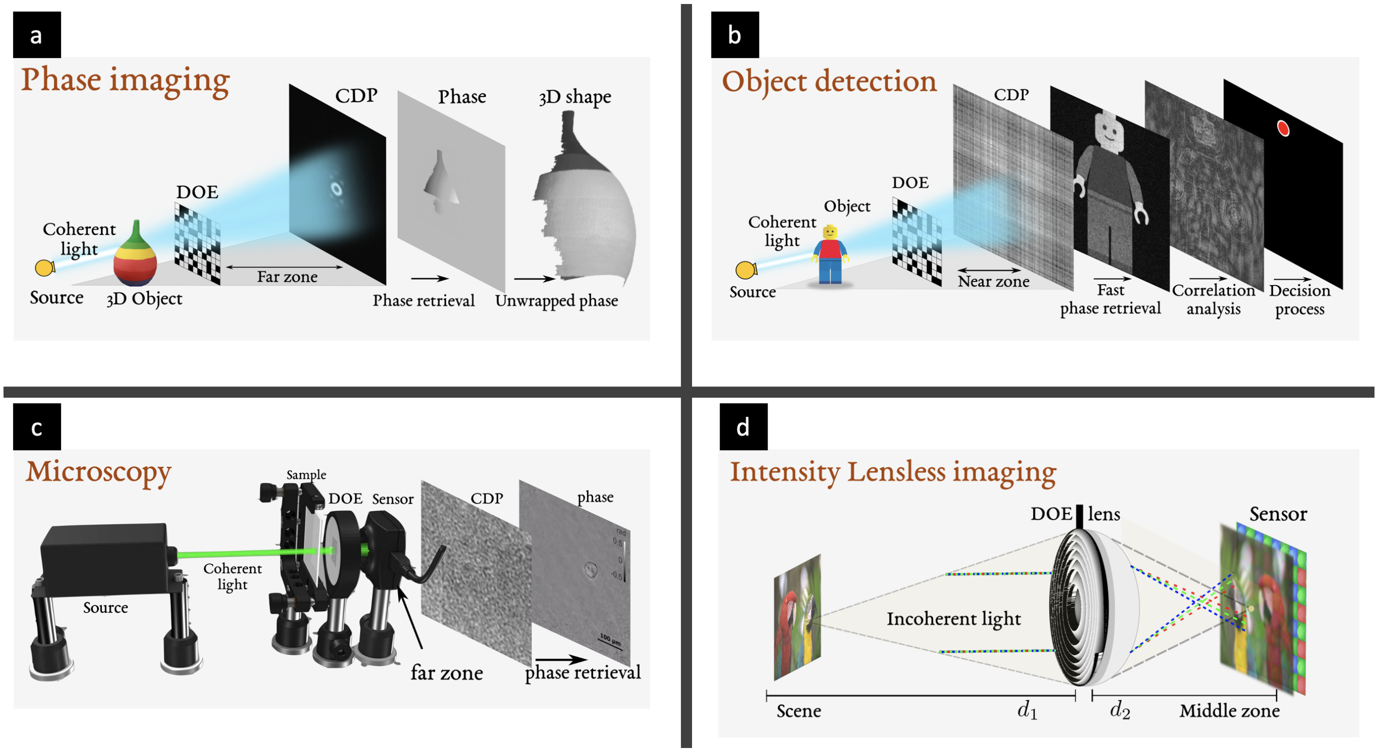

Fig. 27. Common coded-based optical imaging applications: (a) phase imaging, (b) object detection, (c) microscopy, and (d) lensless imaging [18].

formulations, called the Wirtinger Flow (WF), is a gradient descent method based on the Wirtinger derivative, and has demonstrated it can attain exact recovery from the phaseless measurements [200] up to a global unimodular constant. The WF method was improved by the truncated Wirtinger flow (TWF) algorithm proposed in [203], which optimizes the Poisson likelihood and keeps the convergence by designing truncation thresholds to calculate the step gradient. Additionally, the WF and the TWF methods use the spectral initialization strategy to guarantee exact recovery of the true signal up to a global unimodular constant.

The reweighted gradient flow (RAF) [204], stochastic truncated amplitude flow (STAF) [205], and the reshaped Wirtinger flow (RWF) [206] algorithms are also gradient descent methods based on the Wirtinger derivative. These methods aim to solve

$$\underset{\boldsymbol{x}\in\mathbb{C}^n}{\text{minimize}} \quad \frac{1}{m}\sum_{i=1}^{m}\left(\sqrt{y_i} - |\langle \boldsymbol{a}_i, \boldsymbol{x}\rangle|\right)^2 . \tag{71}$$

Further, the RAF and RWF algorithms introduce different initializations, which attain a more accurate estimation of the true signal in comparison to the spectral initialization. In terms of the sample complexity and speed of convergence, the RAF and RWF methods exhibit a superior performance over the state-of-the-art algorithms. It is important to highlight that the functions optimized by the RAF and RWF methods are non-convex and non-smooth. In particular, in order to address the non-smoothness of the optimization cost function, TWF introduces truncation procedures to eliminate the erroneously estimated signs with high probability.

B. Fourier Ptychography

The trade-off between resolution and imaging FoV is a long-standing problem in traditional optics. This trade-off implies an optical system can produce either an image of a small area with fine details, or an image of a large area with coarse details [207]. Fourier Ptychography (FP) was invented in 2013 [208] and has proven to be an effective method of mitigating this trade-off. FP alleviates the physical constraints that limit resolution by integrating SA imaging and phase retrieval. First, FP synthesizes the pupil aperture at the Fourier plane to bypass the resolution set by the objective lens. Mathematically, the acquired measurements in FP are given by

$$y_i = |\langle \boldsymbol{L}\boldsymbol{f}_i, \boldsymbol{x}\rangle|^2 + \eta_i, \tag{72}$$

where $\boldsymbol{L} \in \mathbb{C}^{n\times n}$ is a diagonal matrix that models the effect of the pupil aperture, and $\boldsymbol{f}_i \in \mathbb{C}^n$ for $i = 1,\dots,n$ are the rows of the inverse Fourier transform.

With FP, however, no phase is directly measured during the acquisition process as can be seen from (72), thereby eliminating the challenges of direct phase measurements that exist in holography. Instead, FP recovers the missing phase from intensity measurements during an iterative phase retrieval process. FP also provides the ability to computationally correct optical aberrations post-measurement and solves the problems of phase loss, aberration-induced artifacts, shallow depth of field (DOF), and allows for higher resolution and a larger FOV simultaneously [209]. Current applications include digital pathology and quantitative phase imaging (QPI) with high precision [210], high-throughput imaging [211], high-speed imaging [212], three dimensional (3D) imaging [213], and biomedical applications [214]. Combining reflective imaging, the authors in [215], [216] reported a proof-of-concept study for active remote sensing using visible light with FP.

In comparison to microwaves in SAR, visible light provides higher resolution. As well as providing additional phase information, FP also greatly increases the feasibility of remote sensing. Thereafter, a long-distance subdiffraction-limited visible imaging technique based on FP was developed in [217], i.e., SAVI, which allows the imaging distance to be set freely according to system parameters and is applicable to 0.7 to 1.5 m imaging distances. In contrast, the SAVI system's imaging range is limited by commercially available products, which is comparable to a finite correction system.

Moreover, due to the camera's scanning scheme, the FoV will change, resulting in a smaller overlapped FoV, leading to a higher cost for the array camera.

FP imaging with few photons is a challenge because stray light and noise can overwhelm the signal. Aidukas, et al., tackled this low SNR obstacle applicable to the imaging of delicate biological samples by leveraging quantum correlations. The team showed the ability to extract phase and intensity information of a microscopic object through correlations between the signal and idler of a parametric down-conversion illumination source in their experimental demonstration.

C. Coded Diffractive Imaging

Coded diffraction imaging refers to acquisition of images through a setup that employs coherent/incoherent light and a coded aperture (also known as a diffractive optical element (DOE)) to modulate the scene. Typically this setup allows the acquisition of several snapshots of the scene by changing the spatial configuration of the coded aperture. This modulated data is experimentally acquired in three diffraction zones: near, middle, and far [218, 219]. For the coherent case, mathematically, assuming a diagonal matrix $\boldsymbol{D}_\ell \in \mathbb{C}^{n\times n}$ for modeling the DOE for the ℓ-th snapshot, $\ell = 1,\dots,L$, the coded measurements consist of quadratic equations of the form

$$y_{i,\ell}^k = |\langle \boldsymbol{D}_\ell \boldsymbol{a}_i^k, \boldsymbol{x}\rangle|^2 + \eta_i^k, \tag{73}$$

where $\boldsymbol{a}_i^k \in \mathbb{C}^n$ are the known wavefront propagation vectors associated with the k-th diffraction for $i = 1,\cdots,n$, $\boldsymbol{x} \in \mathbb{C}^n$ is the unknown scene of interest, and $k = 1, 2, 3$ indexes the near, middle, and far zones, respectively.

By harnessing specific properties of each diffraction zone, several advances in imaging applications have been made, and Fig. 27 summarizes common coded aperture (or DOE) applications. Specifically, phase imaging deals with the reconstruction of the three-dimensional (3-D) shape of an object via phase retrieval. The far zone scenario consists of estimating the optical phase of the object by low-pass-filtering the leading eigenvector of a carefully constructed matrix [220]. In the case of object detection the optical phase is used to detect objects within a scene. Near zone coded data for rapid detection uses cross-correlation analysis to detect the target using its optical phase as a discriminant [221]. Moreover, the imaging task in microscopy is the reconstruction of the object wavefront. In [222], a novel approach is described for lens-less single-shot phase retrieval for pixel super-resolution phase imaging in the middle zone by suppressing the noise in a combination of sparse- and deep learning-based filters. Single-shot allows recording of dynamic scenes (frame rate limited only by the camera). And lastly, computational imaging with DOEs is a multidisciplinary research field at the intersection of optics, mathematics, and digital image processing [223]. Particularly, in [223] a DOE is effectively designed for all-in-focus intensity imaging where the diffraction patterns associated with the DOE were studied in the middle zone.

D. Coded Imaging Setups

The advantage of the coded aperture (DOE) lies in its imaging capability to successfully recover the phase without additional optical elements (such as lenses) leading to even more compact imaging devices [222]. The eschewing of the lens makes the system not only light and cost-effective but also lens-aberration-free and with a larger FoV.

Hyperspectral complex-domain imaging is a comparatively new development that deals with a phase delay of coherent light in transparent or reflective objects [224]. Hyperspectral broadband phase imaging is more informative than the monochromatic technique. Conventionally, for the processing of hyperspectral images, 2-D spectral narrow-band images are stacked together and represented as 3-D cubes with two spatial coordinates (x, y) and a third longitudinal spectral coordinate. In hyperspectral phase imaging, data in these 3-D cubes are complex-valued with spatially and spectrally varying amplitudes and phases. This makes phase image processing more complex than the hyperspectral intensity imaging, where the corresponding 3-D cubes are real-valued.

In certain coded diffractive imaging applications, the combination of blind deconvolution, super-resolution, and phase retrieval naturally manifests. While this is a severely ill-posed problem, it has been shown [225] that an image-of-interest could be estimated in polynomial-time. The approach relies on previous results that established the DOE design to achieve high quality images [226] and partially analyzed the combined problem by solving the super-resolution phase retrieval problem [227] from coded data. These designs are obtained by exploiting the model of the physical setup using machine learning methods where the DOE is modeled as a layer of a NN (data-driven model or unrolled) that is trained to act as an estimator of the true image [223]. This data-driven design has shown an outstanding image quality using a single snapshot as well as robustness against noise.

VIII. SA Sonar

SA processing with sonar poses certain challenges that have delayed the development and applicability of SAS imaging methods compared to its radar counterpart. The complexity of SA processing for underwater mapping applications stems mainly from: 1) the propagation speed of acoustic waves in water (1.5×10^3 m/s), which is at least 5 orders of magnitude smaller than the propagation speed of electromagnetic waves in air (3×10^8 m/s), and 2) the coherence loss of the received signal along the SA due to the random motion of the sonar platform, the instability of the medium and the multipath arrival pattern in shallow waters [228]. The low propagation speed of acoustic waves requires a long acquisition time to achieve a practically useful imaging range, limiting the ping repetition rate. Moreover, the spatial sampling requirement for unaliased imaging results in an inversely proportional relation between the speed of the platform carrying the sonar system and the maximum imaging range [229]. Therefore, the time required to form the SA for sonar is much longer than that for radar, making phase errors due to random platform motion and wave propagation critical for SAS imaging [230].

It was soon demonstrated that the temporal and spatial instability of the underwater environment, e.g., due to turbulence or spatial inhomogeneity of the acoustic parameters, is not the main limiting factor for practical SAS [230, 231]. Nevertheless, environmental factors can degrade SAS imaging, e.g., due to refractive effects from internal waves [232]. Introducing an array of multiple receivers instead of a single sensor provided a practically feasible pulse repetition rate for unaliased imaging and became the standard SAS configuration [233]. However, stable navigation of underwater vehicles and motion estimation and compensation with sub-wavelength accuracy is still a great operational challenge [234, 235]. Multi-channel systems increase the complexity of platform motion estimation introducing ping-to-ping yaw errors, but they offer a refined relative position estimate by cross-correlating the signals of overlapping elements in the displaced phase center antenna (DPCA) taking into account the spatio-temporal coherence of homogeneous reverberation [236–238]. State-of-the-art SAS systems are equipped with inertial navigation systems (INS) for coarse motion estimation, combined with DPCA micronavigation to compensate for residual

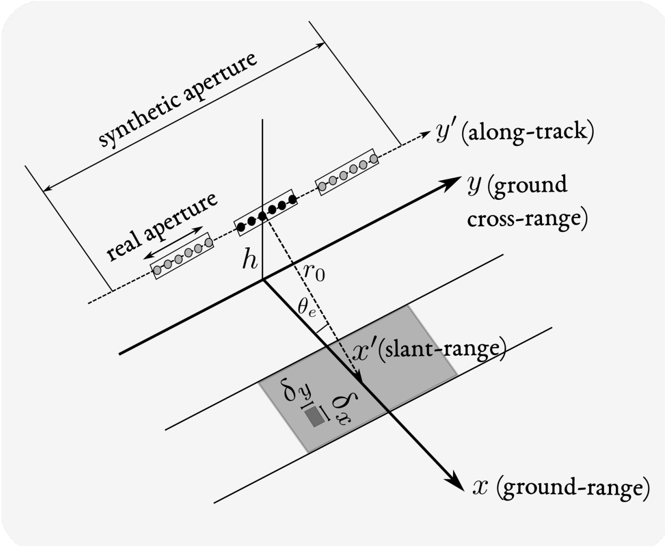

Fig. 28. SAS imaging geometry in strip-map mode.

navigation errors [239–241]. For many years, the cost and complexity of SAS systems limited their scope to military applications, such as mine countermeasures and unexploded ordnance remediation [2, 242]. It is only for the last 20 years that SAS has become common and inexpensive enough to be used for commercial applications such as underwater archaeology, inspection of underwater pipelines and seafloor mapping for offshore windfarm installation and monitoring [242, 243].

A comprehensive review of past work on SAS image reconstruction algorithms, platform motion estimation and compensation methods, interferometric SAS and SAS system configurations is presented in [2]. In the following, we summarize the basic SAS model before we highlight recent developments in SAS and current research trends categorized into generic research focus areas. We limit our review to methods that involve coherent signal processing, rather than incoherent image processing such as image segmentation and automatic target recognition [244, 245].

A. SAS model

The SAS geometry in the simplest and most applied strip-map modality is depicted in Fig. 28. A platform carrying an active sonar, with an arrangement of transmitters and receivers, moves along a linear path, parallel to the seafloor plane. In strip-map mode, the antenna is focused towards broadside, i.e., the central axis of the real-aperture beampattern is perpendicular to the platform path [246].

The active sonar transmits a short pulse, referred to as a ping, and records the backscattered echoes repeatedly as the platform moves along the track. The stop-and-hop approximation postulates that the platform is stationary during each ping transmission and reception, before it jumps instantaneously to the next position [246]. Hence, the position of the platform is discretized according to the ping number p as,

$$y_p = p v_p \tau_{rec}, \tag{74}$$

where v_p is the constant speed of the platform and τ_{rec} is the duration of the recording, which defines the ping repetition period. The insonified area per ping is determined by the radiation pattern of the transmitting antenna. The total imaging area is determined by the SA length and the recording duration τ_{rec} allowing a maximum swath width of,

$$r_{\max} = \frac{c\tau_{rec}}{2}, \tag{75}$$

where c is the speed of sound in water. Multi-element receiver arrays are employed to allow longer imaging ranges without violating the spatial sampling condition for a moderate platform speed (a few knots) [229].

Consider a pulsed acoustic source $h(\mathbf{r}_t, f) = b_T(\mathbf{r}_t)q(f)$, where $b_T(\mathbf{r}_t)$ describes the transmitter aperture as a function of the spatial coordinates $\mathbf{r}_t$ and $q(f)$ is the transmitted waveform as a function of frequency f. The sound pressure incident to a point located at $\mathbf{r}_s$ in the scattering medium due to the pulsed source centered at $\mathbf{r}_{t_c}$ is,

$$p_i(\mathbf{r}_{st}, f) = q(f)\int_{A_T} b_T(\mathbf{r}_{tt}) \frac{e^{-\mathrm{j}\frac{2\pi f}{c}\|\mathbf{r}_{st}-\mathbf{r}_{tt}\|_2}}{4\pi\|\mathbf{r}_{st}-\mathbf{r}_{tt}\|_2}\mathrm{d}\mathbf{r}_{tt}, \tag{76}$$

where the integration is over the transmitter aperture A_T and the position vectors are defined relative to the center of the aperture, i.e., $\mathbf{r}_{st} = \mathbf{r}_s - \mathbf{r}_{t_c}$ and $\mathbf{r}_{tt} = \mathbf{r}_t - \mathbf{r}_{t_c}$. Equation (76) is the solution to the inhomogeneous Helmholtz equation and describes the wavefield at the far-field of a spatially distributed harmonic source in an unbounded medium as the result of the integrated contributions of the elementary point sources $b_T(\mathbf{r}_{tt})\mathrm{d}\mathbf{r}_{tt}$ constituting the source aperture [247]. With the Fraunhofer approximation for far field propagation, [248] $\|\mathbf{r}_{st}-\mathbf{r}_{tt}\|_2 \approx \|\mathbf{r}_{st}\|_2 - \widehat{\mathbf{r}}_{st}\mathbf{r}_{tt}$, where $\widehat{\mathbf{r}}_{st} = \mathbf{r}_{st}/\|\mathbf{r}_{st}\|_2$ is the unit vector in the direction of $\mathbf{r}_{st}$, Eq. (76) is simplified to,

$$\begin{aligned} p_i(\mathbf{r}_{st}, f) &\approx q(f)\frac{e^{-\mathrm{j}\frac{2\pi f}{c}\|\mathbf{r}_{st}\|_2}}{4\pi\|\mathbf{r}_{st}\|_2}\int_{A_T} b_T(\mathbf{r}_{tt})e^{\mathrm{j}\frac{2\pi f}{c}\widehat{\mathbf{r}}_{st}\mathbf{r}_{tt}}\mathrm{d}\mathbf{r}_{tt} \\ &= q(f)\frac{e^{-\mathrm{j}\frac{2\pi f}{c}\|\mathbf{r}_{st}\|_2}}{4\pi\|\mathbf{r}_{st}\|_2}B_T(\mathbf{k}_{st}), \end{aligned} \tag{77}$$

where $\mathbf{k}_{st} = (2\pi f/c)\widehat{\mathbf{r}}_{st}$ is the wavenumber vector in the direction of $\widehat{\mathbf{r}}_{st}$ and $B_T(\mathbf{k}_{st})$ denotes the beampattern of the transmitter as the spatial Fourier transform of its aperture function.

Assuming that the platform is stationary during transmission and reception, the backscattered signal at a receiver centered at $\mathbf{r}_{r_c}$ from the point scatterer at $\mathbf{r}_s$ with complex scattering amplitude s is,

$$\begin{aligned} p(\mathbf{r}_{sr}, f) &= p_i(\mathbf{r}_{st}, f)s(\mathbf{r}_{sr}, f)\int_{A_R} b_R(\mathbf{r}_{rr}) \\ &\qquad\times \frac{e^{-\mathrm{j}\frac{2\pi f}{c}\|\mathbf{r}_{sr}-\mathbf{r}_{rr}\|_2}}{4\pi\|\mathbf{r}_{sr}-\mathbf{r}_{rr}\|_2}\mathrm{d}\mathbf{r}_{rr} \\ &\approx p_i(\mathbf{r}_{st}, f)s(\mathbf{r}_{sr}, f)\frac{e^{-\mathrm{j}\frac{2\pi f}{c}\|\mathbf{r}_{sr}\|_2}}{4\pi\|\mathbf{r}_{sr}\|_2}B_R(\mathbf{k}_{sr}), \end{aligned} \tag{78}$$

where the integration is over the receiver aperture A_R with beampattern $B_R(\mathbf{k}_{sr})$ and $\mathbf{r}_{sr} = \mathbf{r}_s - \mathbf{r}_{r_c}$, $\mathbf{r}_{rr} = \mathbf{r}_r - \mathbf{r}_{r_c}$.

In monostatic systems $\mathbf{r}_{t_c} = \mathbf{r}_{r_c} = \mathbf{r}_{\mathrm{v}}$ by definition, whereas in multi-static configurations the phase center approximation (PCA) [238] replaces each transmitter-receiver pair with a virtual element at $\mathbf{r}_{\mathrm{v}} = (\mathbf{r}_{t_c} + \mathbf{r}_{r_c})/2$ such that $\|\mathbf{r}_s - \mathbf{r}_{t_c}\|_2 \approx \|\mathbf{r}_s - \mathbf{r}_{r_c}\|_2 \approx \|\mathbf{r}_s - \mathbf{r}_{\mathrm{v}}\|_2 = \|\mathbf{r}_{s\mathrm{v}}\|_2$. At any given time frame, the total backscattered field at $\mathbf{r}_{\mathrm{v}}$ with the Born approximation [247] is the superposition of the backscattered echoes from all scatterers within the corresponding isochronous insonified volume A_s,

$$p(\mathbf{r}_{\mathrm{v}}, f) = \frac{q(f)}{(4\pi)^2}\int_{A_s} s(\mathbf{r}_{s\mathrm{v}}, f)B(\mathbf{k}_s)\frac{e^{-\mathrm{j}\frac{2\pi f}{c}2\|\mathbf{r}_{s\mathrm{v}}\|_2}}{\|\mathbf{r}_{s\mathrm{v}}\|_2^2}\mathrm{d}\mathbf{r}_s, \tag{79}$$

where $B(\mathbf{k}_s) = B_T(\mathbf{k}_{st})B_R(\mathbf{k}_{sr})$ is the combined beampattern of the transmitter and the receiver. In the case that the receiver is much smaller than the transmitter, the receiver's beampattern can be considered omnidirectional, hence $B(\mathbf{k}_s) \approx B_T(\mathbf{k}_{st})$.

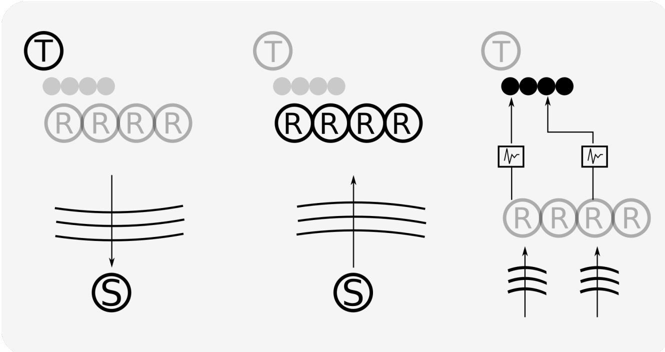

Fig. 29. Transmission (77), reception (78) and matched filtering (80) with a single-transmitter/multiple-receiver configuration. The PCA replaces the multistatic configuration with a virtual array of monostatic elements located at the middle of the distance between each transmitter-receiver pair.

The recorded backscattered signal (79) is compressed with matched filtering, i.e., by multiplication with the complex conjugate of the transmitted pulse $q^*(f)$,

$$\begin{aligned} p_{\text{mf}}(\mathbf{r}_{\text{v}}, f) &= q^*(f) p(\mathbf{r}_{\text{v}}, f) \\ &= \frac{\|q(f)\|_2^2}{(4\pi)^2} \int_{A_s} s(\mathbf{r}_{s\text{v}}, f) B(\mathbf{k}_s) \frac{e^{-\mathrm{j}\frac{2\pi f}{c} 2\|\mathbf{r}_{s\text{v}}\|_2}}{\|\mathbf{r}_{s\text{v}}\|_2^2} \mathrm{d}\mathbf{r}_s, \end{aligned} \tag{80}$$

Figure 29 shows a schematic of the transmission, reception and matched-filtering operations.

Discretizing the scattering field into an imaging grid of N points, the data model (80) can be written in a matrix-vector formulation,

$$\mathbf{d}(p, f) = \mathbf{A}(p, f)\mathbf{s}(p, f) + \mathbf{n}(p, f), \tag{81}$$

where $\mathbf{d} \in \mathbb{C}^M$ is the vector of the matched filtered measurements at frequency f for all M receivers comprising the real aperture at ping p, $\mathbf{s} \in \mathbb{C}^N$ is the unknown vector of the complex scattering values over a grid of N points and $\mathbf{n} \in \mathbb{C}^M$ is the additive noise vector. The matrix $\mathbf{A} \in \mathbb{C}^{M\times N}$ maps the unknown scattering $\mathbf{s}$ to the observations $\mathbf{d}$ and has as columns the steering vectors,

$$\mathbf{a}(\mathbf{r}_s, p, f) = [e^{-\mathrm{j}\frac{2\pi f}{c} 2\|\mathbf{r}_{sv_1}\|_2}, \cdots, e^{-\mathrm{j}\frac{2\pi f}{c} 2\|\mathbf{r}_{sv_M}\|_2}]^T, \tag{82}$$

which describe the propagation delay from the sth scatterer to all the M sensors on the real aperture at ping p. Note that we have incorporated the gain factor, $\|q(f)\|_2^2 B(\mathbf{k}_s)/(4\pi\|\mathbf{r}_{s\text{v}}\|_2)^2$, into the scattering vector $\mathbf{s}$ as it can be easily accounted for in a calibrated system.

SAS imaging refers to the inverse problem of reconstructing the scattering field $\mathbf{s}$, given the sensing matrix $\mathbf{A}$ and a set of measurements $\mathbf{d}$ over a range of frequencies and pings. Conventional (delay-and-sum) beamforming uses the steering vectors (82) as spatial weights to combine the sensor outputs coherently, compensating for the geometrically induced spatial Doppler modulation. In SAS imaging, conventional beamforming provides the scattering estimate,

$$\widehat{\mathbf{s}}_{\text{CBF}} = \sum_{i=1}^{P} \sum_{j=1}^{F} \mathbf{A}^H(p_i, f_j)\mathbf{d}(p_i, f_j), \tag{83}$$

by combining coherently the sensor outputs over P pings and F frequencies. In the case that there are only a few strong scatterers in the scattering field ($K \ll N$), SAS imaging can be solved as a sparse model fitting problem,

$$\min_{\mathbf{s}(p_i, f_j)} \frac{1}{2}\|\mathbf{A}(p_i, f_j)\mathbf{s}(p_i, f_j) - \mathbf{d}(p_i, f_j)\|_2^2 + \mu\|\mathbf{s}(p_i, f_j)\|_1. \tag{84}$$

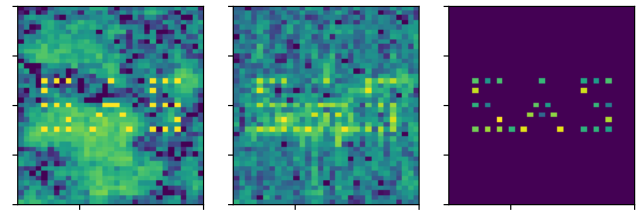

Fig. 30. Seafloor map with a configuration of strong scatterers in a weakly scattering background, and reconstruction with conventional and sparse SAS processing.

where $\mu > 0$ is a regularization parameter which controls the relative importance between the quadratic data-fitting term and the sparsity promoting ℓ_1-norm regularization term [249]. Figure 30 demonstrates SAS images of the reconstructed scattering field with conventional and sparse beamforming. The reader is referred to [246] for a comprehensive review of SAS imaging algorithms.

The resolution of a SAS system is defined in the range and cross-range directions, indicated in Fig. 28 as δ_x and δ_y respectively. The range resolution, obtained with matched filtering, is determined by the bandwidth Δf of the transmitted ping,

$$\delta_x \approx \frac{c}{2\Delta f}. \tag{85}$$

The cross-range (angular) resolution depends on the apparent SA length L_{SA},

$$\delta_y \approx \frac{\lambda r_0}{2L_{\text{SA}}}. \tag{86}$$

For a given transducer size D_y, the corresponding SA length is proportional to the wavelength and the range of a point scatterer, $L_{\text{SA}} \approx \lambda r_0/D$, resulting in a cross-range resolution which is independent of frequency and range, $\delta_y \approx D/2$ [229].

B. Wideband signal processing for SAS

There is a progressive shift of interest towards *wideband* and *widebeam SAS* systems that can provide information about the frequency- and aspect-dependent properties of sea-bottom scattering. For example, low frequencies can be partly transmitted through objects or penetrate the seafloor providing information about internal structure and buried objects [250–252], while multiple views provide information about the object's shape and dimensions [253]. As a result, several wideband SAS systems have been developed [241, 254–256] and SAS processing algorithms have been adapted for wideband and widebeam applications [249, 257–259].

Specifically, sub-band or sub-view processing for frequency- and aspect-dependent feature extraction reduces the resolution and the SNR compared to conventional SAS methods. To alleviate the corresponding SAS image degradation, signal processing methods such as spatial filtering followed by deconvolution [257] or wavenumber-domain filtering [259] have been proposed. Sparse signal reconstruction methods, such as feature selection through wavelet shrinkage [258] or distributed optimization [249], show great potential in wideband low-frequency SAS imaging. In interferometric SAS, wideband methods allow direct estimation of the absolute phase difference, providing robust three-dimensional imaging even with complicated scenes [260].

C. Micronavigation

Micronavigation refers to platform motion estimation methods, which use redundant recordings between pings in multi-channel systems to refine the coarse motion estimates from navigational instruments and achieve the subwavelength motion estimation accuracy required for SAS processing. Current work focuses on achieving sub-sample localization accuracy of the peak correlation from spatially and temporally sampled correlation measurements.

Methods that exploit the spatial correlation of overlapping measurements between consecutive pings for *along-track micronavigation* propose maximum likelihood estimators [261], analytical and numerical coherence models [262] and smoothing interpolation kernels [263, 264] to improve the accuracy of the along-track, ping-to-ping translation estimate. Similarly, time delay estimation between signals recorded on overlapping along-track positions between pings provides an *across-track micronavigation* estimate. Across-track micronavigation is particularly challenging in repeat-pass SAS processing for coherent change detection, where aggregated navigation errors between passes can result in baseline decorrelation not attributed to scene changes [265–267]. To achieve data co-registration in repeat-pass SAS, the authors in [265] introduce a repeat-pass SAS micronavigation algorithm that is a generalization of DPCA method, whereas Ref. [268] proposes a phase unwrapping approach to best fit the temporal correlation function in the presence of noise. The authors in Ref. [267] show that, by combining elements in the multi-channel system into larger effective elements, the along-track and across-track decorrelation baseline increases. A machine learning approach based on variational inference has been recently proposed for robust data-driven estimation of the three-dimensional platform translation between pings from spatiotemporal coherence measurements of diffuse backscatter [269].

D. System configuration

With regard to system design, recent developments propose MIMO configurations [270–272] and circular synthetic trajectories [273]. Specifically, *MIMO SAS* systems use multiple channels not only on receive, but also on transmit [270]. For example, Ref. [271] examines the use of spatially distributed transmitters in the across-track direction of a planar receiver array to increase the effective non-synthetic length of the array in that dimension and, consequently, improve the depth resolution of the resulting SAS system. Ref. [272], instead, proposes a MIMO SAS configuration with spatially distributed transmitters in the along-track direction to improve the spatial sampling rate and increase the imaging range. The authors employ a sparse reconstruction algorithm to reduce the impact of the residual waveform correlation and produce high-quality SAS imaging. *Circular SAS (CSAS)* improves the resolution and reduces the speckle in SAS imaging. Ref. [273] addresses the challenge of focusing CSAS data due to the non-linear trajectory.

IX. Intelligent SA Systems

With the arrival of computing systems with sufficient memory and clock rates, machine learning has grown massively in recent years as researchers have tried to apply it to myriad applications, including SAs. One of the first forays into the concept of intelligent control of sensing systems was Haykin's seminal article on cognitive radar [274], which defined the general architecture to support agile control of radar systems. Such systems, as posited by Haykin, share three defining features. First, they use intelligent signal processing, which builds on learning from the results of the radar's interactions with its environment. Second, they provide some type of channel for the receiver to provide feedback to the transmitter, which allows the transmitter to adapt to its environment in an intelligent way. Third, the system has a means for preserving the information content of

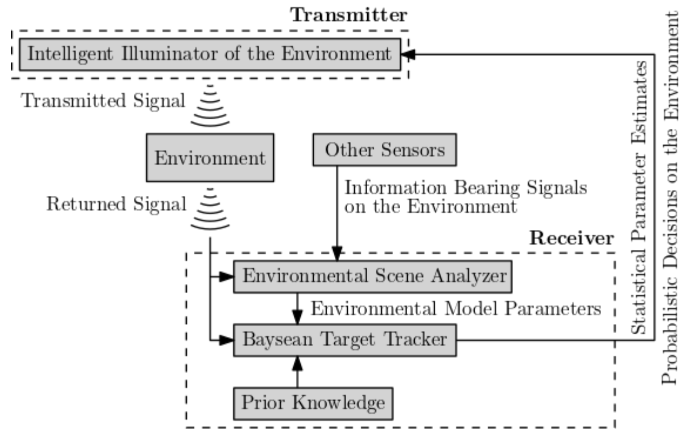

Fig. 31. The basic cognitive transmit/receive sensing system architecture proposed by Haykin, from Fig. 1 in [274]. This architecture assumes a feedback loop from receiver to transmitter, which may not exist (e.g., passive systems).

radar returns. From this general architecture, depicted in Fig. 31, it is possible to apply machine learning to multiple elements of the system. Wideband systems present a set of unique challenges relative to narrrowband systems, such as greater impact of frequency selective fading, as well as larger volumes of data, that invite the use of machine learning to efficiently develop system improvements.

Several current lines of machine learning work focus on SA front-end functions, such as beamforming. In addition, a vast literature has developed around SA image classification, but this considerable body of work lies outside the scope of this paper. As an example of research efforts in recent years that have explored using machine learning to do beamforming for SA, Luchies and Byram [275] proposed a deep feed-forward architecture for reducing sidelobes in ultrasound applications, and noted that SA techniques could provide further improvements by expanding the depth of field. Peretz and Feuer discuss a beamforming algorithm for SA ultrasound in [276]. The Delay and Sum (DAS) technique in SA ultrasound, allows for a higher frame rate but at the cost of lower Signal to Noise Ratio (SNR) and reduced contrast resolution. Using Synthetic Transmit Aperture (STA) ultrasound results in higher SNR, but requires more memory use because all the elements in the array are receiving and storing the returns from a single transmitting element. Peretz and Feuer introduce Deep NN Beamforming (DNNB) for SA, STA, and phased array, which involves a training component that compares large aperture and small aperture data, and a utilization component that uses the trained deep NN to process the small-aperture data to achieve large-aperture type results.

Yonei et al. [277] used deep NNs for image reconstruction in passive SA radar applications, where the user deploys receivers that operate opportunistically, i.e., they use transmitters in the environment, with which they do not coordinate operations, and measure the transmitter's signal and its reflection from a target of interest. The opportunistic nature of passive SAR means that the transmitter's location, waveform, and beam pattern may not be known to the receiver as it moves across the aperture. The authors trained a recurrent NN (RNN) model to obtain estimates of the parameters associated with both forward projection and backprojection and filtering. Using the Born approximation, the authors model the forward projection operation in a sampled aperture as the linear transformation $\boldsymbol{d} = \mathbf{F}\boldsymbol{\rho}$, where $\boldsymbol{\rho}$ is a vector of reflectivity values of sample points in the environment, $\boldsymbol{d}$ is the vector of corresponding received signal values, and $\mathbf{F}$ is the forward scattering matrix. They implement the backprojection and filtering operation using $\mathbf{F}$ and a filtering matrix $\mathbf{Q}$ that they employ at each stage of the RNN, and use unsupervised learning to train the RNNs to estimate the weights.

Yonel et al. built on their deep learning concept in a subsequent work [278], in which they apply a decoder to the estimated reflectivity vector at the RNN output to map it back to the data space and thus produce an auto-encoder. By incorporating feedback that adaptively minimizes the error between received SAR signals and those generated by the auto-encoder, the authors demonstrate that they are able to estimate the SAR waveform. In addition, other researchers have applied cognitive methods to SAR waveform design, such as the work by Xu et al. [279], which develops a joint optimization algorithm for designing a SAR waveform that maximizes resolution performance and the Signal to Clutter and Noise Ratio (SCNR).

Another major area of work involving machine learning is beamforming for ultrasound applications, including those that use either transmitted plane waves (PWs) or transmitted Diverging Waves (DWs). Early work includes the investigation by Gasse et al. [280], on PW beamforming using multiple transmissions to produce a compound image. Because PW transmissions do not use a focused beam, the image resolution for a single PW transmission is poor; a resulting strategy is to combine multiple PW images, but this oversampling reduces the ultrasound image frame rate. Gasse et al. developed a Convolutional NN (CNN) approach that would increase frame rate by learning channel parameters so that good quality images could be obtained by compounding fewer PW transmissions. The authors trained a six-layer CNN and were able to use it to match the performance metrics obtained with about 20 PW transmissions using only 3 PW transmissions.

More recent work by Ghani et al. in [281] addresses issues with using Diverging Waves (DWs) to illuminate targets. The authors also used a six-layer CNN with relatively low computational complexity by having only the first two CNN layers be 3D convolutional layers, with the subsequent layers being 2D. Ghani et al. also trained using invidual pixels rather than entire images, which prevents the CNN from learning features unique to ultrasound environments. The authors also used a compound loss function to train their CNN, rather than using a simple MMSE criterion. This produced improved performance due to the relationships between the various elements of the compound loss function.

Recent work has explored the use of machine learning to solve the forward and reverse scattering problems. This approach uses a linear approximation such as Eq. (81), which arises from sampling the scattering field. The approach employed by [282] uses a NN architecture that consists of a single layer of neurons, with no activation function, to find the sensing matrix, $\mathbf{A}$, or its pseudo-inverse $\mathbf{B} = (\mathbf{A}^H\mathbf{A})^{-1}\mathbf{A}^H$, where H is the Hermetian (complex transpose) matrix operator. The authors note that knowing $\mathbf{A}$ is sufficient to solve the scattering problem when the observation space sampling is chosen so that $\mathbf{A}^H\mathbf{A}$ is approximately a diagonal matrix; however, their experimental results using the CIFAR-10 image dataset [283] show better performance using the estimated pseudo-inverse.

X. SA Radiometry

Remote sensing at L-band (1.4 GHz) microwave frequencies provides the advantage of penetrating the atmosphere and offers sensitivity to parameters of the ocean and land surface that are important for understanding the earth's environment. Examples include the measurement of soil moisture and sea surface salinity which are important for understanding energy exchange with the atmosphere and, therefore, improve the forecasting of weather and climate change. The measurement of these parameters from space requires resolution on the order of 10 km. To obtain resolution on this order of magnitude requires placing very large antennas in orbit. For example, to obtain an image resolution of 10 km at 1.4 GHz would require an aperture of more than 15 m flying in a low earth orbit at an altitude of 800 km. The engineering problems associated with placing large antennas into orbit limit the deployment of passive sensors at this frequency [284].

Fig. 32. The microwave imaging radiometer using aperture synthesis (MIRAS) [284] is a Y-shaped SA radiometer on-board the soil moisture and ocean salinity (SMOS) satellite. Photo credit: European Space Agency.

Aperture synthesis is an interferometric technique for passive microwave remote sensing that mitigates the technical challenges associated with placing large apertures in space. In aperture synthesis, the coherent product (cross-correlation) of the complex signal from pairs of antennas is measured for different antenna-pair spacings (also called baselines). The product at each baseline yields a sample point in the Fourier transform of the brightness temperature map of the scene, and the scene itself can be reconstructed by inverting the sampled transform [285–290]. The resolution of the temperature image is determined by the largest baseline. The individual antennas determine the FOV on the ground surface. The compromise one makes in using aperture synthesis is a potential loss of radiometric sensitivity because small antennas imply a decrease in SNR for each measurement compared to a filled aperture.

Fig. 32 illustrates a concept for employing aperture synthesis in both spatial dimensions. In the picture, small antennas are arranged along the arms of a Y, but other arrangements are also possible. The necessary baselines are obtained by making measurements between all independent pairs of antennas. One can show that this configuration has the same spatial resolution as a filled aperture with the dimensions of the arms. Aircraft instruments with antennas arranged in Y and U configurations have been built and satellite instruments in space have used the Y configuration.

XI. Future Outlook and Summary

This paper has provided an overview of the broad utility of SA techniques to a wide range of imaging applications, including radar, channel sounding, optics, radiometry, and sonar. The overarching advantage of a SA is that the available angular resolution can be increased beyond the limits imposed by the physical size of the antenna. This is accomplished by using a mechanical positioner to move the receive antenna through space while it collects signal samples. Provided the samples are phase coherent then they can be combined in post-processing as if they were measured by a physical aperture with the same size as the SA. In the temporal domain, synthetic techniques can also be applied to increase the available delay resolution. For example, in frequency domain channel sounding, a wide measurement bandwidth is synthesized by measuring the frequency response of a wireless channel using many narrowband frequency tones spaced over a wide frequency grid.

Many recent innovations have improved the performance of SAs with potential for even more significant advances in the future. Primary among these is the use of self-calibrating quantum sensors based on Rydberg atoms that measure electric field strength to extraordinary precision. The quantum states of atoms are fundamental constants of nature that never drift or change and don't need to be calibrated. Therefore, they provide traceable measurements that are hugely important in many metrology applications.

New technology for micronavigation and the precision geolocation of ocean-going vessels has had a dramatic impact on SAS. By knowing precisely the location and orientation of a sonar vessel it is possible to significantly improve the detection and imaging performance of sonar, especially in severe weather. Advances in micronavigation have leveraged machine learning, which also underpins many other advances in SA imaging. New beamforming techniques and the development of intelligent systems that can adapt system parameters to optimize performance based on the operational environment are just a few examples of the advanced capabilities now possible via machine learning approaches.

Acknowledgements

K. V. M. acknowledges helpful discussions with Lam Nguyen of United States DEVCOM Army Research Laboratory. A. A.-G. thanks Matthew L. Simons of NIST for helpful discussions and reference paper recommendations. P. V. acknowledges measurements and data generated through experiments conducted by the SAMURAI team pertaining to the NIST Channel Sounding section. P. V. also acknowledges contributions to the simulations of randomized sparse arrays made by Mohamed Hany, Sudantha Perera, Katherine Remley, Carnot Nogueria, and Rick Candell of NIST.

References

[1] M. Soumekh, *Synthetic aperture radar signal processing*. John Wiley & Sons, 1999.

[2] M. P. Hayes and P. T. Gough, "Synthetic aperture sonar: A review of current status," *IEEE Journal of Oceanic Engineering*, vol. 34, no. 3, pp. 207–224, 2009.

[3] R. Levanda and A. Leshem, "Synthetic aperture radio telescopes," *IEEE Signal Processing Magazine*, vol. 27, no. 1, pp. 14–29, 2009.

[4] P. Vouras, J. Quimby, B. Jamroz, A. Weiss, R. Leonhardt, D. F. Williams, and K. A. Remley, "Frequency invariant beampatterns for wideband synthetic aperture channel sounders," in *IEEE International Workshop on Signal Processing Advances in Wireless Communications*, 2020, pp. 1–5.

[5] P. C. Konda, L. Loetgering, K. C. Zhou, S. Xu, A. R. Harvey, and R. Horstmeyer, "Fourier ptychography: Current applications and future promises," *Optics Express*, vol. 28, no. 7, pp. 9603–9630, 2020.

[6] D. M. Le Vine, "Synthetic aperture radiometer systems," *IEEE Transactions on Microwave Theory and Techniques*, vol. 47, no. 12, pp. 2228–2236, 1999.

[7] B. Fan and S. Das, "Synthetic aperture acoustic imaging with deep generative model based source distribution prior," in *IEEE International Conference on Acoustics, Speech and Signal Processing*, 2021, pp. 1420–1424.

[8] C. L. Holloway, J. A. Gordon, S. Jefferts, A. Schwarzkopf, D. A. Anderson, S. A. Miller, N. Thaicharoen, and G. Raithel, "Broadband Rydberg atom-based electric-field probe for SI-traceable, self-calibrated measurements," *IEEE Transactions on Antennas and Propagation*, vol. 62, no. 12, pp. 6169–6182, 2014.

[9] T. S. Ralston, D. L. Marks, P. Scott Carney, and S. A. Boppart, "Interferometric synthetic aperture microscopy," *Nature Physics*, vol. 3, no. 2, pp. 129–134, 2007.

[10] J. A. Jensen, S. I. Nikolov, K. L. Gammelmark, and M. H. Pedersen, "Synthetic aperture ultrasound imaging," *Ultrasonics*, vol. 44, pp. e5–e15, 2006.

[11] G. S. Mayer, H. Zhu, L. Lauzon, and R. Mitchell, "Synthetic aperture MRI," *Journal of Cerebral Blood Flow and Metabolism*, vol. 23, pp. 190–190, 2003.

[12] A. T. Herdman, A. Wollbrink, W. Chau, R. Ishii, B. Ross, and C. Pantev, "Determination of activation areas in the human auditory cortex by means of synthetic aperture magnetometry," *Neuroimage*, vol. 20, no. 2, pp. 995–1005, 2003.

[13] I. Akiyama and K. Yano, "Synthetic aperture computed tomography," in *Acoustical Imaging*, S. Lees and L. A. Ferrari, Eds. Springer, 1997, pp. 575–581.

[14] J. T. Ylitalo and H. Ermert, "Ultrasound synthetic aperture imaging: Monostatic approach," *IEEE Transactions on Ultrasonics, Ferroelectrics, and Frequency Control*, vol. 41, no. 3, pp. 333–339, 1994.

[15] K. V. Mishra, M. R. B. Shankar, V. Koivunen, B. Ottersten, and S. A. Vorobyov, "Toward millimeter-wave joint radar communications: A signal processing perspective," *IEEE Signal Processing Magazine*, vol. 36, no. 5, pp. 100–114, Sep 2019.

[16] A. M. Elbir, K. V. Mishra, and S. Chatzinotas, "Terahertz-band joint ultra-massive MIMO radar-communications: Model-based and model-free hybrid beamforming," *IEEE Journal of Special Topics in Signal Processing*, vol. 15, no. 6, pp. 1468–1483, 2021.

[17] S. Gishkori, D. Wright, L. Daniel, M. Gashinova, and B. Mulgrew, "Imaging moving targets for a forward-scanning automotive SAR," *IEEE Transactions on Aerospace and Electronic Systems*, vol. 56, no. 2, pp. 1106–1119, 2019.

[18] S. Pinilla, K. V. Mishra, I. Shevkunov, M. Soltanalian, V. Katkovnik, and K. Egiazarian, "Unfolding-aided bootstrapped phase retrieval in optical imaging: Explainable AI reveals new imaging frontiers," *IEEE Signal Processing Magazine*, vol. 40, pp. 46–60, 2023.

[19] D. A. Ausherman, A. Kozma, J. L. Walker, H. Jones, and E. C. Poggio, "Developments in radar imaging," *IEEE Transactions on Aerospace and Electronic Systems*, vol. AES-20, no. 4, pp. 363–400, 1984.

[20] J. R. Fienup and J. J. Miller, "Aberration correction by maximizing generalized sharpness metrics," *Journal of the Optical Society of America A*, vol. 20, no. 4, pp. 609–620, 2003.

[21] J. R. Fienup, "Detecting moving targets in SAR imagery by focusing," *IEEE Transactions on Aerospace and Electronic Systems*, vol. 37, no. 3, pp. 794–809, 2001.

[22] ——, "Gradient-search phase-retrieval algorithm for inverse synthetic-aperture radar," *Optical Engineering*, vol. 33, no. 10, pp. 3237–3242, 1994.

[23] ——, "Synthetic-aperture radar autofocus by maximizing sharpness," *Optics Letters*, vol. 25, no. 4, pp. 221–223, 2000.

[24] ——, "Phase error correction for synthetic aperture phased-array imaging systems," in *SPIE Image Reconstruction from Incomplete Data*, M. A. Fiddy and R. P. Millane, Eds., vol. 4123, 2000, pp. 47–55.

[25] W. Ye, T. S. Yeo, and Z. Bao, "Weighted least squares estimation of phase errors for SAR/ISAR autofocus," *IEEE Transactions on Geoscience and Remote Sensing*, vol. 37, no. 5, pp. 2487–2494, 1999.

[26] J. Ender, M. G. Amin, G. Fornaro, and P. A. Rosen, "Recent advances in radar imaging," *IEEE Signal Processing Magazine*, vol. 31, no. 4, pp. 15–158, 2014.

[27] S. A. Werness, M. A. Stuff, and J. R. Fienup, "Two-dimensional imaging of moving targets in SAR data," in *Asilomar Conference on Signals, Systems, and Computers*, 1990, pp. 16–22.

[28] O. Gassot, A. Herique, W. Fa, J. Du, and W. Kofman, "Ultra-wideband SAR tomography on asteroids," *Radio Science*, vol. 56, no. 8, pp. 1–17, 2021.

[29] M. Almutiry, "Wideband tomographic super-resolution radar image," *IEEE Sensors Journal*, vol. 20, no. 3, pp. 1208–1216, 2019.

[30] L. H. Nguyen, K. A. Kappra, D. C. Wong, R. Kapoor, and J. Sichina, "Mine field detection algorithm utilizing data from an ultrawideband wide-area surveillance radar," in *SPIE Detection and Remediation Technologies for Mines and Minelike Targets III*, vol. 3392, 1998, pp. 627–643.

[31] T. H. Vu, L. H. Nguyen, and V. Monga, "Classifying multichannel UWB SAR imagery via tensor sparsity learning techniques," *IEEE Transactions on Aerospace and Electronic Systems*, vol. 55, no. 4, pp. 1712–1724, 2018.

[32] F. Giovanneschi, K. V. Mishra, M. A. Gonzalez-Huici, Y. C. Eldar, and J. H. Ender, "Dictionary learning for adaptive GPR landmine classification," *IEEE Transactions on Geoscience and Remote Sensing*, vol. 57, no. 12, pp. 10 036–10 055, 2019.

[33] K. V. Mishra and L. H. Nguyen, "Autofocus algorithms for millimeter-wave 3-D FLoSAR," in *SPIE Passive and Active Millimeter-Wave Imaging XXII*, vol. 10994, 2019, p. 109940J.

[34] T. S. Lim, V. C. Koo, H.-T. Ewe, and H.-T. Chuah, "A SAR autofocus algorithm based on particle swarm optimization," *Progress In Electromagnetics Research B*, vol. 1, pp. 159–176, 2008.

[35] J. N. Ash, "An autofocus method for backprojection imagery in synthetic aperture radar," *IEEE Geoscience and Remote Sensing Letters*, vol. 9, no. 1, pp. 104–108, 2012.

[36] J. Wang and X. Liu, "SAR minimum-entropy autofocus using an adaptive-order polynomial model," *IEEE Geoscience and Remote Sensing Letters*, vol. 3, no. 4, pp. 512–516, 2006.

[37] D. Phippen, L. Daniel, E. Hoare Sr, S. Gishkori Sr, B. Mulgrew, M. Cherniakov, and M. Gashinova, "Height estimation for 3D automotive scene reconstruction using 300 GHz multi-receiver radar," *IEEE Transactions on Aerospace and Electronic Systems*, 2021, in press.

[38] V. C. Koo, T. S. Lim, and H. T. Chuah, "A comparison of autofocus algorithms for SAR imagery," in *Progress In Electromagnetics Research Symposium*, 2005, pp. 16–19.

[39] X. Mao, D. Zhu, and Z. Zhu, "Autofocus correction of APE and residual RCM in spotlight SAR polar format imagery," *IEEE Transactions on Aerospace and Electronic Systems*, vol. 49, no. 4, pp. 2693–2706, 2013.

[40] D. E. Wahl, P. H. Eichel, D. C. Ghiglia, and C. V. Jakowatz Jr., "Phase gradient autofocus - A robust tool for high resolution SAR phase correction," *IEEE Transactions on Aerospace and Electronic Systems*, vol. 30, no. 3, pp. 827–835, 1994.

[41] M. Kuźniak and M. Malanowski, "Implementation of phase gradient autofocus algorithm for spotlight SAR," in *SPIE Photonics Applications in Astronomy, Communications, Industry, and High-Energy Physics Experiments*, vol. 6937, 2007, p. 69372Y.

[42] Q. Liu and Y. Wang, "A fast eigenvector-based autofocus method for sparse aperture ISAR sensors imaging of moving target," *IEEE Sensors Journal*, vol. 19, no. 4, pp. 1307–1319, 2018.

[43] W. Jian and Z. Zhu-lin, "Forward looking SAR imaging algorithm via CS," in *IEEE CIE International Conference on Radar*, vol. 2, 2011, pp. 1562–1565.

[44] H. Mansour, D. Liu, U. S. Kamilov, and P. T. Boufounos, "Sparse blind deconvolution for distributed radar autofocus imaging," *IEEE Transactions on Computational Imaging*, vol. 4, no. 4, pp. 537–551, 2018.

[45] E. Mason, B. Yonel, and B. Yazici, "Deep learning for radar," in *IEEE Radar Conference*, 2017, pp. 1703–1708.

[46] D. Feng, D. An, and X. Huang, "An extended fast factorized back projection algorithm for missile-borne bistatic forward-looking SAR imaging," *IEEE Transactions on Aerospace and Electronic Systems*, vol. 54, no. 6, pp. 2724–2734, 2018.

[47] J. Wu, Z. Li, Y. Huang, J. Yang, H. Yang, and Q. H. Liu, "Focusing bistatic forward-looking SAR with stationary transmitter based on keystone transform and nonlinear chirp scaling," *IEEE Geoscience and Remote Sensing Letters*, vol. 11, no. 1, pp. 148–152, 2014.

[48] O. Rubel, V. Lukin, A. Rubel, and K. Egiazarian, "Selection of Lee filter window size based on despeckling efficiency prediction for Sentinel SAR images," *Remote Sensing*, vol. 13, no. 10, p. 1887, 2021.

[49] R. Guerra, S. López, and R. Sarmiento, "A computationally efficient algorithm for fusing multispectral and hyperspectral images," *IEEE Transactions on Geoscience and Remote Sensing*, vol. 54, no. 10, pp. 5712–5728, 2016.

[50] R. A. Schowengerdt, *Remote sensing: Models and methods for image processing*. Elsevier, 2006.

[51] N. Kussul, G. Lemoine, F. J. Gallego, S. V. Skakun, M. Lavreniuk, and A. Y. Shelestov, "Parcel-based crop classification in Ukraine using Landsat-8 data and Sentinel-1A data," *IEEE Journal of Selected Topics in Applied Earth Observations and Remote Sensing*, vol. 9, no. 6, pp. 2500–2508, 2016.

[52] E. Ferrentino, A. Buono, F. Nunziata, A. Marino, and M. Migliaccio, "On the use of multipolarization satellite SAR data for coastline extraction in harsh coastal environments: The case of Solway Firth," *IEEE Journal of Selected Topics in Applied Earth Observations and Remote Sensing*, vol. 14, pp. 249–257, 2020.

[53] N. Joshi, M. Baumann, A. Ehammer, R. Fensholt, K. Grogan, P. Hostert, M. R. Jepsen, T. Kuemmerle, P. Meyfroidt, E. T. Mitchard, J. Reiche, C. M. Ryan, and B. Waske, "A review of the application of optical and radar remote sensing data fusion to land use mapping and monitoring," *Remote Sensing*, vol. 8, no. 1, p. 70, 2016.

[54] A. D. Nascimento, A. C. Frery, and R. J. Cintra, "Detecting changes in fully polarimetric SAR imagery with statistical information theory," *IEEE Transactions on Geoscience and Remote Sensing*, vol. 57, no. 3, pp. 1380–1392, 2018.

[55] R. Touzi, "A review of speckle filtering in the context of estimation theory," *IEEE Transactions on Geoscience and Remote Sensing*, vol. 40, no. 11, pp. 2392–2404, 2002.

[56] C. Oliver and S. Quegan, *Understanding synthetic aperture radar images*. SciTech Publishing, 2004.

[57] V. S. Frost, J. A. Stiles, K. S. Shanmugan, and J. C. Holtzman, "A model for radar images and its application to adaptive digital filtering of multiplicative noise," *IEEE Transactions on Pattern Analysis and Machine Intelligence*, vol. PAMI-4, no. 2, pp. 157–166, 1982.

[58] D. Cozzolino, S. Parrilli, G. Scarpa, G. Poggi, and L. Verdoliva, "Fast adaptive nonlocal SAR despeckling," *IEEE Geoscience and Remote Sensing Letters*, vol. 11, no. 2, pp. 524–528, 2013.

[59] A. Gupta, A. Tripathi, and V. Bhateja, "Despeckling of SAR images via an improved anisotropic diffusion algorithm," in *International Conference on Frontiers of Intelligent Computing: Theory and Applications*, 2013, pp. 747–754.

[60] M. Tahmasbi, B. A. Bash, S. Guha, and M. Bloch, "Signaling for covert quantum sensing," in *IEEE International Symposium on Information Theory*, 2021, pp. 1041–1045.

[61] S. Lloyd, "Enhanced sensitivity of photodetection via quantum illumination," *Science*, vol. 321, no. 5895, pp. 1463–1465, 2008.

[62] M. Lanzagorta, O. Jitrik, J. Uhlmann, and S. E. Venegas-Andraca, "Quantum synthetic aperture radar," in *SPIE Radar Sensor Technology XXI*, K. I. Ranney and A. Doerry, Eds., vol. 10188, 2017, pp. 141–151.

[63] D. Luong, C. W. S. Chang, A. M. Vadiraj, A. Damini, C. M. Wilson, and B. Balaji, "Receiver operating characteristics for a prototype quantum two-mode squeezing radar," *IEEE Transactions on Aerospace and Electronic Systems*, vol. 56, no. 3, pp. 2041–2060, 2020.

[64] C. W. S. Chang, A. M. Vadiraj, J. Bourassa, B. Balaji, and C. M. Wilson, "Quantum-enhanced noise radar," *Applied Physics Letters*, vol. 114, no. 11, p. 112601, 2019.

[65] D. Luong, S. Rajan, and B. Balaji, "Entanglement-based quantum radar: From myth to reality," *IEEE Aerospace and Electronic Systems Magazine*, vol. 35, no. 4, pp. 22–35, 2020.

[66] S. Barzanjeh, S. Pirandola, D. Vitali, and J. M. Fink, "Microwave quantum illumination using a digital receiver," *Science Advances*, vol. 6, no. 19, p. eabb0451, 2020.

[67] S. Barzanjeh, S. Guha, C. Weedbrook, D. Vitali, J. H. Shapiro, and S. Pirandola, "Microwave quantum illumination," *Physical Review Letters*, vol. 114, p. 080503, 2015.

[68] M. Sanz, K. G. Fedorov, F. Deppe, and E. Solano, "Challenges in open-air microwave quantum communication and sensing," in *IEEE Conference on Antenna Measurements Applications*, 2018, pp. 1–4.

[69] M. Brandsema, "Current readiness for quantum radar implementation," in *IEEE Conference on Antenna Measurements Applications*, 2018, pp. 1–4.

[70] B. Balaji, "Quantum radar: Snake oil or good idea?" in *IEEE International Carnahan Conference on Security Technology*, 2018, pp. 1–7.

[71] A. Karsa and S. Pirandola, "Classical benchmarking for microwave quantum illumination," *IET Quantum Communication*, vol. 2, no. 4, pp. 246–257, 2021.

[72] ——, "Energetic considerations in quantum target ranging," in *IEEE Radar Conference*, 2021, pp. 1–4.

[73] M. I. Skolnik, *Radar handbook*, 3rd ed. McGraw Hill, 2008.

[74] W. M. Waters and B. R. Jarrett, "Tests of direct-sampling coherent detection with a laboratory analog-to-digital converter," *IEEE Transactions on Aerospace and Electronic Systems*, vol. AES-21, no. 3, pp. 430–432, 1985.

[75] ——, "Bandpass signal sampling and coherent detection," *IEEE Transactions on Aerospace and Electronic Systems*, vol. AES-18, no. 6, pp. 731–736, 1982.

[76] K. V. Mishra, "Frequency diversity wideband digital receiver and signal processor for solid-state dual-polarimetric weather radars," Master's thesis, Colorado State University, 2012.

[77] C. T. Rodenbeck, M. Martinez, J. B. Beun, J. Silva-Martinez, A. I. Karsilayan, and R. Liechty, "When less is more. . . Few bit ADCs in RF systems," *IEEE Access*, vol. 7, pp. 12 035–12 046, 2019.

[78] D. M. Akos and J. B. Y. Tsui, "Design and implementation of a direct digitization GPS receiver front end," *IEEE Transactions on Microwave Theory and Techniques*, vol. 44, no. 12, pp. 2334–2339, 1996.

[79] C. T. Rodenbeck, K. Tracey, K. Barkley, and B. DuVerneay, "Delta modulation technique for improving the sensitivity of monobit subsamplers in radar and coherent receiver applications," *IEEE Transactions on Microwave Theory and Techniques*, vol. 62, no. 8, pp. 1811–1822, 2014.

[80] C. T. Rodenbeck, A. C. Ferguson, and J. M. Pankonin, "Monobit subsampler for digital downconversion in pulse-Doppler radar applications," *IEEE Transactions on Microwave Theory and Techniques*, vol. 57, no. 5, pp. 1036–1043, 2009.

[81] G. Fornaro, V. Pascazio, and G. Schirinzi, "Synthetic aperture radar interferometry using one bit coded raw and reference signals," *IEEE Transactions on Geoscience and Remote Sensing*, vol. 35, no. 5, pp. 1245–1253, 1997.

[82] J. Li, M. Li, R. J. Evans, E. Skadas, and B. Moran, "Band-pass sampling techniques for high resolution multi-channel single-chip radar systems," in *IEEE Radar Conference*, 2012, pp. 499–503.

[83] J. Mo, A. Alkhateeb, S. Abu-Surra, and R. W. Heath, "Achievable rates of hybrid architectures with few-bit ADC receivers," in *International ITG Workshop on Smart Antennas*, 2016, pp. 1–8.

[84] A. V. Oppenheim and R. W. Schafer, *Discrete-time signal processing*, 3rd ed. Prentice Hall, 2009.

[85] J. B. Tsui, *Digital techniques for wideband receivers*. SciTech Publishing, 2004, vol. 2.

[86] ——, *Special design topics in digital wideband receivers*. Artech House, 2010.

[87] M. Shinagawa, Y. Akazawa, and T. Wakimoto, "Jitter analysis of high-speed sampling systems," *IEEE Journal of Solid-State Circuits*, vol. 25, no. 1, pp. 220–224, 1990.

[88] S. H. Dokhanchi, B. S. Mysore, K. V. Mishra, and B. Ottersten, "A mmWave automotive joint radar-communications system," *IEEE Transactions on Aerospace and Electronic Systems*, vol. 55, no. 3, pp. 1241–1260, 2019.

[89] S. Bhattacharjee, K. V. Mishra, R. Annavajjala, and C. R. Murthy, "Evaluation of orthogonal chirp division multiplexing for automotive integrated sensing and communications," in *IEEE International Conference on Acoustics, Speech and Signal Processing*, 2022, pp. 8742–8746.

[90] E. Vargas, K. V. Mishra, R. Jacome, B. M. Sadler, and H. Arguello, "Joint radar-communications processing from a dual-blind deconvolution perspective," in *IEEE International Conference on Acoustics, Speech and Signal Processing*, 2022, pp. 5622–5626.

[91] G. Duggal, S. Vishwakarma, K. V. Mishra, and S. S. Ram, "Doppler-resilient 802.11ad-based ultrashort range automotive joint radar-communications system," *IEEE Transactions on Aerospace and Electronic Systems*, vol. 56, no. 5, pp. 4035–4048, 2020.

[92] L. Wu, K. V. Mishra, M. R. Bhavani Shankar, and B. Ottersten, "Resource allocation in heterogeneously-distributed joint radar-communications under asynchronous Bayesian tracking framework," *IEEE Journal on Selected Areas in Communications*, vol. 40, no. 7, pp. 2026–2042, 2022.

[93] J. Liu, K. V. Mishra, and M. Saquib, "Co-designing statistical MIMO radar and in-band full-duplex multi-user MIMO communications," *arXiv preprint arXiv:2006.14774*, 2020.

[94] L. Li, K. Josiam, and R. Taori, "Feasibility study on full-duplex wireless millimeter-wave systems," in *IEEE International Conference on Acoustics, Speech and Signal Processing*, 2014, pp. 2769–2773.

[95] S. Rajagopal, R. Taori, and S. Abu-Surra, "Self-interference mitigation for in-band mmWave wireless backhaul," in *IEEE Consumer Communications and Networking Conference*, 2014, pp. 551–556.

[96] Z. Xiao, P. Xia, and X. G. Xia, "Full-duplex millimeter-wave communication," *IEEE Wireless Communications*, vol. 24, no. 6, pp. 136–143, 2017.

[97] V. Singh, S. Mondal, A. Gadre, M. Srivastava, J. Paramesh, and S. Kumar, "Millimeter-wave full duplex radios," in *ACM Annual International Conference on Mobile Computing and Networking*, 2020, pp. 1–4.

[98] K. Lin, Y. E. Wang, C. K. Pao, and Y. C. Shih, "A Ka-band FMCW radar front-end with adaptive leakage cancellation," *IEEE Transactions on Microwave Theory and Techniques*, vol. 54, no. 12, pp. 4041–4048, 2006.

[99] *IEEE 802.11ad Part 11: Wireless LAN medium access control (MAC) and physical layer (PHY) specifications Amendment 3: Enhancements for very high throughput in the 60 GHz band*, IEEE Std., 2012.

[100] E. Grossi, M. Lops, L. Venturino, and A. Zappone, "Opportunistic radar in IEEE 802.11ad networks," *IEEE Transactions on Signal Processing*, vol. 66, no. 9, pp. 2441–2454, 2018.

[101] P. Kumari, J. Choi, N. González-Prelcic, and R. W. Heath, "IEEE 802.11ad based radar: An approach to joint vehicular communication-radar system," *IEEE Transactions on Vehicular Technology*, vol. 67, no. 4, pp. 3012–3027, 2018.

[102] G. R. Muns, K. V. Mishra, C. B. Guerra, Y. C. Eldar, and K. R. Chowdhury, "Beam alignment and tracking for autonomous vehicular communication using IEEE 802.11ad-based radar," in *IEEE Infocom Workshops - Hot Topics in Social and Mobile Connected Smart Objects*, 2019, pp. 535–540.

[103] A. M. Elbir, K. V. Mishra, M. Shankar, and S. Chatzinotas, "The rise of intelligent reflecting surfaces in integrated sensing and communications paradigms," *IEEE Network*, 2023, in press.

[104] T. Wei, L. Wu, K. V. Mishra, and M. R. B. Shankar, "Multiple IRS-assisted wideband dual-function radar-communication," in *IEEE International Symposium on Joint Communications & Sensing*, 2022, pp. 1–5.

[105] Z. Esmaeilbeig, K. V. Mishra, and M. Soltanalian, "IRS-aided radar: Enhanced target parameter estimation via intelligent reflecting surfaces," in *IEEE Sensor Array and Multichannel Signal Processing Workshop*, 2022, pp. 1–5.

[106] S. D. Blunt and K. Gerlach, "Adaptive pulse compression via MMSE estimation," *IEEE Transactions on Aerospace and Electronic Systems*, vol. 42, no. 2, pp. 572–584, 2006.

[107] C. W. Rossler, "Adaptive radar with application to joint communication and synthetic aperture radar (CoSAR)," Ph.D. dissertation, Ohio State University, 2013.

[108] W. Gabriel, "Superresolution techniques and ISAR imaging," in *IEEE Radar Conference*, 1989, pp. 48–55.

[109] X. Liao and Z. Bao, "Radar target recognition using superresolution range profiles as features," in *SPIE International Symposium on Multispectral Image Processing*, vol. 3545, 1998, pp. 397–400.

[110] J. Tsao and B. D. Steinberg, "Reduction of sidelobe and speckle artifacts in microwave imaging: The CLEAN technique," *IEEE Transactions on Antennas and Propagation*, vol. 36, no. 4, pp. 543–556, 1988.

[111] R. Bose, A. Freedman, and B. D. Steinberg, "Sequence CLEAN: A modified deconvolution technique for microwave imaging of contiguous targets," *IEEE Transactions on Aerospace and Electronic Systems*, vol. 38, no. 1, pp. 89–97, 2002.

[112] A. Weiss, J. Quimby, R. Leonhardt, B. Jamroz, P. Vouras, K. Remley, and D. Williams, "Welcome to SAMURAI's documentation!" github, 2022, accessed: January 29, 2023. [Online]. Available: https://tsapps.nist.gov/publication/get_pdf.cfm?pub_id=933665,https://github.com/usnistgov/SAMURAI

[113] S. Ranvier, M. Kyro, K. Haneda, T. Mustonen, C. Icheln, and P. Vainikainen, "VNA-based wideband 60 GHz MIMO channel sounder with 3-D arrays," in *IEEE Radio and Wireless Symposium*, 2009, pp. 308–311.

[114] H. Nguyen, K. Mahler, M. Peter, W. Keusgen, T. Eichler, and H. Mellein, "Estimation of DoA based on large scale virtual array data," in *European Conference on Antennas and Propagation*, 2016, pp. 1–4.

[115] H. Nguyen, W. Keusgen, and T. Eichler, "Instantaneous direction of arrival measurements in mobile radio channels using virtual circular array antennas," in *IEEE Global Communications Conference Workshops*, 2016, pp. 1–7.

[116] H. Hayashi and T. Ohtsuki, "DOA estimation in MIMO radar using temporal spatial virtual array with MUSIC algorithm," in *IEEE International Conference on Signal Processing and Communication Systems*, 2015, pp. 1–6.

[117] A. Mannesson, B. Bernhardsson, M. Yaqoob, and T. F, "Optimal virtual array length under position imperfections," in *IEEE Sensor Array and Multichannel Signal Processing Workshop*, 2014, pp. 5–8.

[118] M. H. C. Dias and G. L. Siqueira, "Indoor 1.8 GHz AOA-TDOA measurements extending the use of a wideband propagation channel sounder with the synthetic aperture concept," in *European Microwave Conference*, 2005, pp. 1–4.

[119] H. Qiao, P. Sarangi, Y. Alnumay, and P. Pal, "Sample complexity trade-offs for synthetic aperture based high resolution estimation and detection," in *IEEE Sensor Array and Multichannel Signal Processing Workshop*, 2020, pp. 1–5.

[120] B. Chen, Z. Zhong, B. Ai, and D. G. Michelson, "Moving virtual array measurement scheme in high-speed railway," *IEEE Antennas and Wireless Propagation Letters*, vol. 15, pp. 706–709, 2016.

[121] T. Zhou, C. Tao, S. Salous, and L. Liu, "Measurements and analysis of angular characteristics and spatial correlation for high-speed railway channels," *IEEE Transactions on Intelligent Transportation Systems*, vol. 19, no. 2, pp. 357–67, 2018.

[122] G. Santella and E. Restuccia, "Analysis of frequency domain wide-band measurements of the indoor radio channel at 1, 5.5, 10 and 18 GHz," in *IEEE Global Communications Conference*, 1996, pp. 1162–1166.

[123] S. J. Howard and K. Pahlavan, "Measurement and analysis of the indoor radio channel in the frequency domain," *IEEE Transactions on Instrumentation and Measurement*, vol. 39, no. 5, pp. 751–755, 1990.

[124] A. W. Mbugua, W. Fan, Y. Ji, and G. F. Pedersen, "Millimeter wave multi-user performance evaluation based on measured channels with virtual antenna array channel sounder," *IEEE Access*, vol. 6, pp. 12 318–12 326, 2018.

[125] M. Kyro, S. Ranvier, V. M. Kolmonen, K. Haneda, and P. Vainikainen, "Long range wideband channel measurements at 81-86 GHz frequency range," in *European Conference on Antennas and Propagation*, 2010, pp. 1–5.

[126] A. J. Weiss, J. Quimby, R. Leonhardt, R. Jones, J. Kast, B. Jamroz, P. Vouras, D. F. Williams, and K. A. Remley, "Millimeter-wave high multipath channel measurements," in *URSI General Assembly and Scientific Symposium*, 2020, pp. 1–3.

[127] P. Vouras, K. A. Remley, B. Jamroz, M. Becker, D. F. Williams, J. Quimby, R. Leonhardt, R. D. Horansky, A. Weiss, R. D. Jones, J. Kast, A. Elsherbeni, P. Manurkar, D. Guven, J. Chuang, and C. Gentile, "Over-the-air testing with synthetic-aperture techniques," in *Metrology for 5G and Emerging Wireless Technologies*, T. H. Loh, Ed. IET Press, 2021, pp. 327–368.

[128] I. Frigyes and A. J. Seeds, "Optically generated true-time delay in phased-array antennas," *IEEE Transactions on Microwave Theory and Techniques*, vol. 43, no. 9, pp. 2378–2386, 1995.

[129] B. Wang, M. Jian, F. Gao, G. Y. Li, and H. Lin, "Beam squint and channel estimation for wideband mmWave massive MIMO-OFDM systems," *IEEE Transactions on Signal Processing*, vol. 67, no. 23, pp. 5893–5908, 2019.

[130] B. Wang, F. Gao, S. Jin, H. Lin, G. Y. Li, S. Sun, and T. S. Rappaport, "Spatial-wideband effect in massive MIMO with application in mmWave systems," *IEEE Communications Magazine*, vol. 56, no. 12, pp. 134–141, 2018.

[131] D. P. Scholnik and J. O. Coleman, "Formulating wideband array-pattern optimizations," in *IEEE International Conference on Phased Array Systems and Technology*, 2000, pp. 489–492.

[132] ——, "Optimal array-pattern synthesis for wideband digital transmit arrays," *IEEE Journal of Selected Topics in Signal Processing*, vol. 1, no. 4, pp. 660–677, 2007.

[133] W. Liu, D. McLernon, and M. Ghogho, "Frequency invariant beamforming without tapped delay-lines," in *IEEE International Conference on Acoustics, Speech and Signal Processing*, vol. 2, 2007, pp. II–997–II–1000.

[134] W. Liu, "Implementation of a wideband beamformer based on a rectangular array with spatial-only information," in *European Signal Processing Conference*, 2010, pp. 2087–2090.

[135] F. C. Lin, J. P. Hansen, J. McConnell, and K. Gerlach, "Experimental wideband multi-channel cancellation performance," in *IEEE Radar Conference*, 2005, pp. 675–679.

[136] S. C. Yeiss, R. W. Stewart, M. Schabert, I. K. Proudler, and M. W. Hoffman, "An efficient scheme for broadband adaptive beamforming," in *Asilomar Conference on Signals, Systems, and Computers*, vol. 1, 1999, pp. 496–500.

[137] P. Vouras, M. Hany, R. Candell, S. Perera, K. Remley, and C. Nogueira, "Grating lobes and spatial aliasing in sparse array beampatterns," National Institute of Standards and Technology, 2022, accessed: Jan. 15, 2022. [Online]. Available: https://doi.org/10.18434/mds2-2595

[138] S. Kirkpatrick, C. D. G. Jr., and M. P. Vecchi, "Optimization by simulated annealing," *Science*, vol. 220, no. 4598, pp. 671–680, 1983.

[139] V. Murino, A. Trucco, and C. S. Regazzoni, "Synthesis of unequally spaced arrays by simulated annealing," *IEEE Transactions on Signal Processing*, vol. 44, no. 1, pp. 119–122, 1996.

[140] J. F. Hopperstad, "Optimization of thinned arrays," Master's thesis, University of Oslo, 1998.

[141] A. Trucco and F. Repetto, "A stochastic approach to optimising the aperture and the number of elements of an aperiodic array," in *MTS/IEEE OCEANS Conference*, vol. 3, 1996, pp. 1510–1515.

[142] A. Trucco, "Synthesis of aperiodic planar arrays by a stochastic approach," in *MTS/IEEE OCEANS Conference*, vol. 2, 1997, pp. 820–825.

[143] J. H. Holland, "Genetic algorithms," *Scientific American*, vol. 267, no. 1, pp. 66–73, 1992.

[144] D. E. Goldberg, *Genetic algorithms*. Addison-Wesley, 1989.

[145] R. L. Haupt, "Thinned arrays using genetic algorithms," *IEEE Transactions on Antennas and Propagation*, vol. 42, no. 7, pp. 993–999, 1994.

[146] P. Weber, R. Schmitt, B. D. Tylkowski, and J. Steck, "Optimization of random sparse 2-D transducer arrays for 3-D electronic beam steering and focusing," in *IEEE Ultrasonics Symposium*, vol. 3, 1994, pp. 1503–1506.

[147] D. O'Neill, "Element placement in thinned arrays using genetic algorithms," in *MTS/IEEE OCEANS Conference*, vol. 2, 1994, pp. 301–306.

[148] H. Hassanieh, F. Adib, D. Katabi, and P. Indyk, "Faster GPS via the sparse Fourier transform," in *ACM Annual International Conference on Mobile Computing and Networking*, 2012, pp. 353–364.

[149] H. Hassanieh, L. Shi, O. Abari, E. Hamed, and D. Katabi, "GHz-wide sensing and decoding using the sparse Fourier transform," in *IEEE Conference on Computer Communications*, 2014, pp. 2256–2264.

[150] S. Wang, V. M. Patel, and A. Petropulu, "The robust sparse Fourier transform (RSFT) and its application in radar signal processing," *IEEE Transactions on Aerospace and Electronic Systems*, vol. 53, no. 6, pp. 2735–2755, 2017.

[151] L. Shi, H. Hassanieh, A. Davis, D. Katabi, and F. Duran, "Light field reconstruction using sparsity in the continuous Fourier domain," *ACM Transactions on Graphics*, vol. 34, no. 1, pp. 1–13, 2014.

[152] H. Hassanieh, M. Mayzel, L. Shi, D. Katabi, and V. Y. Orekhov, "Fast multi-dimensional NMR acquisition and processing using the sparse FFT," *Journal of Biomolecular NMR*, vol. 63, no. 1, pp. 9–19, 2015.

[153] S. Wang, V. M. Patel, and A. Petropulu, "Multidimensional sparse Fourier transform based on the Fourier projection-slice theorem," *IEEE Transactions on Signal Proccessing*, vol. 67, no. 1, pp. 54–69, 2019.

[154] A. C. Gilbert, M. J. Strauss, and J. A. Tropp, "A tutorial on fast Fourier sampling," *IEEE Signal Processing Magazine*, vol. 25, no. 2, pp. 57–66, 2008.

[155] A. C. Gilbert, P. Indyk, M. Iwen, and L. Schmidt, "Recent developments in the sparse Fourier transform: A compressed Fourier transform for big data," *IEEE Signal Processing Magazine*, vol. 31, no. 5, pp. 91–100, 2014.

[156] S. Pawar and K. Ramchandran, "FFAST: An algorithm for computing an exactly k-sparse DFT in $O(k \log k)$ time," *IEEE Transactions on Information Theory*, vol. 64, no. 1, pp. 429–450, 2018.

[157] B. Ghazi, H. Hassanieh, P. Indyk, D. Katabi, E. Price, and L. Shi, "Sample-optimal average-case sparse Fourier transform in two dimensions," in *IEEE Annual Allerton Conference on Communication, Control, and Computing*, 2013, pp. 1258–1265.

[158] H. Hassanieh, P. Indyk, D. Katabi, and E. Price, "Simple and practical algorithm for sparse Fourier transform," in *Annual ACM-SIAM symposium on Discrete Algorithms*, 2012, pp. 1183–1194.

[159] J. Duplouy, C. Morlaas, H. Aubert, P. Potier, and P. Pouliguen, "Wideband vector antenna for dual-polarized and three-dimensional direction-finding applications," *IEEE Antennas and Wireless Propagation Letters*, vol. 18, no. 8, pp. 1572–1575, 2019.

[160] V. Aksyuk, C. Holloway, A. Artusio-Glimpse, and M. Simons, "Photonic Rydberg atom radio frequency sensor array," U.S. Patent Application 63/228,238, 2021.

[161] C. L. Holloway, J. Kitching, A. Artusio-Glimpse, V. Aksyuk, M. T. Simons, and O. D. Lopez, "Atomic vapor cell and making an atomic vapor cell," U.S. Patent Application 17/374,537, 2021.

[162] J. A. Sedlacek, A. Schwettmann, H. Kübler, R. Löw, T. Pfau, and J. P. Shaffer, "Microwave electrometry with Rydberg atoms in a vapour cell using bright atomic resonances," *Nature Physics*, vol. 8, no. 11, pp. 819–824, 2012.

[163] C. S. Adams, J. D. Pritchard, and J. P. Shaffer, "Rydberg atom quantum technologies," *Journal of Physics B: Atomic, Molecular and Optical Physics*, vol. 53, no. 1, p. 012002, 2019.

[164] "Rydberg technologies: Quantum sensing and measurement solutions," http://www.rydbergtechnologies.com/, accessed: 2020-05-10.

[165] H. Amarloo, J. Ramirez-Serrano, and J. P. Shaffer, "Vapor cells for imaging of electromagnetic fields," U.S. Patent 11 112 298, 2020.

[166] ——, "Photonic-crystal vapor cells for imaging of electromagnetic fields," U.S. Patent Application 17/308,588, 2020.

[167] ——, "Radar systems using photonic crystal receivers to detect target objects," U.S. Patent Application 17/201,830, 2021.

[168] D. A. Anderson, R. E. Sapiro, and G. Raithel, "A self-calibrated SI-traceable Rydberg atom-based radio frequency electric field probe and measurement instrument," *IEEE Transactions on Antennas and Propagation*, vol. 69, no. 9, pp. 5931–5941, 2021.

[169] D. A. Anderson, G. A. Raithel, E. G. Paradis, and A. Rachel E. Sapiro, "Atom-based electromagnetic field sensing element and measurement system," U.S. Patent Application 2021/0 048 465 A1, 2021.

[170] K. Barokas, "ColdQuanta awarded DARPA contract to develop a complete Rydberg atom-based RF sensor system," https://www.globenewswire.com/news-release/2021/08/17/2282053/0/en/ColdQuanta-Awarded-DARPA-Contract-to-Develop-a-Complete-Rydberg-Atom-Based-RF-Sensor-System.html, accessed: 2022-05-10.

[171] "DARPA selects research teams to enable quantum shift in spectrum sensing," https://www.darpa.mil/news-events/2021-08-04, accessed: 2022-05-10.

[172] C. L. Holloway, M. T. Simons, J. A. Gordon, P. F. Wilson, C. M. Cooke, D. A. Anderson, and G. Raithel, "Atom-based RF electric field metrology: From self-calibrated measurements to subwavelength and near-field imaging," *IEEE Transactions on Electromagnetic Compatibility*, vol. 59, no. 2, pp. 717–728, 2017.

[173] D. H. Meyer, Z. A. Castillo, K. C. Cox, and P. D. Kunz, "Assessment of Rydberg atoms for wideband electric field sensing," *Journal of Physics B: Atomic, Molecular and Optical Physics*, vol. 53, no. 3, p. 034001, 2020.

[174] R. E. Sapiro, G. Raithel, and D. A. Anderson, "Time dependence of Rydberg EIT in pulsed optical and RF fields," *Journal of Physics B: Atomic, Molecular and Optical Physics*, vol. 53, no. 9, p. 094003, 2020.

[175] M. T. Simons, A. H. Haddab, J. A. Gordon, and C. L. Holloway, "A Rydberg atom-based mixer: Measuring the phase of a radio frequency wave," *Applied Physics Letters*, vol. 114, no. 11, p. 114101, 2019.

[176] J. A. Gordon, M. T. Simons, A. H. Haddab, and C. L. Holloway, "Weak electric-field detection with sub-1 Hz resolution at radio frequencies using a Rydberg atom-based mixer," *AIP Advances*, vol. 9, no. 4, p. 045030, 2019.

[177] M. T. Simons, J. A. Gordon, and C. L. Holloway, "Fiber-coupled vapor cell for a portable Rydberg atom-based radio frequency electric field sensor," *Applied Optics*, vol. 57, no. 22, pp. 6456–6460, 2018.

[178] R. Cardman, L. F. Gonçalves, R. E. Sapiro, G. Raithel, and D. A. Anderson, "Atomic 2D electric field imaging of a Yagi–Uda antenna near-field using a portable Rydberg-atom probe and measurement instrument," *Advanced Optical Technologies*, vol. 9, no. 5, pp. 305–312, 2020.

[179] A. K. Robinson, N. Prajapati, D. Senic, M. T. Simons, and C. L. Holloway, "Determining the angle-of-arrival of a radio-frequency source with a Rydberg atom-based sensor," *Applied Physics Letters*, vol. 118, no. 11, p. 114001, 2021.

[180] M. T. Simons, A. B. Artusio-Glimpse, A. K. Robinson, N. Prajapati, and C. L. Holloway, "Rydberg atom-based sensors for radio-frequency electric field metrology, sensing, and communications," *Measurement: Sensors*, vol. 18, p. 100273, 2021.

[181] C. L. Holloway, M. T. Simons, J. A. Gordon, A. Dienstfrey, D. A. Anderson, and G. Raithel, "Electric field metrology for SI traceability: Systematic measurement uncertainties in electromagnetically induced transparency in atomic vapor," *Journal of Applied Physics*, vol. 121, no. 23, p. 233106, 2017.

[182] D. B. Newell, F. Cabiati, J. Fischer, K. Fujii, S. G. Karshenboim, H. S. Margolis, E. de Mirandés, P. J. Mohr, F. Nez, K. Pachucki, T. J. Quinn, B. N. Taylor, M. Wang, B. M. Wood, and Z. Zhang, "The CODATA 2017 values of h, e, k, and n_A for the revision of the SI," *Metrologia*, vol. 55, no. 1, pp. L13–L16, 2018.

[183] A. A. Michelson and F. G. Pease, "Measurement of the diameter of Alpha-Orionis by the interferometer," *Proceedings of the National Academy of Sciences*, vol. 7, no. 5, p. 143, 1921.

[184] F. Merkle, "Synthetic-aperture imaging with the European very large telescope," *Journal of the Optical Society of America A*, vol. 5, no. 6, pp. 904–913, 1988.

[185] A. Bulbul and J. Rosen, "Super-resolution imaging by optical incoherent synthetic aperture with one channel at a time," *Photonics Research*, vol. 9, no. 7, pp. 1172–1181, 2021.

[186] R. H. Brown and R. Q. Twiss, "A test of a new type of stellar interferometer on Sirius," in *A Source Book in Astronomy and Astrophysics, 1900-1975*, K. R. Lang and O. Gingerich, Eds. Harvard University Press, 2013, pp. 8–12.

[187] J. Rosen and G. Brooker, "Digital spatially incoherent Fresnel holography," *Optics Letters*, vol. 32, no. 8, pp. 912–914, 2007.

[188] B. Katz and J. Rosen, "Super-resolution in incoherent optical imaging using synthetic aperture with Fresnel elements," *Optics Express*, vol. 18, no. 2, pp. 962–972, 2010.

[189] ——, "Could SAFE concept be applied for designing a new synthetic aperture telescope?" *Optics Express*, vol. 19, no. 6, pp. 4924–4936, 2011.

[190] A. Vijayakumar, Y. Kashter, R. Kelner, and J. Rosen, "Coded aperture correlation holography - A new type of incoherent digital holograms," *Optics Express*, vol. 24, no. 11, pp. 12 430–12 441, 2016.

[191] A. Vijayakumar and J. Rosen, "Interferenceless coded aperture correlation holography - A new technique for recording incoherent digital holograms without two-wave interference," *Optics Express*, vol. 25, no. 12, pp. 13 883–13 896, 2017.

[192] A. Bulbul, A. Vijayakumar, and J. Rosen, "Partial aperture imaging by systems with annular phase coded masks," *Optics Express*, vol. 25, no. 26, pp. 33 315–33 329, 2017.

[193] D. Gottesman, T. Jennewein, and S. Croke, "Longer-baseline telescopes using quantum repeaters," *Physical Review Letters*, vol. 109, p. 070503, 2012.

[194] J. Borregaard, H. Pichler, T. Schröder, M. D. Lukin, P. Lodahl, and A. S. Sørensen, "One-way quantum repeater based on near-deterministic photon-emitter interfaces," *Physical Review X*, vol. 10, p. 021071, 2020.

[195] J. Bland-Hawthorn, M. J. Sellars, and J. G. Bartholomew, "Quantum memories and the double-slit experiment: Implications for astronomical interferometry," *Journal of the Optical Society of America B*, vol. 38, no. 7, pp. A86–A98, 2021.

[196] Y. Ma, Y.-Z. Ma, Z.-Q. Zhou, C.-F. Li, and G.-C. Guo, "One-hour coherent optical storage in an atomic frequency comb memory," *Nature Communications*, vol. 12, no. 1, pp. 1–6, 2021.

[197] J. R. Fienup, "Phase retrieval algorithms: A comparison," *Applied Optics*, vol. 21, no. 15, pp. 2758–2769, 1982.

[198] E. J. Candès, X. Li, and M. Soltanolkotabi, "Phase retrieval from coded diffraction patterns," *Applied and Computational Harmonic Analysis*, vol. 39, no. 2, pp. 277–299, 2015.

[199] E. J. Candès and X. Li, "Solving quadratic equations via phaselift when there are about as many equations as unknowns," *Foundations of Computational Mathematics*, vol. 14, no. 5, pp. 1017–1026, 2014.

[200] E. J. Candès, X. Li, and M. Soltanolkotabi, "Phase retrieval via Wirtinger flow: Theory and algorithms," *IEEE Transactions on Information Theory*, vol. 61, no. 4, pp. 1985–2007, 2015.

[201] S. Pinilla, J. Bacca, and H. Arguello, "Phase retrieval algorithm via nonconvex minimization using a smoothing function," *IEEE Transactions on Signal Processing*, vol. 66, no. 17, pp. 4574–4584, 2018.

[202] A. Paulus, J. Knapp, J. Kornprobst, and T. F. Eibert, "Reliable linearized phase retrieval for near-field antenna measurements with truncated measurement surfaces," *IEEE Transactions on Antennas and Propagation*, 2022, in press.

[203] Y. Chen and E. Candès, "Solving random quadratic systems of equations is nearly as easy as solving linear systems," in *Advances in Neural Information Processing Systems*, 2015, pp. 739–747.

[204] G. Wang, G. B. Giannakis, Y. Saad, and J. Chen, "Phase retrieval via reweighted amplitude flow," *IEEE Transactions on Signal Processing*, vol. 66, no. 11, pp. 2818–2833, 2018.

[205] G. Wang, G. B. Giannakis, and J. Chen, "Scalable solvers of random quadratic equations via stochastic truncated amplitude flow," *IEEE Transactions on Signal Processing*, vol. 65, no. 8, pp. 1961–1974, 2017.

[206] H. Zhang and Y. Liang, "Reshaped Wirtinger flow for solving quadratic system of equations," in *Advances in Neural Information Processing Systems*, 2016, pp. 2622–2630.

[207] G. Zheng, C. Shen, S. Jiang, P. Song, and C. Yang, "Concept, implementations and applications of Fourier ptychography," *Nature Reviews Physics*, vol. 3, no. 3, pp. 207–223, 2021.

[208] G. Zheng, R. Horstmeyer, and C. Yang, "Wide-field, high-resolution Fourier ptychographic microscopy," *Nature Photonics*, vol. 7, no. 9, pp. 739–745, 2013.

[209] A. Pan, M. Zhou, Y. Zhang, J. Min, M. Lei, and B. Yao, "Adaptive-window angular spectrum algorithm for near-field ptychography," *Optics Communications*, vol. 430, pp. 73–82, 2019.

[210] Y. Zhang, A. Pan, M. Lei, and B. Yao, "Data preprocessing methods for robust Fourier ptychographic microscopy," *Optical Engineering*, vol. 56, no. 12, p. 123107, 2017.

[211] A. Pan, Y. Zhang, K. Wen, M. Zhou, J. Min, M. Lei, and B. Yao, "Subwavelength resolution Fourier ptychography with hemispherical digital condensers," *Optics Express*, vol. 26, no. 18, pp. 23 119–23 131, 2018.

[212] L. Tian, Z. Liu, L.-H. Yeh, M. Chen, J. Zhong, and L. Waller, "Computational illumination for high-speed in vitro Fourier ptychographic microscopy," *Optica*, vol. 2, no. 10, pp. 904–911, 2015.

[213] R. Horstmeyer, J. Chung, X. Ou, G. Zheng, and C. Yang, "Diffraction tomography with Fourier ptychography," *Optica*, vol. 3, no. 8, pp. 827–835, 2016.

[214] J. Chung, G. W. Martinez, K. C. Lencioni, S. R. Sadda, and C. Yang, "Computational aberration compensation by coded-aperture-based correction of aberration obtained from optical Fourier coding and blur estimation," *Optica*, vol. 6, no. 5, pp. 647–661, 2019.

[215] K. Guo, S. Dong, and G. Zheng, "Fourier ptychography for brightfield, phase, darkfield, reflective, multi-slice, and fluorescence imaging," *IEEE Journal of Selected Topics in Quantum Electronics*, vol. 22, no. 4, pp. 77–88, 2015.

[216] S. Dong, R. Horstmeyer, R. Shiradkar, K. Guo, X. Ou, Z. Bian, H. Xin, and G. Zheng, "Aperture-scanning Fourier ptychography for 3D refocusing and super-resolution macroscopic imaging," *Optics Express*, vol. 22, no. 11, pp. 13 586–13 599, 2014.

[217] J. Holloway, M. S. Asif, M. K. Sharma, N. Matsuda, R. Horstmeyer, O. Cossairt, and A. Veeraraghavan, "Toward long-distance subdiffraction imaging using coherent camera arrays," *IEEE Transactions on Computational Imaging*, vol. 2, no. 3, pp. 251–265, 2016.

[218] T.-C. Poon and J.-P. Liu, *Introduction to modern digital holography: With MATLAB*. Cambridge University Press, 2014.

[219] A. Guerrero, S. Pinilla, and H. Arguello, "Phase recovery guarantees from designed coded diffraction patterns in optical imaging," *IEEE Transactions on Image Processing*, vol. 29, pp. 5687–5697, 2020.

[220] S. Pinilla, L. Galvis, K. Egiazarian, and H. Arguello, "Single-shot coded diffraction system for 3D object shape estimation," in *International Symposium on Electronic Imaging*, vol. 6, 2020, p. 059.

[221] A. Jerez, S. Pinilla, and H. Arguello, "Fast target detection via template matching in compressive phase retrieval," *IEEE Transactions on Computational Imaging*, vol. 6, pp. 934–944, 2020.

[222] P. Kocsis, I. Shevkunov, V. Katkovnik, H. Rekola, and K. Egiazarian, "Single-shot pixel super-resolution phase imaging by wavefront separation approach," *Optics Express*, vol. 29, no. 26, pp. 43 662–43 678, 2021.

[223] S. R. M. Rostami, S. Pinilla, I. Shevkunov, V. Katkovnik, and K. Egiazarian, "Power-balanced hybrid optics boosted design for achromatic extended depth-of-field imaging via optimized mixed OTF," *Applied Optics*, vol. 60, no. 30, pp. 9365–9378, 2021.

[224] V. Katkovnik, I. Shevkunov, and K. Egiazarian, "ADMM and spectral proximity operators in hyperspectral broadband phase retrieval for quantitative phase imaging," *arXiv preprint arXiv:2105.07891*, 2021.

[225] S. Pinilla, K. V. Mishra, and B. M. Sadler, "Non-convex recovery from phaseless low-resolution blind deconvolution measurements using noisy masked patterns," in *Asilomar Conference on Signals, Systems, and Computers*, 2021, pp. 876–880.

[226] J. Bacca, S. Pinilla, and H. Arguello, "Super-resolution phase retrieval from designed coded diffraction patterns," *IEEE Transactions on Image Processing*, vol. 29, pp. 2598–2609, 2019.

[227] V. Katkovnik, I. Shevkunov, N. V. Petrov, and K. Egiazarian, "Computational super-resolution phase retrieval from multiple phase-coded diffraction patterns: Simulation study and experiments," *Optica*, vol. 4, no. 7, pp. 786–794, 2017.

[228] L. J. Cutrona, "Comparison of sonar system performance achievable using synthetic aperture techniques with the performance achievable by more conventional means," *The Journal of the Acoustical Society of America*, vol. 58, no. 2, pp. 336–348, 1975.

[229] R. E. Hansen, "Introduction to synthetic aperture sonar," in *Sonar Systems*, N. Kolev, Ed. InTechOpen, 2011, pp. 3–28.

[230] R. E. Williams, "Creating an acoustic synthetic aperture in the ocean," *The Journal of the Acoustical Society of America*, vol. 60, no. 1, pp. 60–73, 1976.

[231] J. T. Christoff, C. D. Loggins, and E. L. Pipkin, "Measurement of the temporal phase stability of the medium," *The Journal of the Acoustical Society of America*, vol. 71, no. 6, pp. 1606–1607, 1982.

[232] R. E. Hansen, A. P. Lyons, T. O. Sæbø, H. J. Callow, and D. A. Cook, "The effect of internal wave-related features on synthetic aperture sonar," *IEEE Journal of Oceanic Engineering*, vol. 40, no. 3, pp. 621–631, 2014.

[233] H. Lee, "Extension of synthetic aperture radar (SAR) technique to undersea applications," *IEEE Journal of Oceanic Engineering*, vol. 4, no. 2, pp. 60–63, 1979.

[234] R. E. Hansen, H. J. Callow, T. O. Sæbø, and S. Synnes, "Challenges in seafloor imaging and mapping with synthetic aperture sonar," *IEEE Transactions on Geoscience and Remote Sensing*, vol. 49, no. 10, pp. 3677–3687, 2011.

[235] A. J. Hunter, W. A. Connors, and S. Dugelay, "An operational concept for correcting navigation drift during sonar surveys of the seafloor," *IEEE Journal of Oceanic Engineering*, vol. 43, no. 4, pp. 913–926, 2017.

[236] Y. Doisy, "General motion estimation from correlation sonar," *IEEE Journal of Oceanic Engineering*, vol. 23, no. 2, pp. 127–140, 1998.

[237] ——, "Theoretical accuracy of Doppler navigation sonars and acoustic Doppler current profilers," *IEEE Journal of Oceanic Engineering*, vol. 29, no. 2, pp. 430–441, 2004.

[238] A. Bellettini and M. A. Pinto, "Theoretical accuracy of synthetic aperture sonar micronavigation using a displaced phase-center antenna," *IEEE J. Oceanic Eng.*, vol. 27, no. 4, pp. 780–789, 2002.

[239] T. G. Fossum, P. E. Hagen, B. Langli, and R. E. Hansen, "HISAS 1030: High resolution synthetic aperture sonar with bathymetric capabilities," in *International Conference on High-Resolution Surveys in Shallow Water*, 2008, p. 1.

[240] A. Bellettini and M. Pinto, "Design and experimental results of a 300-kHz synthetic aperture sonar optimized for shallow-water operations," *IEEE Journal of Oceanic Engineering*, vol. 34, no. 3, pp. 285–293, 2009.

[241] L. Jay Larsen, A. Wilby, and C. Stewart, "Deep ocean survey and search using synthetic aperture sonar," in *MTS/IEEE OCEANS Conference*, 2010, pp. 1–4.

[242] R. E. Hansen, "Synthetic aperture sonar technology review," *Marine Technology Society Journal*, vol. 47, no. 5, pp. 117–127, 2013.

[243] P. Hagen, N. Storkersen, and K. Vestgard, "HUGIN - use of UUV technology in marine applications," in *MTS/IEEE OCEANS Conference*, vol. 2, 1999, pp. 967–972.

[244] D. P. Williams, "Fast target detection in synthetic aperture sonar imagery: A new algorithm and large-scale performance analysis," *IEEE Journal of Oceanic Engineering*, vol. 40, no. 1, pp. 71–92, 2014.

[245] I. J. Sledge, M. S. Emigh, J. L. King, D. L. Woods, J. T. Cobb, and J. C. Principe, "Target detection and segmentation in circular-scan synthetic-aperture-sonar images using semi-supervised convolutional encoder-decoders," *arXiv preprint arXiv:2101.03603*, 2021.

[246] P. T. Gough and D. W. Hawkins, "Unified framework for modern synthetic aperture imaging algorithms," *International Journal of Imaging Systems and Technology*, vol. 8, no. 4, pp. 343–358, 1997.

[247] P. M. Morse and K. U. Ingaard, *Theoretical acoustics*. Princeton University Press, 1986.

[248] J. W. Goodman, *Introduction to Fourier optics*, 3rd ed. Roberts & Co., 2005.

[249] A. Xenaki and Y. Pailhas, "Compressive synthetic aperture sonar imaging with distributed optimization," *The Journal of the Acoustical Society of America*, vol. 146, no. 3, pp. 1839–1850, 2019.

[250] M. A. Pinto, A. Bellettini, R. Hollett, and A. Tesei, "Real-and synthetic-array signal processing of buried targets," *IEEE Journal of Oceanic Engineering*, vol. 27, no. 3, pp. 484–494, 2002.

[251] I. Lucifredi and H. Schmidt, "Subcritical scattering from buried elastic shells," *The Journal of the Acoustical Society of America*, vol. 120, no. 6, pp. 3566–3583, 2006.

[252] Y. Pailhas, C. Capus, K. Brown, and P. Moore, "Analysis and classification of broadband echoes using bio-inspired dolphin pulses," *The Journal of the Acoustical Society of America*, vol. 127, no. 6, pp. 3809–3820, 2010.

[253] D. A. Cook, J. T. Christoff, and J. E. Fernandez, "Broadbeam multi-aspect synthetic aperture sonar," in *MTS/IEEE OCEANS Conference*, vol. 1, 2001, pp. 188–192.

[254] J. Chatillon, A. E. Adams, M. A. Lawlor, and M. E. Zakharia, "SAMI: A low-frequency prototype for mapping and imaging of the seabed by means of synthetic aperture," *IEEE Journal of Oceanic Engineering*, vol. 24, no. 1, pp. 4–15, 1999.

[255] S. G. Schock, J. Wulf, G. Quentin, and J. Sara, "Synthetic aperture processing of buried object scanning sonar data," in *MTS/IEEE OCEANS Conference*, 2005, pp. 2236–2241.

[256] S.-M. Steele, R. Charron, J. Dillon, and D. Shea, "Performance prediction for a low frequency ultra-wideband synthetic aperture sonar," in *MTS/IEEE OCEANS Conference*, 2019, pp. 1–7.

[257] T. M. Marston, P. L. Marston, and K. L. Williams, "Scattering resonances, filtering with reversible SAS processing, and applications of quantitative ray theory," in *MTS/IEEE OCEANS Conference*, 2010, pp. 1–9.

[258] A. J. Hunter and R. van Vossen, "Sonar target enhancement by shrinkage of incoherent wavelet coefficients," *The Journal of the Acoustical Society of America*, vol. 135, no. 1, pp. 262–268, 2014.

[259] S. Synnes, A. Hunter, R. Hansen, T. Sæbø, H. Callow, R. Van Vossen, and A. Austeng, "Wideband synthetic aperture sonar backprojection with maximization of wave number domain support," *IEEE Journal of Oceanic Engineering*, vol. 42, no. 4, pp. 880–891, 2017.

[260] T. O. Sæbø, S. A. V. Synnes, and R. E. Hansen, "Wideband interferometry in synthetic aperture sonar," *IEEE Transactions on Geoscience and Remote Sensing*, vol. 51, no. 8, pp. 4450–4459, 2013.

[261] W. Zhu, L. Feng, C. Wang, Y. Wang, and W. Qiu, "Theory and signal processing of acoustic correlation techniques for velocity measurement of vessel," *IEEE Journal of Oceanic Engineering*, vol. 36, no. 2, pp. 338–346, 2011.

[262] T. E. Blanford, D. C. Brown, and R. J. Meyer, "Measurements and models of the correlation of redundant spatial coherence measurements for the incoherently scattered field," *The Journal of the Acoustical Society of America*, vol. 146, no. 6, pp. 4224–4236, 2019.

[263] D. C. Brown, I. D. Gerg, and T. E. Blanford, "Interpolation kernels for synthetic aperture sonar along-track motion estimation," *IEEE Journal of Oceanic Engineering*, vol. 45, no. 4, pp. 1497–1505, 2019.

[264] B. Thomas and A. Hunter, "Coherence-induced bias reduction in synthetic aperture sonar along-track micronavigation," *IEEE Journal of Oceanic Engineering*, 2021.

[265] A. J. Hunter, S. Dugelay, and W. Fox, "Repeat-pass synthetic aperture sonar micronavigation using redundant phase center arrays," *IEEE Journal of Oceanic Engineering*, vol. 41, no. 4, pp. 820–830, 2016.

[266] V. Myers, I. Quidu, B. Zerr, T. O. Sæbø, and R. E. Hansen, "Synthetic aperture sonar track registration with motion compensation for coherent change detection," *IEEE Journal of Oceanic Engineering*, vol. 45, no. 3, pp. 1045–1062, 2020.

[267] S. Synnes, R. Hansen, and T. Sæbø, "Spatial coherence of speckle for repeat-pass synthetic aperture sonar micronavigation," *IEEE Journal of Oceanic Engineering*, vol. 46, no. 4, pp. 1330–1345, 2021.

[268] B. Thomas, A. Hunter, and S. Dugelay, "Phase wrap error correction by random sample consensus with application to synthetic aperture sonar micronavigation," *IEEE Journal of Oceanic Engineering*, vol. 46, no. 1, pp. 221–235, 2021.

[269] A. Xenaki, B. Gips, and Y. Pailhas, "Unsupervised learning of platform motion in synthetic aperture sonar," *The Journal of the Acoustical Society of America*, vol. 151, no. 2, pp. 1104–1114, 2022.

[270] Y. Pailhas, Y. Petillot, K. Brown, and B. Mulgrew, "Spatially distributed MIMO sonar systems: Principles and capabilities," *IEEE Journal of Oceanic Engineering*, vol. 42, no. 3, pp. 738–751, 2016.

[271] T. M. Marston, S. G. Kargl, D. S. Plotnick, and K. L. Williams, "Improving downlooking SAS resolution with transmitter spatial diversity," in *MTS/IEEE OCEANS Conference*, 2019, pp. 1–5.

[272] A. Xenaki, Y. Pailhas, and R. Sabatini, "Sparse MIMO synthetic aperture sonar processing with distributed optimization," in *Asilomar Conference on Signals, Systems, and Computers*, 2020, pp. 82–87.

[273] T. Marston and J. Kennedy, "Spatially variant autofocus for circular synthetic aperture sonar," *The Journal of the Acoustical Society of America*, vol. 149, no. 6, pp. 4078–4093, 2021.

[274] S. Haykin, "Cognitive radar: A way of the future," *IEEE Signal Processing Magazine*, vol. 23, no. 1, pp. 30–40, 2006.

[275] A. C. Luchies and B. C. Byram, "Deep neural networks for ultrasound beamforming," *IEEE Transactions on Medical Imaging*, vol. 37, no. 9, pp. 2010–2021, 2018.

[276] N. Peretz and A. Feuer, "Deep learning applied to beamforming in synthetic aperture ultrasound," *arXiv preprint arXiv:2011.10321*, 2020.

[277] B. Yonel, E. Mason, and B. Yazıcı, "Deep learning for passive synthetic aperture radar," *IEEE Journal of Selected Topics in Signal Processing*, vol. 12, no. 1, pp. 90–103, 2018.

[278] B. Yonel, E. Mason, and B. Yazici, "Deep learning for waveform estimation and imaging in passive radar," *IET Radar, Sonar & Navigation*, vol. 13, pp. 915–926, 2019.

[279] M. Xu, N. Du, Z. Li, H. Yang, J. Wu, and J. Yang, "Cognitive SAR waveform design method based on joint optimization criteria," in *Asia-Pacific Conference on Synthetic Aperture Radar*, 2019, pp. 1–4.

[280] M. Gasse, F. Millioz, E. Roux, D. Garcia, H. Liebgott, and D. Friboulet, "High-quality plane wave compounding using convolutional neural networks," *IEEE Transactions on Ultrasonics, Ferroelectrics, and Frequency Control*, vol. 64, no. 10, pp. 1637–1639, 2017.

[281] M. U. Ghani, F. Can Meral, F. Vignon, and J.-l. Robert, "High frame-rate ultrasound imaging using deep learning beamforming," in *IEEE International Ultrasonics Symposium*, 2019, pp. 295–298.

[282] O. DeGuchy, J. Alvarez, A. Kim, R. F. Marcia, and C. Tsogka, "Machine learning for forward and inverse scattering in synthetic aperture radar," in *SPIE Applications of Machine Learning*, M. E. Zelinski, T. M. Taha, J. Howe, A. A. S. Awwal, and K. M. Iftekharuddin, Eds., vol. 11511, 2020, pp. 148–161.

[283] A. Krizhevsky, "Learning multiple layers of features from tiny images," University of Toronto, Tech. Rep., 2009. [Online]. Available: https://www.cs.toronto.edu/~kriz/cifar.html

[284] D. M. L. Vine, "Synthetic aperture radiometer systems," *IEEE Transactions on Microwave Theory and Techniques*, vol. 47, no. 12, pp. 2228–2236, 1999.

[285] A. R. Thompson, J. M. Moran, , and G. W. Swenson, *Interferometry and synthesis in radio astronomy*. John Wiley & Sons, 1986.

[286] D. M. Le Vine, "The sensitivity of synthetic aperture radiometers for remote sensing applications from space," *Radio Science*, vol. 25, no. 4, pp. 441–453, 1990.

[287] D. Le Vine, A. J. Griffis, C. T. Swift, and T. J. Jackson, "ESTAR: A synthetic aperture microwave radiometer for remote sensing applications," *Proceedings of the IEEE*, vol. 82, no. 12, pp. 1787–1801, 1994.

[288] C. S. Ruf, C. T. Swift, A. B. Tanner, and D. M. L. Vine, "Interferometric synthetic aperture microwave radiometry for remote sensing of the Earth," *IEEE Transactions on Geoscience and Remote Sensing*, vol. 26, no. 5, pp. 597–611, 1988.

[289] C. T. Swift, D. M. L. Vine, and C. S. Ruf, "Aperture synthesis concept in microwave remote sensing of the Earth," *IEEE Transactions on Microwave Theory and Techniques*, vol. 39, no. 12, pp. 1931–1935, 1991.

[290] J. R. Piepmeier, F. A. Pellerano, P. O'Neill, D. LeVine, E. Kim, and T. Doiron, "Synthetic thinned aperture radiometry (STAR) technologies enabling 10-km soil moisture remote sensing from space," in *NASA Earth Science Technology Conference*, 2002, p. B2P7.